Search for the Standard Model Higgs Boson in $ZH \to \mu^+\mu^- \, b\bar{b}$ Production at DØ and Evidence for the $H \to b\bar{b}$ Decay at the Tevatron

by

Jiaming Yu

A dissertation submitted in partial fulfillment
of the requirements for the degree of
Doctor of Philosophy
(Physics)
in the University of Michigan
2014

Doctoral Committee:

Assistant Professor Junjie Zhu, Chair
Professor Ratindranath Akhoury
Professor Jianming Qian
Assistant Professor Zhengya Zhang

ACKNOWLEDGEMENTS

Throughout the years there have been numerous people who have helped bring this thesis to fruition. I am indebted to all the kindly help I received!

I would like to express my heartfelt gratitude to my advisor, Dr. Junjie Zhu. It is his support, patience and generosity that guided me to this thesis. He has also shown me an excellent example of righteousness and professionalism that would take my lifetime to learn and practice.

My sincere thanks goes to all the members in the $ZH\ell\ell bb$ working group at DØ experiment when I was working on this analysis: Xuebing Bu, Seth Caughron, Marie-Claude Cousinou, Satish Desai, Suneel Dutt, Peng Jiang, Ashish Kumar, Qizhong Li, Elemer Nagy, Leah Welty-Rieger, Taka Yasuda for their support, guidance and helpful suggestions. Very special thanks go to Xuebing, Satish and Yunhe, who generously provided so much technical assistance and consolation when I was still struggling as a fresh beginner in this field.

I would also like to thank my other dissertation committee members: Prof. Ratindranath Akhoury, Prof. Jianming Qian and Dr. Zhengya Zhang for their time to evaluate my research work.

Happy thanks goes to all the friends I have met at the Fermilab and my officemates at the University of Michigan, Pengfei Ding, Weigang Geng, Dikai Li, Liang Li, Si Liu, Siqi Yang, Hang Yin, Haolv Feng, Xuefei Li, Lulu Liu and Nan Lu, thank you all for making my five years of Ph.D life so colorful and enjoyable.

Last but not least, I would to thank my family. It is the unconditional supports

from my parents that helped me through the trough of my research, their prayer for me was what sustained me thus far. A huge "thank you" to my husband, Chunpeng Wang, whose support, encouragement and patience were undeniably the bedrock upon which the past five years of my life have been built. His tolerance of my occasional moods is a testament to itself of his genuine love. I love you.

TABLE OF CONTENTS

LIST OF FIGURES

Figure

LIST OF TABLES

Table

LIST OF APPENDICES

Appendix

ABSTRACT

Search for the Standard Model Higgs Boson in $ZH \to \mu^+\mu^- b\bar{b}$ Production at DØ and Evidence for the $H \to b\bar{b}$ Decay at the Tevatron

by

Jiaming Yu

Chair: Junjie Zhu

A search for $ZH \to \mu^+\mu^- b\bar{b}$ is presented, using a Run 2 dataset with an integrated luminosity of 9.7 fb^{-1} collected by the DØ detector. Selected events contain at least two reconstructed jets and a Z candidate reconstructed with two opposite-sign charged muons. Random forests of decision trees are trained to distinguish between signal and background events in two orthogonal b-tag samples. The $ZH \to \mu^+\mu^- b\bar{b}$ analysis is then combined with $ZH \to e^+e^- b\bar{b}$ analysis. For the combined results of $ZH \to \ell^+\ell^- b\bar{b}$, no Higgs signal is observed, limits are set on the ZH cross-section $\times$ BR($H \to b\bar{b}$) for different Higgs masses, from 90 to 150 GeV. For a Standard Model (SM) Higgs boson of mass 125 GeV, the observed cross-section limit is 7.1 times the SM cross-section with an expected sensitivity of 5.1 times the SM cross section. The result of $ZH \to \ell^+\ell^- b\bar{b}$ channel has been combined with searches in other Higgs decay channels at the Tevatron, which led to the first evidence of $H \to b\bar{b}$.

CHAPTER I

Introduction

The end of the last millennium witnessed the triumph of the Standard Model (SM) of particle physics. The high-precision measurements carried out at the LEP, SLAC, Tevatron colliders and elsewhere have provided a decisive test of the SM theory and firmly established that it provides the correct effective description of the strong and electroweak interactions at present energies. In the SM, the Higgs mechanism has been postulated to instigate electroweak symmetry breaking (EWSB), from which the W/Z bosons, leptons and quarks gain masses. The mechanism gives rise to a new scalar particle – the Higgs boson. Finding the Higgs boson has been a scientific goal of many experiments in the past few decades. The Higgs boson had been the last piece of the puzzle that remained for a long time until it was discovered in 2012 at CERN.

This thesis presents a search for the SM Higgs boson in the process $ZH \to \mu^+\mu^- b\bar{b}$ in 9.7 fb^{-1} of $p\bar{p}$ collisions at $\sqrt{s} = 1.96$ TeV using the DØ detector. Chapter II gives a brief description about the theory of the SM and the Higgs boson. The DØ detector and the Tevatron accelerator are described in Chapter III. Chapter IV describes the reconstruction algorithms which transform the raw data recorded by the detector into physics objects that later are used to characterize the collisions. Chapters V to VII give details about the search for the Higgs boson in $ZH \to \mu^+\mu^- b\bar{b}$ channel. Results

of the search are presented in Chapter VIII The results of this analysis is published in [1] and [2], and it is combined with searches in other Higgs decay channels at the Tevatron, which lead to the first evidence of $H \to b\bar{b}$ [3].

CHAPTER II

The Standard Model and the Higgs Boson

2.1 The Standard Model

The SM is the theory of the electromagnetic, weak and strong interactions of elementary particles. The electroweak theory, proposed by Glashow, Salam and Weinberg to describe the electromagetic and weak interactions between quarks and leptons, is based on the gauge symmetry group $SU(2)_L \times U(1)_Y$ of weak left-handed isospin and hypercharge. Combined with Quantum Chromo-Dynamics (QCD), the theory of the strong interaction between the colored quarks based on the symmetry group $SU(3)_C$, the SM provides a unified framework to describe these three interactions. The theory is perturbative at sufficiently high energies and renormalizable, and thus describes these interactions at the quantum level.

There are two kinds of fields in the SM – matter field and gauge field.

(1) The matter fields include three generations of left-handed and right-handed chiral quarks and leptons, as shown in Tab. 2.1. The left-handed fermions are in weak isodoublets (L_i, Q_i), while the right-handed fermions are in weak isosinglets (e_{R_i}, u_{R_i} and d_{R_i}), where i goes from 1 to 3 for three different generations. There are not right-handed neutrinos in the SM because the present experimental evidence show that there are only left-handed neutrinos in the natrue.

The fermion hypercharge, Y_f, defined in terms of the third component of the weak

isospin I_f^3 and the electrical charge Q in units of the proton charge $+e$, is given by

$$Y_f = 2Q_f - 2I_f^3 \tag{2.1}$$

Moreover, the quarks are triplets under the $SU(3)_C$ group, while leptons are color singlets. This leads to the relation

$$\sum_f Y_f = \sum_f Q_f = 0 \tag{2.2}$$

which ensures the cancellation of chiral anomalies [4] within each generation, and thus preserving the renormalizability of the electroweak theory [5]. Each particle has an antiparticle, which has the same mass and spin, but has opposite values of electric charge, color charge, and flavor from the ordinary particles. Fields of anti-leptons and anti-quarks are labeled as $\bar{L}_i$, $\bar{Q}_i$, and $\bar{e}_{R_i}$, $\bar{u}_{R_i}$, $\bar{d}_{R_i}$, respectively.

Table 2.1: The fermion fields of the Standard Model and their quantum numbers; electrical charge Q, weak isospin I, the third component of the weak isospin I^3, and hypercharge Y . The color quantum number of the strong force is not included.

	Generation			Quantum number			
	1^{st}	2^{nd}	3^{rd}	Q_f	I_f	I_f^3	Y_f
Leptons	$L_1 \equiv \begin{pmatrix} \nu_e \\ e \end{pmatrix}_L$	$L_2 \equiv \begin{pmatrix} \nu_\mu \\ \mu \end{pmatrix}_L$	$L_3 \equiv \begin{pmatrix} \nu_\tau \\ \tau \end{pmatrix}_L$	0	1/2	+1/2	-1
				-1	1/2	-1/2	-1
	$e_{R_1} \equiv e_R$	$e_{R_2} \equiv \mu_R$	$e_{R_3} \equiv \tau_R$	-1	0	0	-2
Quarks	$Q_1 \equiv \begin{pmatrix} u \\ d \end{pmatrix}_L$	$Q_2 \equiv \begin{pmatrix} c \\ s \end{pmatrix}_L$	$Q_3 \equiv \begin{pmatrix} t \\ b \end{pmatrix}_L$	+2/3	1/2	+1/2	+1/3
				-1/3	1/2	-1/2	+1/3
	$u_{R_1} \equiv u_R$	$u_{R_2} \equiv c_R$	$u_{R_3} \equiv t_R$	+2/3	0	0	+4/3
	$d_{R_1} \equiv d_R$	$d_{R_2} \equiv s_R$	$d_{R_3} \equiv b_R$	-1/3	0	0	-2/3

(2) The gauge fields are corresponding to the spin-one bosons that mediate the interactions. In the electroweak sector, we have the field B_μ which corresponds to the generator Y (a constant, but could be different for different fermions) of the $U(1)_Y$ group, and the three fields $W_\mu^{1,2,3}$ which correspond to the generators $\frac{\tau^a}{2}$ ($a = 1, 2, 3,$

τ^a are the non-commuting 2×2 Pauli matrices) of the $SU(2)_L$ group. In the strong interaction sector, there is an octet of gluon fields $G_\mu^{1,\cdots,8}$ which correspond to the eight generators $\frac{\lambda^a}{2}$ ($a = 1, \cdots, 8$, λ^a are the 3×3 anti-commuting Gell-Mann matrices) of the $SU(3)_C$ group. The commutation relations between these generators are given by

$$\begin{aligned} &[Y, Y] = 0 \\ &\left[\tau^a, \tau^b\right] = 2i\epsilon^{abc}\tau_c \\ &\left[\lambda^a, \lambda^b\right] = 2if^{abc}\lambda_c, \text{ and } Tr[\lambda^a\lambda^b] = 2\delta_{ab} \end{aligned} \tag{2.3}$$

where ϵ^{abc} and f^{abc} are the antisymmetric tensors. Defining g_1, g_2 and g_s as the coupling constants of $U(1)_Y$, $SU(2)_L$ and $SU(3)_C$ respectively, the field strengths are given by

$$\begin{aligned} B_{\mu\nu} &= \partial_\mu B_\nu - \partial_\nu B_\mu \\ W^a_{\mu\nu} &= \partial_\mu W^a_\nu - \partial_\nu W^a_\mu - g_2\epsilon^{abc}W^b_\mu W^c_\nu \\ G^a_{\mu\nu} &= \partial_\mu G^a_\nu - \partial_\nu G^a_\mu - g_s f^{abc}G^b_\mu G^c_\nu \end{aligned} \tag{2.4}$$

The SM Lagrangian, without mass terms for fermions and gauge bosons, is then given by

$$\begin{aligned} \mathcal{L}_{SM} &= -\frac{1}{4}G^a_{\mu\nu}G^{\mu\nu}_a - \frac{1}{4}W^a_{\mu\nu}W^{\mu\nu}_a - \frac{1}{4}B_{\mu\nu}B^{\mu\nu} \\ &\quad + \bar{L}_i iD_\mu\gamma^\mu L_i + \bar{e}_{R_i} iD_\mu\gamma^\mu e_{R_i} + \bar{Q}_i iD_\mu\gamma^\mu Q_i + \bar{u}_{R_i} iD_\mu\gamma^\mu u_{R_i} + \bar{d}_{R_i} iD_\mu\gamma^\mu d_{R_i} \end{aligned} \tag{2.5}$$

where the covariant derivative D_μ is defined as

$$D_\mu = \partial_\mu - ig_1\frac{Y}{2}B_\mu - ig_2\frac{\tau_a}{2}W^a_\mu - ig_s\frac{\lambda_a}{2}G^a_\mu \tag{2.6}$$

and γ^μ ($\mu = 0, 1, 2, 3$) is the 4×4 Dirac matrices. In order to write Eqn. 2.6 in such

a compact form, a convention has to be introduced: whenever the terms in D_μ act on a fermion state of different matrix form, the result is zero by definition. For example, $\tau_a W_\mu^a$ is a 2×2 matrix in $SU(2)_L$ space and it gives zero if acting on e_R, u_R, d_R. Similarly, $\lambda_a G_\mu^a$ is a 3×3 matrix in color space, it gives zero if acting on the leptons (L, e_R) but is meaningful acting on the quarks.

The Lagrangian $\mathcal{L}_{SM}$ is invariant under the local $SU(3)_C \times SU(2)_L \times U(1)_Y$ gauge transformations for fermion and gauge fields. In the case of the electroweak sector, for instance, under a local transformation as shown in Eqn. 2.7, $\mathcal{L}_{SM}$ is unchanged.

$$\begin{aligned}
&L(x) \to L'(x) = e^{i\alpha_a(x)\tau^a + i\beta(x)Y} L(x),\ R(x) \to R'(x) = e^{i\beta(x)Y} R(x) \\
&\overrightarrow{W}_\mu(x) \to \overrightarrow{W'}_\mu(x) = \overrightarrow{W}_\mu(x) - \frac{1}{g_2}\partial_\mu \overrightarrow{\alpha}(x) - \overrightarrow{\alpha}(x) \times \overrightarrow{W}_\mu(x), \\
&B_\mu(x) \to B'_\mu(x) = B_\mu(x) - \frac{1}{g_1}\partial_\mu \beta(x)
\end{aligned} \tag{2.7}$$

The coupling between the fermion and gauge fields is also well defined by $\mathcal{L}_{SM}$. Some new notations have to be introduced to give a clear physics picture here, they are defined as follows:

$$\begin{cases} W^+ = (-W^1 + iW^2)/\sqrt{2} \\ W^- = (-W^1 - iW^2)/\sqrt{2} \\ W^0 = W^3 \end{cases} \tag{2.8}$$

$$\begin{cases} A_\mu = (g_2 B_\mu - g_1 Y_L W_\mu^0)/\sqrt{g_2^2 + g_1^2 Y_L^2} \\ Z_\mu = (g_1 Y_L B_\mu + g_2 W_\mu^0)/\sqrt{g_2^2 + g_1^2 Y_L^2} \end{cases} \tag{2.9}$$

$$\begin{cases} \sin\theta_w = -(g_1 Y_L)/\sqrt{g_2^2 + g_1^2 Y_L^2} \\ \cos\theta_w = (g_2)/\sqrt{g_2^2 + g_1^2 Y_L^2} \end{cases} \tag{2.10}$$

$W^\pm$ are mixtures of W^1, W^2 fields. γ/Z are mixtures of B and W^0 fields, thus can describe electromagnetic and weak interactions in a coherent framework. θ_W is the

mixing angle between pure EM and weak interactions.

It is noticed that in $\mathcal{L}_{SM}$ only the combination $g_1 Y_L$ (Y_L is the hypercharge of left-handed fermions) occurs, and we can choose (for convenience) $Y_L = -1$, since a redefinition of g_1 can always absorb and change in Y_L. The interaction terms in Eqn. 2.6, taking the first generation case as an example, could be re-written as:

$$\begin{aligned}\mathcal{L}_{SM} = &\sum_{f=\nu_e,e,u,d} eQ_f \bar{f}\gamma^\mu f A^\mu \\ &+\frac{g_2}{\cos\theta_w}\sum_{f=\nu_e,e,u,d}\left[\bar{f}_L\gamma^\mu f_L\left(I_f^3 - Q_f\sin^2\theta_w\right) + \bar{f}_R\gamma^\mu f_R\left(-Q_f\sin^2\theta_w\right)\right] Z_\mu \\ &+\frac{g_2}{\sqrt{2}}\left[\left(\bar{u}_L\gamma^\mu d_L + \bar{\nu}_{eL}\gamma^\mu e_L\right) W_\mu^+ + \left(\bar{d}_L\gamma^\mu u_L + \bar{e}_L\gamma^\mu \nu_{eL}\right) W_\mu^-\right] \\ &+\frac{g_s}{2}\sum_{q=u,d}\bar{q}_\alpha\gamma^\mu\lambda^a_{\alpha\beta}q_\beta G^a_\mu \end{aligned} \quad (2.11)$$

which are nothing but the vertices for processes of $\gamma \to (e^+e^-,\ q\bar{q})$, $Z \to (e^+e^-,\ q\bar{q},\ \nu_e\bar{\nu}_e)$, $W^- \to (e^-\bar{\nu}_e,\ \bar{u}d)$, $W^+ \to (e^+\nu_e,\ u\bar{d})$ and $g \to q\bar{q}$. For the second and third families one could just change the substitutions to (ν_μ, μ, c, s) or (ν_τ, τ, t, b).

Up to now, the gauge fields and the fermions fields have been kept massless, as there are not terms of format $-m_f\bar{\psi}_f\psi_f$ for fermions and $-\frac{1}{2}m^2\phi_\mu\phi^\mu$ for bosons. In the case of strong interactions, the gluons are indeed massless particles. In the case of electroweak sector, the situation is more problematic:

- the Z and W bosons have been proved experimentally to be massive. If we just explicitly adding terms of $\frac{1}{2}M_V^2 V_\mu V^\mu, (V = Z, W)$, the local $SU(2)_L \times U(1)_Y$ gauge symmetry will be broken;

- the fermion mass term

$$-m\bar{\psi}\psi = -m(\bar{\psi}_R\psi_L + \bar{\psi}_L\psi_R) \quad (2.12)$$

  is manifestly non-invariant under the isospin symmetry transformations, since

ψ_L is a member of an $SU(2)_L$ doublet while ψ_R is a member of a singlet.

The question is therefore brought up – is there a way to generate the gauge boson and the fermion masses without violating $SU(2)_L \times U(1)_Y$ gauge invariance? The answer is yes: the Higgs-Brout-Englert-Guralnik-Hagen-Kibble mechanism of spontaneous symmetry breaking [6], or the Higgs mechanism for short.

2.2 Higgs mechanism

For the Higgs mechanism, in essence the assumption is made that the universe is filled with a spin-zero field, called a Higgs field, that is a doublet in the $SU(2)_L$ space and carries non-zero $U(1)_Y$ hypercharge, but is a singlet in color space. The gauge bosons and fermions can interact with this field, and in its presence they no longer appear to be massless.

By introducing the Higgs fields, we need to generate masses for the three gauge bosons $W^{\pm}$ and Z, and the photon should remain massless so that quantum electrodynamics (QED) must stay an exact symmetry. Therefore, we need at least 3 degrees of freedom for the scalar fields. The simplest choice is a complex $SU(2)_L$ doublet of scalar fields ϕ

$$\phi = \begin{pmatrix} \phi^+ \\ \phi^0 \end{pmatrix}, \; Y_\phi = +1 \tag{2.13}$$

where ϕ^+ and ϕ^0 are complex fields,

$$\phi^+ = \frac{\phi_1 + i\phi_2}{\sqrt{2}} \tag{2.14}$$

$$\phi^0 = \frac{\phi_3 + i\phi_4}{\sqrt{2}} \tag{2.15}$$

with the following constraint to make sure the potential term in the Lagrangian (Eqn.

2.17) is invariant under the local gauge transformation

$$\phi^\dagger\phi = \frac{\phi_1^2 + \phi_2^2 + \phi_3^2 + \phi_4^2}{2} = \text{invariant} \tag{2.16}$$

The Lagrangian associated with this Higgs (scalar) field is written as

$$\mathcal{L}_S = (D^\mu\phi)^\dagger(D_\mu\phi) - V(\phi) = |D^\mu\phi|^2 - (\mu^2\phi^\dagger\phi + \lambda(\phi^\dagger\phi)^2) \tag{2.17}$$

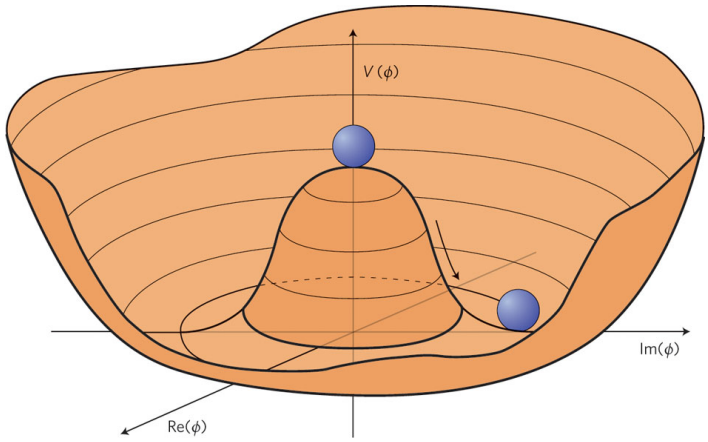

Figure 2.1: An effective potential, $V(\phi)$

In the potential $V(\phi)$, $\mu^2\phi^\dagger\phi$ is the mass term and $\lambda(\phi^\dagger\phi)^2$ is the self-coupling term. The self-coupling λ is required to be positive to make the potential bounded from below. If μ^2 is positive, the vacuum, which minimizes the potential, corresponds to $\phi = 0$. If $\mu^2 < 0$, then $V(\phi)$ has a minimum at

$$\phi^\dagger\phi = \frac{-\mu^2}{2\lambda} \equiv \frac{\upsilon^2}{2} \tag{2.18}$$

where $\upsilon = \sqrt{-\mu^2/\lambda}$ is defined as the vacuum expectation value (VEV). There are many ways to have Eqn. 2.18 satisfied, as shown in Fig. 2.1. We pick, arbitrarily,

the point $\phi_3 = \upsilon,\ \phi_1 = \phi_2 = \phi_3 = 0$, and expand around the vacuum, so that

$$\phi = \frac{1}{\sqrt{2}} \begin{pmatrix} 0 \\ \upsilon + H \end{pmatrix} \tag{2.19}$$

Here, the "H" is the so-called Higgs boson. The choice that only the neutral component ϕ^0 gets a vacuum expectation value is very important, since whatever quantum numbers ϕ carries can vanish into the vacuum. If ϕ^+ had a vacuum expectation value then electric charge would not be conserved, contrary to observation.

Now the term $(D^\mu\phi)^\dagger(D_\mu\phi)$ in Eqn. 2.17 could be fully expanded as

$$\begin{aligned} |D_\mu\phi|^2 &= |(\partial_\mu - ig_1 Y_\phi \tfrac{1}{2} B_\mu - ig_2 \tfrac{\tau_a}{2} W_\mu^a)\phi|^2 \\ &= \tfrac{1}{2}(\partial_\mu H)^2 + \tfrac{1}{8} g_2^2 (\upsilon + H)^2 |W_\mu^1 + iW_\mu^2|^2 + \tfrac{1}{8}(\upsilon + H)^2 |g_2 W_\mu^0 - g_1 B_\mu|^2 \end{aligned} \tag{2.20}$$

Considering the notations defined in Eqn. 2.9 and 2.10, we have

$$\begin{aligned} |D_\mu\phi|^2 &= \tfrac{1}{2}(\partial_\mu H)^2 + \tfrac{1}{4} g_2^2 \upsilon^2 W_\mu^+ W^{-\mu} + \tfrac{1}{8}(g_1^2 + g_2^2)\upsilon^2 Z_\mu Z^\mu \\ &+ \tfrac{1}{2} g_2^2 \upsilon H W_\mu^+ W^{-\mu} + \tfrac{1}{4}(g_1^2 + g_2^2)\upsilon H Z_\mu Z^\mu + \tfrac{1}{4} g_2^2 H^2 W_\mu^+ W^{-\mu} + \tfrac{1}{8}(g_1^2 + g_2^2) H^2 Z_\mu Z^\mu \\ &= \tfrac{1}{2}(\partial_\mu H)^2 + M_W^2 W_\mu^+ W^{-\mu} + \tfrac{1}{2} M_Z^2 Z_\mu Z^\mu + \tfrac{2M_W^2}{\upsilon} H W^+ W^- + \tfrac{M_W^2}{\upsilon^2} H^2 W^+ W^- \\ &+ \tfrac{M_Z^2}{\upsilon} H Z Z + \tfrac{M_Z^2}{2\upsilon^2} H^2 Z Z \end{aligned} \tag{2.21}$$

In the last step of Eqn. 2.21, we already use the format of masses of gauge bosons:

$$M_W = \frac{1}{2}\upsilon g_2,\ M_Z = \frac{1}{2}\upsilon\sqrt{g_2^2 + g_1^2},\ M_A = 0 \tag{2.22}$$

We have achieved half of our goal so far, by spontaneously breaking the symmetry $SU(2)_L \times U(1)_Y \to U(1)_Q$, three Goldstone bosons have been absorbed by the $W^\pm$ and Z bosons to form their longitudinal components and get their masses. Since the $U(1)_Q$ symmetry is still unbroken with the photon as its generator, the photon

remains massless as it should be.

The mass of fermions are also generated using the same scalar field ϕ, a so-called Yukawa Lagrangian ($SU(2)_L \times U(1)_Y$ invariant) is introduced

$$\begin{aligned} \mathcal{L}_F &= \textstyle\sum_{f=leptons,quarks} -\lambda_f(\bar{f}_L \phi f_R + \phi^\dagger \bar{f}_R f_L) \\ &= -\textstyle\sum_f \frac{\lambda_f \upsilon}{\sqrt{2}}(\bar{f}_L f_R + \bar{f}_R f_L) + \frac{\lambda_f}{\sqrt{2}}(\bar{f}_L f_R + \bar{f}_R f_L)H \\ &= -\textstyle\sum_f m_f \bar{f} f + \frac{m_f}{\upsilon}\bar{f} f H \end{aligned} \tag{2.23}$$

where

$$m_f = \frac{\lambda_f \upsilon}{\sqrt{2}} \tag{2.24}$$

With the same isodoublet ϕ of scalar fields, we have generated the masses of both the weak vector bosons $W^\pm$, Z and the fermions, while preserving the $SU(2)_L \times U(1)_Y$ gauge symmetry, which is now spontaneously broken or hidden. The electromagnetic $U(1)_Q$ symmetry, as well as the $SU(3)_C$ color symmetry, stay unbroken. In this simplest form of Higgs mechanism, a neutral particle, the Higgs boson, is required to exist. Equation. 2.17 also contains the terms associated with this Higgs boson – the kinetic part of the Higgs field, $\frac{1}{2}(\partial_\mu H)^2$, comes from the term involving the covariant derivative $|D_\mu \phi|^2$, while the mass and self interaction parts come from the potential $V(\phi)$:

$$\begin{aligned} \mathcal{L}_H &= \tfrac{1}{2}(\partial_\mu H)^2 - V \\ &= \tfrac{1}{2}(\partial_\mu H)^2 - \lambda \upsilon^2 H^2 - \lambda \upsilon H^3 - \tfrac{\lambda}{4} H^4 \\ &= \tfrac{1}{2}(\partial_\mu H)^2 - \tfrac{1}{2} M_H^2 H^2 - \tfrac{M_H^2}{2\upsilon} H^3 - \tfrac{M_H^2}{8\upsilon^2} H^4 \end{aligned} \tag{2.25}$$

where

$$M_H = \sqrt{2\lambda \upsilon^2} \tag{2.26}$$

2.2.1 Decays of the SM Higgs boson

In the SM, once the Higgs mass is fixed, the profile of the Higgs particle is uniquely determined. The couplings of the Higgs boson to gauge bosons (Eqn. 2.21) and fermions (Eqn. 2.23) are directly proportional to the masses of these particles, thus the Higgs boson will have the tendency to decay into the heaviest ones in the allowed phase space. In the experiment, people usually search for Higgs boson in the following three types of decay mode [7]:

- Decays into fermions (quarks and leptons).

  The tree level Feynman diagram is shown on the left plot of Fig. 2.2, and the partial width of the Higgs boson decay into fermion paris is given by [8] [9]

$$\Gamma(H \to f\bar{f}) = \frac{G_\mu N_c}{4\sqrt{2\pi}} M_H m_f^2 \beta_f^3 \tag{2.27}$$

  where $\beta = (1 - 4m_f^2/M_H^2)^{1/2}$, N_c is the color factor with $N_c = 3(1)$ for quarks (leptons) and G_μ is the Fermi constant.

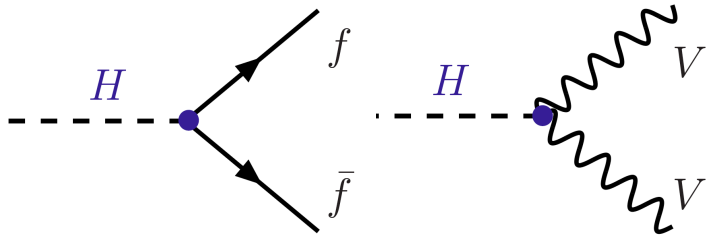

(a) (b)

Figure 2.2: The Feynman diagram for the Higgs boson decays into fermions (left) and real vector bosons (W or Z) (right).

- Decays into electroweak gauge bosons.

  Above the WW and ZZ kinematic thresholds, the Higgs boson will decay mainly into pairs of massive gauge bosons, the tree level diagram is shown

on the right plot of Fig. 2.2, here $V = W, Z$. The partial width for a Higgs boson decaying into two real massive gauge bosons is given by [10] [9]

$$\Gamma(H \to VV) = \frac{G_\mu M_H^3}{16\sqrt{2\pi}} \delta_V \sqrt{1-4x}(1-4x+12x^2) \tag{2.28}$$

where $\delta_W = 2$, $\delta_Z = 1$ and $x = M_V^2/M_H^2$. Below the WW/ZZ kinematic thresholds, the Higgs boson could also decay into two massive gauge bosons, but with one or two of them off-shell.

- Loop-induced decays into $\gamma\gamma$, γZ and gg.

  Since gluons and photons are massless, they do not couple to the Higgs boson directly. Nevertheless, the Hgg, $H\gamma\gamma$ and $H\gamma Z$ coupling can be generated at the quantum level with loops involving massive particles. The $H\gamma\gamma$ and $H\gamma Z$ couplings are mediated by W boson and charged fermion loops, while the Hgg coupling is mediated only by quark loops, as shown in Fig. 2.3.

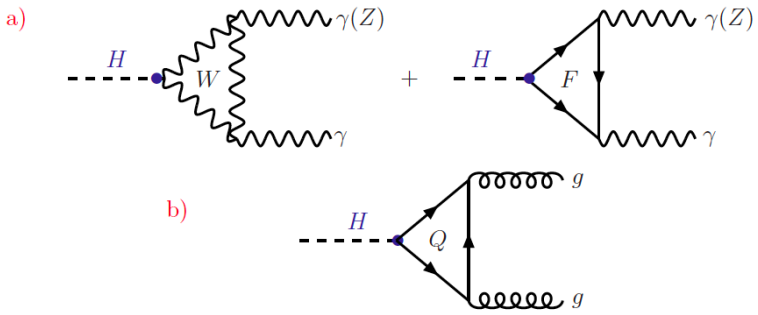

Figure 2.3: Loop-induced Higgs boson decays into a) $\gamma\gamma$ or γZ, b) gg.

The decay branching ratios and the total width of the SM Higgs boson as a function of the Higgs boson mass are shown in Fig. 2.4 and 2.5 [7]. In the low mass range (110 GeV $\lesssim M_H \lesssim$ 130 GeV), the main decay mode of the Higgs boson is $H \to b\bar{b}$ with a branching ratio of $75-50\%$. The $\gamma\gamma$ and γZ decays are rare, with branching ratios at the level of a few per mille. The $H \to WW^*$ decays, which are below the 1% level for

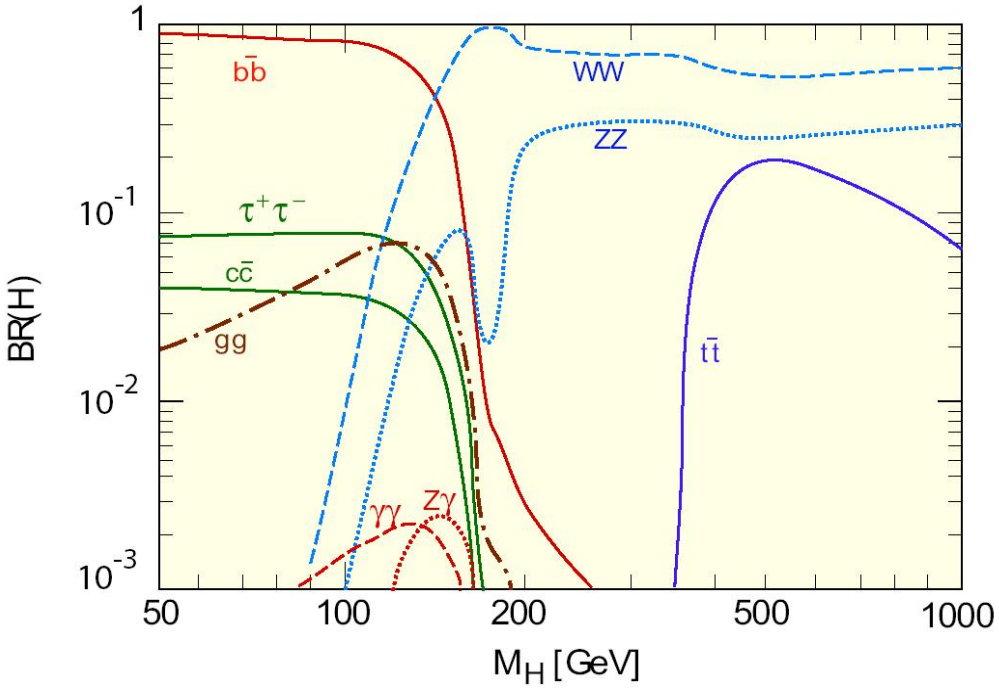

Figure 2.4: The SM Higgs boson decay branching ratios as a function of M_H.

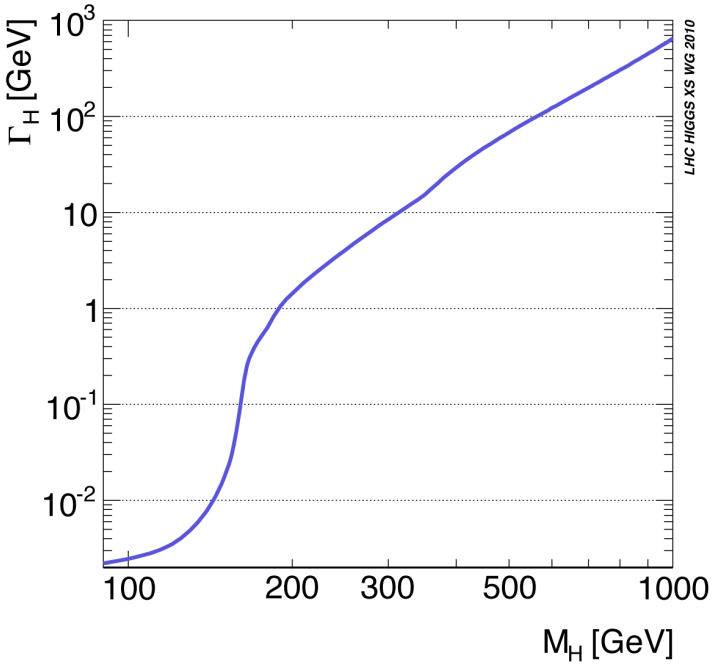

Figure 2.5: The SM Higgs boson total decay width as a function of M_H.

$M_H \sim 100$ GeV, dramatically increase with M_H to reach $\sim 30\%$ at $M_H \sim 130$ GeV; for this mass value, $H \to ZZ^*$ occurs at the percent level. In the intermediate mass range (130 GeV $\lesssim M_H \lesssim$ 180 GeV), the Higgs boson decays mainly to WW and ZZ pairs, with one off-shell gauge boson below the $2M_V$ kinematic threshold. The WW decay starts to dominate at $M_H \sim 130$ GeV and becomes gradually overwhelming, in particular for $2M_W \lesssim M_H \lesssim 2M_Z$, where the W boson is real while the Z boson is still virtual, strongly suppressing the $H \to ZZ^*$ mode and leading to a WW branching ratio of almost 100%. In the high mass range ($M_H \gtrsim 2M_Z$), the Higgs boson decays exclusively into the massive gauge boson channels with a branching ratio of $\sim 2/3$ for WW and $\sim 1/3$ for ZZ. The opening of the $t\bar{t}$ channel for $M_H \gtrsim 350$ GeV does not alter significantly this pattern. The reason is that while the $H \to t\bar{t}$ partial decay width grows as M_H, the partial decay width into (longitudinal) gauge bosons increases as M_H^3.

For the total decay width, the Higgs boson is very narrow in the low mass range, $\Gamma_H < 10$ MeV, but the width becomes rapidly wider for masses larger than 130 GeV, reaching ~ 1 GeV slightly above the ZZ threshold. For $M_H \gtrsim 500$ GeV, its decay width is comparable to its mass because of the longitudinal gauge boson contributions in the decays $H \to WW, ZZ$. For even larger mass (~ 1 TeV), the perturbation theory is jeopardized.

2.2.2 Higgs production at Tevatron

For the SM Higgs boson, the main production mechanisms at hadron colliders make use of the fact that the Higgs boson couples preferentially to the heavy particles: the massive W and Z vector bosons, the top quark and the bottom quark. The four main production processes and their Feynman diagrams are shown in Fig. 2.6.

- $gg \to H$: gluon-gluon fusion
- $gg, q\bar{q} \to q\bar{q} + H$

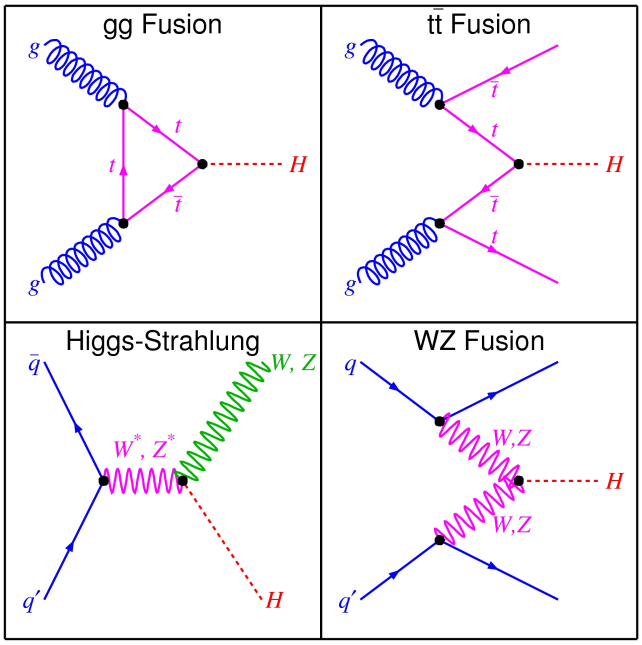

Figure 2.6: The dominant SM Higgs boson production mechanisms in hadronic collisions.

- $q\bar{q} \to V + H$: associated production with W/Z
- $q\bar{q} \to V^*V^* \to qq + H$: vector boson fusion

The cross sections for the Higgs boson production in the main channels are summarized in Fig. 2.7 at the Tevatron Run 2 with a center-of-mass energy $\sqrt{s} = 1.96$ TeV. The most relevant production mechanism is the associated production with W/Z bosons (the $WH : ZH$ cross section ratio is approximately 1.5 for $M_H \lesssim 200$ GeV), and the cross section is slightly less than 250 fb for $M_H \sim 120$ GeV. The WW/ZZ fusion cross sections are on the same order in the mass range $M_H \lesssim 100$ -200 GeV, while the cross sections for associated production with $t\bar{t}$ pairs are rather low, being less than 10 fb for $M_H \sim 115$ GeV. The gg fusion mechanism has the largest production cross section, but suffers from a vert large QCD background.

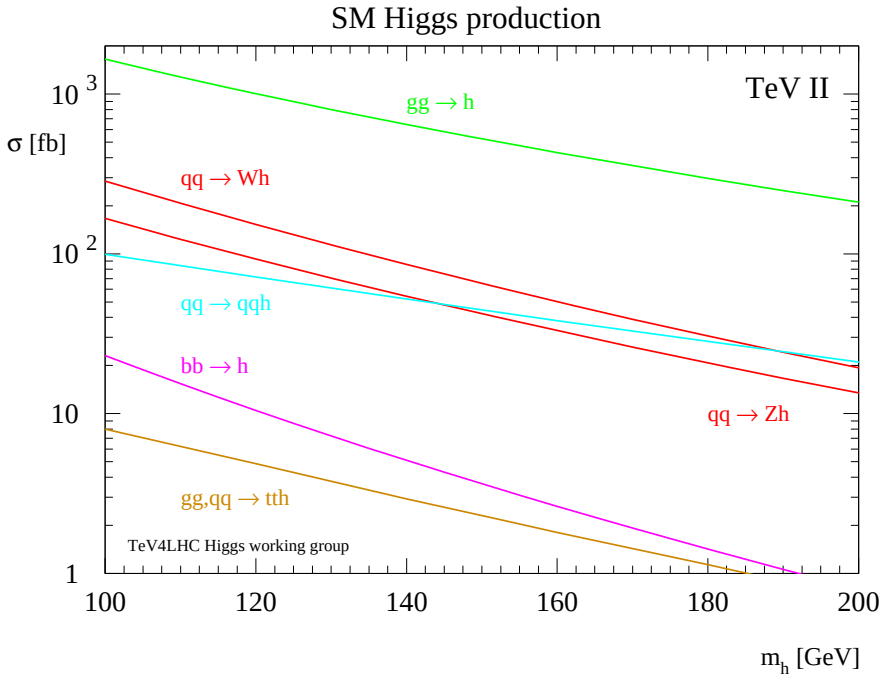

Figure 2.7: The SM Higgs boson production cross sections at the Tevatron in the dominant channels as a function of M_H [11].

2.3 Search for the SM Higgs boson

High energy physicist has been hunting for the Higgs boson for decades. The difficulty in finding the Higgs boson arises, in part, because its coupling are proportional to mass, so they are small for the light particles that are most copiously available. Another reason is that the mass of Higgs boson is unknown, and there are few theoretical constraints could be set on it. As shown in Eqn. 2.26, M_H depends on the coefficient λ of the Higgs self-interaction in the Higgs potential. Since there is no understanding of the physical origin of λ, its numerical value is not known. Nor does any other observables depend on λ in a way that allows λ to be extracted.

2.3.1 Experimental constraints on the Higgs boson mass

The Higgs boson will contribute to the radiative corrections to the high-precision electroweak observables, there are constraints on its mass, which is the only yet unknown free parameter in the SM. Precision electroweak data, including the latest W boson mass measurements from the CDF [12] and DØ [13] collaborations and the latest Tevatron combination for the top quark mass [14], constrain the mass of the SM Higgs boson to $M_H < 152$ GeV [15] at the 95% confidence level (C.L.). Direct searches at the CERN e^+e^- Collider (LEP) [16], by the CDF and DØ collaborations at the Fermilab Tevatron pp Collider [17], and by the ATLAS and CMS collaborations at the CERN Large Hadron Collider (LHC) [18][19] further restrict the allowed range to $122.1 < M_H < 127.0$ GeV. The experimental constraints on the Higgs boson mass are summarized in Fig. 2.8.

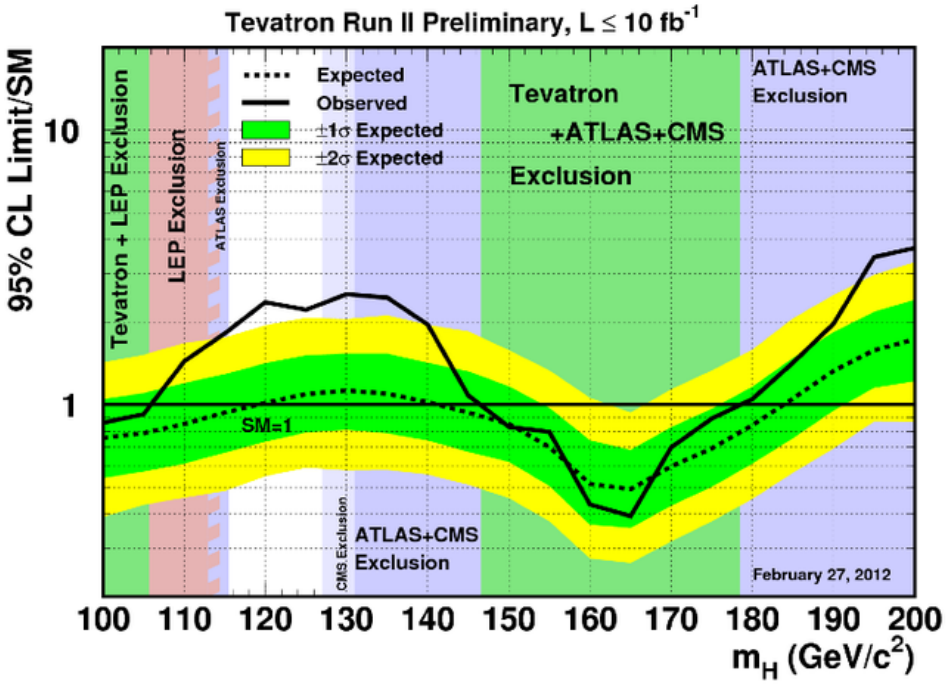

Figure 2.8: The experimental constraints on the SM Higgs mass.

2.3.2 The discovery of a "Higgs-like" boson

In summer 2013, the CDF and DØ collaborations combined the searches for the associated production of a Higgs boson with W or Z boson and subsequent decay of teh Higgs boson to $b\bar{b}$. The searches are conducted for a Higgs boson in the low mass range. An excess of events in the data compared with the background prediction is observed, which is most significant in the mass range between 120 and 135 GeV. The largest local significance is 3.3 standard deviation (s.d.), corresponding to a global significance of 3.1 standard deviations [3]. The details of Higgs boson search at the Tevatron will be discussed in Sect. IX.

On July 4th 2012, the ATLAS and CMS collaborations reported excesses above background expectations at 5σ level, consistent with the production of a SM Higgs boson at $M_H \approx 126$ GeV [20][21]. Much of the power of the LHC searches comes from $gg \to H$ production and the Higgs boson decays into $\gamma\gamma$ and ZZ, which probe the couplings of the Higgs boson to gauge bosons. Figures. 2.9 show the Higgs mass distribution which reconstructed from two photons or four leptons from ZZ decay (from ALTAS collaboration). This observation, which has a significance of 5.9 standard deviations (as shown in Fig. 2.10), corresponding to a background fluctuation probability of 1.7×10^{-9}, is compatible with the production and decay of the SM Higgs boson. Strong evidence shows that the discovered boson has spin J=0 and parity P+, which is consistent with the SM prediction. The couplings of this new boson to fermions and bosons, as well as anomalous contributions to loop-induced production and decay modes, are measured, All measurements are consistent with expectations for the SM Higgs boson.

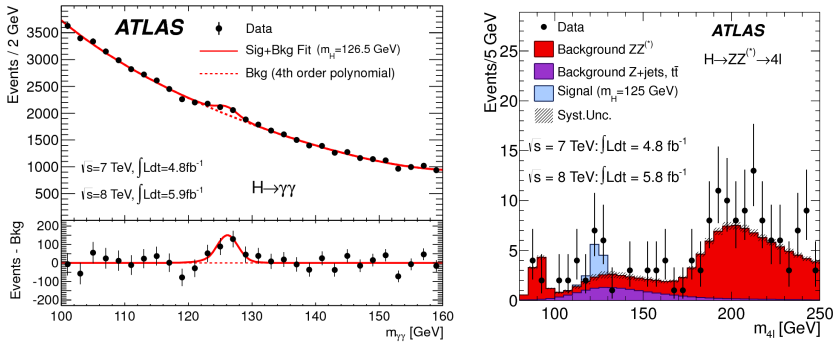

Figure 2.9: The distributions of the invariant mass of diphoton candidates (left) and the four-lepton invariant mass (right) for the combined 7 TeV and 8 TeV data sample.

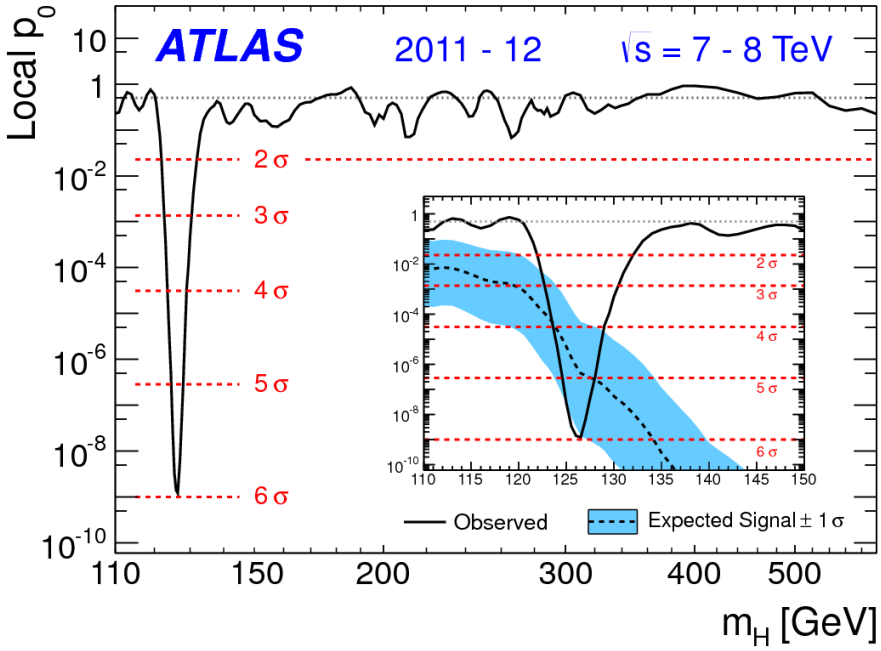

Figure 2.10: The local probability p_0 (uncapped) as a function of M_H. The dashed curve shows the median expected local p0 under the hypothesis of a SM Higgs boson production signal at that mass. The horizontal dashed lines indicate the p-values corresponding to significances of 1σ to 6σ.

2.4 Search for $ZH \to \ell^+\ell^- b\bar{b}$ process at the Tevatron

The detector signature of a $ZH \to \ell^+\ell^- b\bar{b}$ event at the Tevatron is two energetic b jets and two opposite-sign charged leptons whose combined mass is near that of the Z boson. The $ZH \to \ell^+\ell^- b\bar{b}$ Higgs search channel is distinguished from other Tevatron modes by the lack of neutrinos in the final states. The lack of neutrinos means that both the $H \to b\bar{b}$ and $Z \to \ell^+\ell^-$ decays can be reconstructed without the need to infer the presence of particles from missing energy. This feature provides a strong control on background processes that compensates for the low production cross section $\times$ $Z \to \ell^+\ell^-$ branching ratio.

Leading order Feynman diagrams for $ZH \to \ell^+\ell^- b\bar{b}$ and important background processes to this search are shown in Fig. 2.11. The primary standard model background is $Z + b\bar{b}$ production. This process shares the same final states as $ZH \to \ell^+\ell^- b\bar{b}$, except it lacks of a "Higgs" resonance in the distribution of the reconstructed dijet mass. The next largest background is $t\bar{t}$ production where each top decays to a W and a b quark, and both W bosons decay leptonically. The two neutrinos from the W decays appear as significant missing transverse energy, a feature which is not present in $ZH \to \ell^+\ell^- b\bar{b}$ events. The remaining backgrounds come from diboson(WW, WZ, ZZ) and multijet production with non-prompt leptons, or with jets misidentified as leptons.

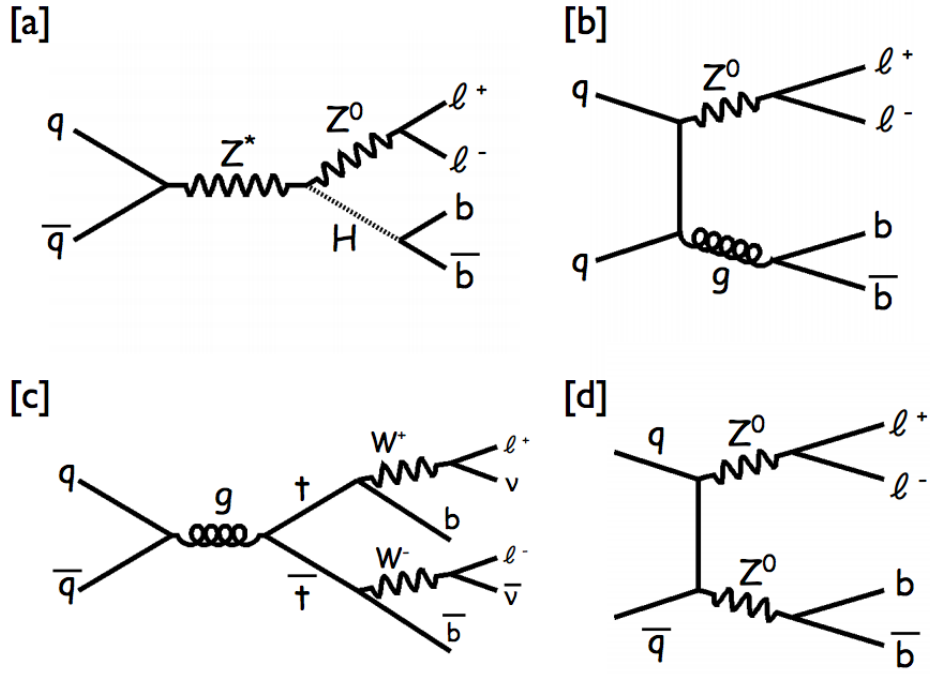

Figure 2.11: Leading order Feynman diagrams for $ZH \to \ell^+\ell^- b\bar{b}$ [a], $Z + b\bar{b}$ [b], $t\bar{t}$ [c], and Diboson ZZ production [d].

CHAPTER III

The Tevatron Accelerator and the DØ detector

3.1 The Fermilab accelerator system

The Tevatron accelerator was the world's highest energy proton-antiproton collider before it was shut down on September 30, 2011. Some of the most important fundamental discoveries of recent decades happened at the Tevatron, such as the discovery of the top quark [22], which helped to test and refine the SM of particle physics. The whole chain of the Fermilab's accelerator system is shown in Fig. 3.1, which includes the Pre-accelerator, Linac, Booster, Debuncher and Accumulator (two machines are referred to as the Antiproton Source, which is shown as the purple triangle in Fig. 3.1), Main Injector (MI) and the Tevatron. A summary of some parameters of the Fermilab accelerator system is listed in Tab. 3.1.

Producing negatively charged hydrogen ions is the first step in creating proton and antiproton beams. The Linac, approximately 500 feet long, accelerates the negatively charged hydrogen ions (H^-) to 400 MeV. Those ions are injected to the next accelerator – Booster, a circular accelerator located about 20 feet below ground. Just after entering the Booster, the ions pass through a carbon foil, which removes electrons from the ions, creating positively charged protons. The protons travel around the Booster about 20,000 times, and experience an accelerating force from an electric field in a radio-frequency cavity during each revolution. This boosts the protons

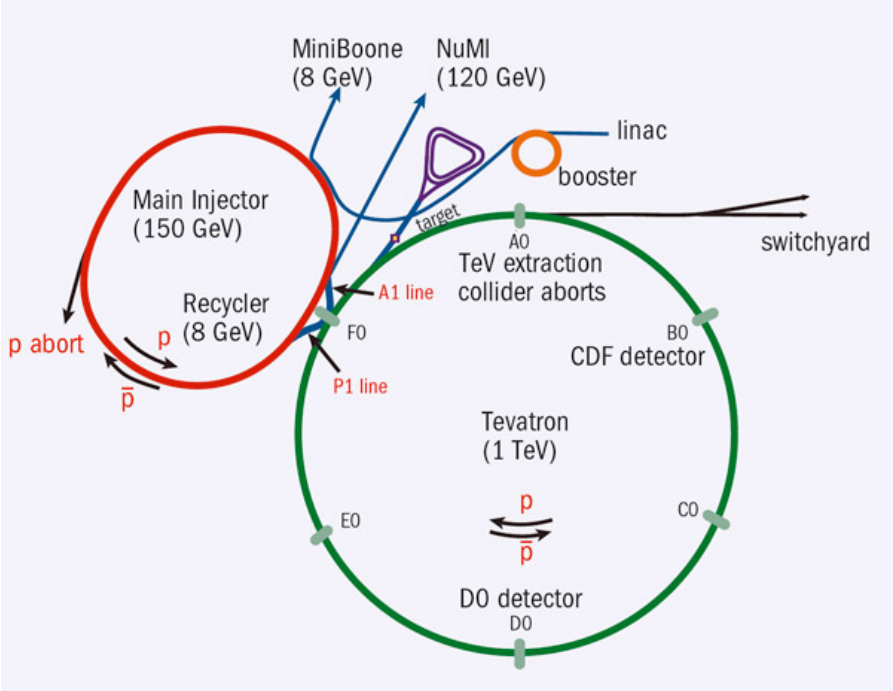

Figure 3.1: Overview of the Tevatron accelerator chain.

energy up to 8 GeV by the end of the acceleration cycle.

To produce antiprotons, proton beams are steered into a nickel target. The collisions produce a wide range of secondary particles, including many antiprotons. All secondary particles enter a beamline where antiprotons are captured and focused. Finally antiprotons are injected into a storage ring where they are accumulated and cooled.

After accumulating a sufficient number of antiprotons, the proton and antiproton beams are sent to the MI for additional cooling and accumulation before they are injected into the Tevatron. The MI is a circular synchrotron seven times the circumference of the Booster and slightly more than half of the Tevatron circumference. It can operate in different modes: (1) accelerate protons and antiprotons before injection into the Tevatron; (2) deliver protons for antiproton production; and (3) transfer antiprotons from the antiproton storage ring to the Tevatron. One of the main Run 2 upgrade is adding the Recycler to the Main Injector Project. The Recycler Ring

increases the collision rate in the Tevatron collider by a factor of three to five beyond that with the Main Injector alone. Without the Recycler, the precious antiprotons left at the end of a collider "store" must be thrown away. The Recycler allows these antiprotons to be re-used in a later store.

After the proton and antiproton beams are accelerated to 150 GeV in the MI, they are injected into the Tevatron. The Tevatron is a superconducting magnet synchrotron with a radius of 1 km that accelerates protons and antiprotons in opposite directions. The Tevatron is split into six sections labeled A to F, each section being further split into numbered subsections. Each Ø subsection is a straight section and some of them are special. FØ is the location of the Tevatron 8 RF cavities and the transfer lines to the MI. BØ is the home of the CDF detector, while DØ is the home of the detector with the same name.

During Run I data taking period (1992-1996), the Tevatron operated six bunches of protons and antiprotons, with 3500 ns between each bunch crossing and a center-of-mass energy of 1.8 TeV. The peak luminosity was typically $1 - 2 \times 10^{31}$ cm^{-2}s^{-1} and approximately 150 pb^{-1} of data were delivered . Following the completion of the new MI and associated Tevatron upgrades [23], Run II data taking period began in March 2001 and ended in September 2011. During Run II, the Tevatron was operated with 36 bunches of proton and antiprotons with a bunch spacing of 396 ns and at a center-of-mass energy of 1.96 TeV. The peak instantaneous luminosity recorded is 4×10^{32} cm^{-2}s^{-1}, and data with a total integrated luminosity of 11.9 fb^{-1} data were recorded by both detectors.

3.2 The DØ detector

The DØ experiment was proposed in 1983 to study proton-antiproton collisions at the Fermilab Tevatron collider. During Run I of the Tevatron, approximately 120 pb^{-1} of data were recorded by the DØ detector, which led to the discovery

Table 3.1: Fermilab accelerator parameters

Accelerator	Initial kinetic energy (GeV)	Final kinetic energy (GeV)	Length or Radius (m)	Destination of beam
Pre-acc	$\tilde{0}$	7.5×10^{-4}	15	Linac
Linac	7.5×10^{-4}	0.4	120	Booster
Booster	0.4	8	75	Main Injector
Main Injector	8	120	529	Antiproton source
		150	529	Tevatron
Tevatron	150	980	1000	Stays in Tevatron
				$\bar{p}$ to Recycler
Antiproton source	8	8	75	Main Injector
Recycler	8	8	529	Main Injector

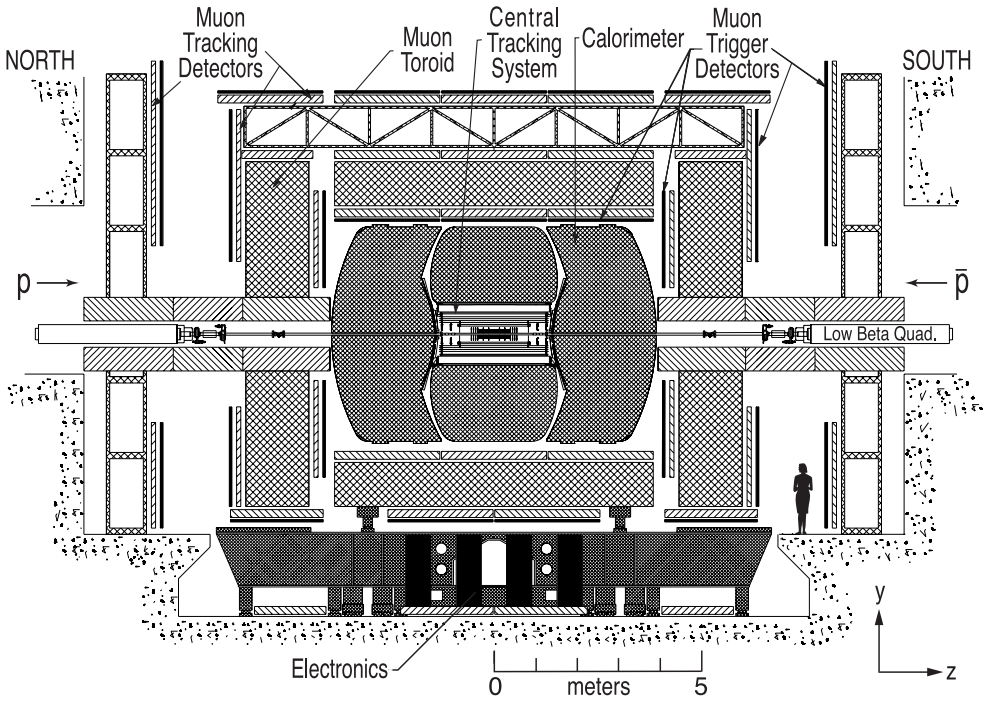

Figure 3.2: Diagram of the upgraded DØ detector, as viewed from inside the Tevatron ring.

of the top quark in 1995 [22]. To accommodate the Tevatron upgrades for Run II, the DØ detector was also significantly upgraded [26]. The upgraded detector consists of three major subsystems: central tracking detectors, uranium/liquid-argon calorimeters, and a muon spectrometer [24]. A side view of the DØ detector is shown in Fig. 3.2. The right-handed coordinate system is used – the z-axis is defined along

the proton direction, the y-axis is upward and the x-axis is pointing to the center of the Tevatron. Usually, the $x - y$ plane is called the transverse plane. The angles ϕ and θ are the azimuthal and polar angles, respectively. The r coordinate denotes the distance to the z axis in the transverse plan. The pseudorapidity, $\eta = -\ln[\tan(\theta/2)]$, approximates the true rapidity, $y = 1/2\ln[(E + p_z)(E - p_z)]$, for finite angles in the limit that $(mc^2/E) \to 0$. The term "forward" is used to describe the regions at large $|\eta|$. Usually, we use "$\eta_{\rm det}$" stands for the value calculated with the center of the detector as the origin of the coordinate, and use "η" stands for the value calculated with the reconstructed primary vertex as the origin of the coordinate. The transverse momentum, p_T, is the component of momentum in the transverse plane. Both $p_{\rm T}$ and y are Lorentz-invariant variables.

3.2.1 Central tracking

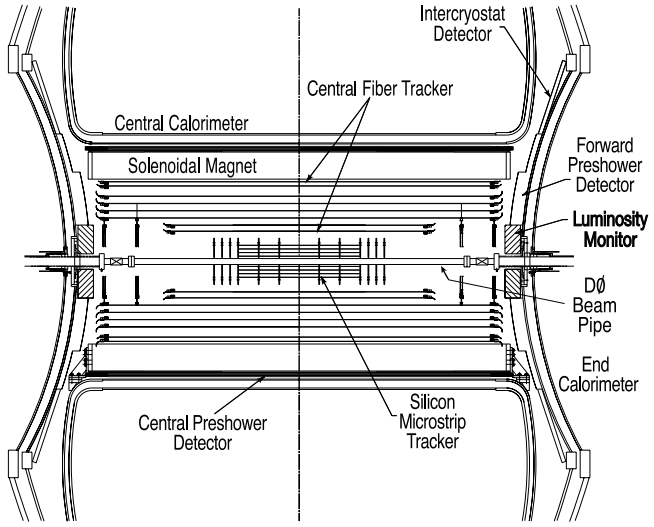

Figure 3.3: Cross-sectional view of the central tracking system in the x-z plane. Also shown are the locations of the solenoid, the preshower detectors, luminosity monitor, and the calorimeters.

A schematic view of the central tracking system is shown in Fig. 3.3. It surrounds the DØ beryllium beam pipe (the gray part in Fig. 3.3), which has a wall thickness

of 0.508 mm and an outer diameter of 38.1 mm, and is 2.37 m long. The central tracking system consists of two major sub-systems:

(1) Silicon microstrip tracker (SMT).

The SMT has barrel modules interspersed with disks in the center and assemblies of disks in the forward regions, as shown in Fig. 3.4. There are six barrels in the central region. Each barrel has four silicon readout layers. The centers of the barrels are located at $|z| = 6.2, 19.0, 31.8$ cm. Each barrel is capped at high $|z|$ with a disk of 12 double-sided (DS) wedge detectors, called "F-disks". Forward of the three "barrel|disk" assemblies is a unit consisting of three F-disks on each side. In the far forward regions, two larger-diameter disks, called "H-disks", provide tracking at high η. Twenty-four single-sided (SS) wedges are mounted on each H-disk. The centers of the F-disks are located at $|z| = 12.5, 25.3, 38.2, 43.1, 48.1, 53.1$ cm, and the H-disks are at $|z| = 100.4, 121.0$ cm.

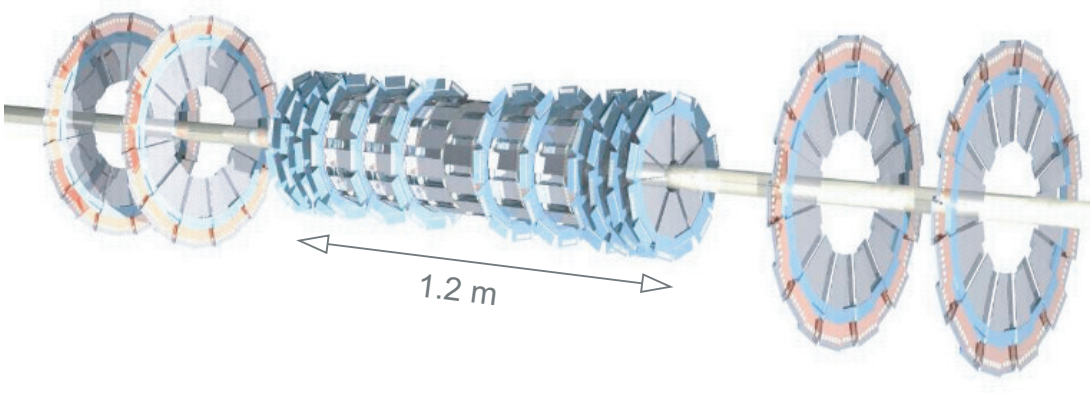

Figure 3.4: The disk/barrel design of the silicon microstrip tracker.

The SMT provides both tracking and vertexing over nearly the full η_{det} coverage of the calorimeter and muon systems. The barrels primarily measure the r-ϕ coordinate and the disks measure r-z as well as r-ϕ. The vertices for particles at high η_{det} are thus reconstructed in three dimensions by the disks, and vertices of particles at small η_{det} are measured by the barrels and the central fiber tracker (CFT).

(2) CFT.

The CFT consists of scintillating fibers mounted on eight concentric support cylinders and occupies the radial space from 20 to 52 cm from the center of the beampipe. To accommodate the forward SMT H-disks, the two innermost cylinders are 1.66 m long; the outer six cylinders are 2.52 m long. The scintillating fibers, including the cladding, are 835 μm in diameter. Each cylinder supports one doublet layer of fibers oriented along the beam direction (z) and a second doublet layer at a stereo angle in ϕ of $+3^\circ$ (u) or -3° (v). From the smallest cylinder outward, the fiber doublet orientation is $zu - zv - zu - zv - zu - zv - zu - zv$. The light is observed from only one end of each scintillating fiber. The opposite end of each scintillating fiber is mirrored with a sputtered aluminum coating that provides a reflectivity of about 90%. The CFT provides a coverage of $|\eta_{det}| \leq 1.7$.

By combining signals from both SMT and CFT, the two tracking detectors locate the primary interaction vertex with a resolution of about 35 μm along the beamline. They can tag b-quark jets with an impact parameter resolution of better than 15 μm in the r-ϕ plane for particles with transverse momentum $p_T > 10$ GeV at $\eta_{det} = 0$.

3.2.2 Calorimeters

The calorimeters are designed to provide identification and energy measurements for electrons, photons and jets, as well as the transverse energy imbalance. The calorimeter system consists of three sampling calorimeters and an intercyostat detector (ICD). The central calorimeter (CC) covers $|\eta_{det}| \leq 1$ and the two endcap calorimeters (EC) extend coverage to $|\eta_{det}| \approx 4$. As shown in Fig. 3.5, each calorimeter contains an electromagnetic (EM) section closest to the interaction region followed by fine and coarse hadronic sections. The active medium for the calorimeters is liquid argon and each of the three calorimeters is located within its own cryostat that maintains the detector temperature at approximately 90K. Different absorber plates are

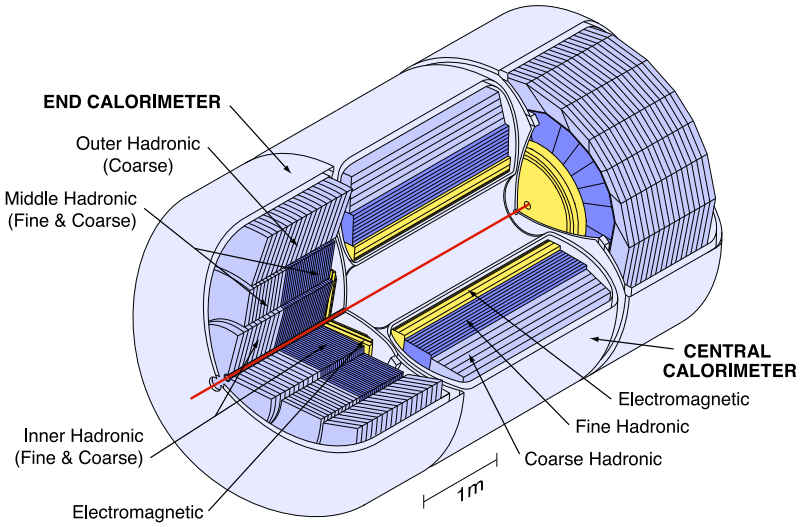

Figure 3.5: Isometric view of the CC and two EC.

used in different locations. The EM sections use thin plates (3 mm in the CC and 4 mm in the EC), made from nearly pure depleted uranium. The hadronic sections are made from 6-mm-thick uranium-niobium (2%) alloy. The coarse hadronic modules contain relatively think (46.5 mm) plates of copper (in the CC) or stainless steel (in the EC).

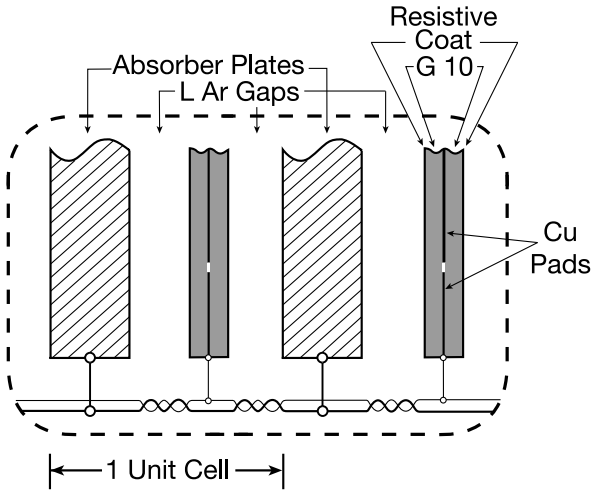

Figure 3.6: Schematic view of the liquid argon gap and signal board unit cell for the calorimeter.

A typical calorimeter cell is shown in Fig. 3.6. The electric field is established by

grounding the metal absorber plates and connecting the resistive surfaces of the signal boards to positive high voltage (typically 2.0 kV). The electron drift time across the 2.3 mm liquid argon gap is approximately 450 ns. Signal boards are made from two 0.5 mm G-10 sheets. For one sheet, one surface is bare G-10, while the one facing the inner surface of the second sheet, originally copper-coated, is milled into the pattern necessary for segmented readout. Several such pads at approximately the same η_{det} and ϕ are ganged together in depth to form a readout cell.

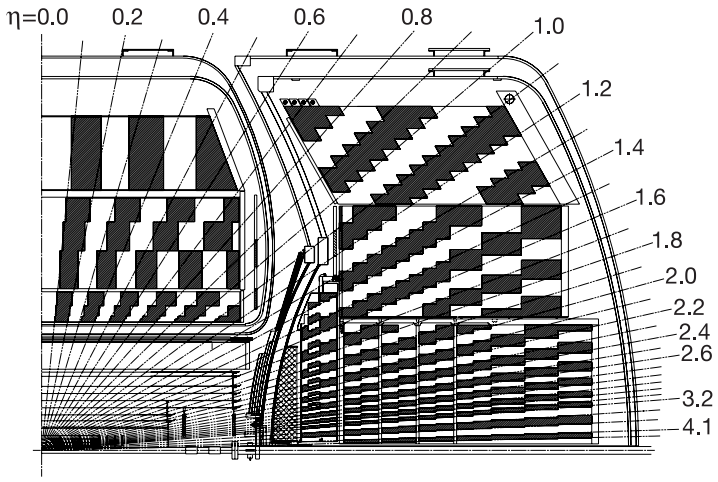

Figure 3.7: Schematic view of a portion of the calorimeters showing the transverse and longitudinal segmentation pattern. The shading pattern indicates groups of cells ganged together for signal readout. The rays indicate η_{det} intervals from the center of the detector.

Calorimeter readout cells form pseudo-projective towers as shown in Fig. 3.7, with each tower subdivided in depth. There are four separate depth layers for the EM modules in the CC and EC. In the CC, the layers are approximately 1.4, 2.0, 6.8, and $9.8X_0$[1] thick. In the EC, they are approximately 1.6, 2.6, 7.9, and $9.3X_0$ thick. The detector components between the interaction region and the first active gap in the CC at $\eta_{det} = 0$ provide about $4.0X_0$ of material; those between the interaction

[1]Radiation length X_0: average thickness of material that reduces the mean energy of the charged particle by a factor of e. The value of X_0 for uranium is typically 3.2 mm [27].

region and the first active gaps of the EC at $\eta_{det} = 2$ are $4.4X_0$ thick.

In the CC, the fine hadronic modules have three longitudinal gangings of approximately 1.3, 1.0, and $0.76\lambda_A$[2]. The single coarse hadronic module has a thickness of about $3.2\lambda_A$. The two EC have inner and outer radii of 3.92 and 86.4 cm, respectively. The fine hadronic portion consists of four readout cells, each $1.1\lambda_A$ thick. The coarse hadronic portion has a single readout cell that is $4.1\lambda_A$ thick. Each of the EC middle hadronic modules has four fine hadronic readout cells of about $0.9\lambda_A$ each and a single coarse hadronic section of $4.4\lambda_A$. The outer hadronic modules of the ECs are made from stainless steel plates inclined at an angle of about 60° with respect to the beam axis. The maximum thickness is $6.0\lambda_A$.

The transverse sizes of the readout cells are comparable to the transverse sizes of showers: 1-2 cm for EM showers and about 10 cm for hadronic showers. Towers in both EM and hadronic modules are $\Delta\phi = 2\pi/64 \approx 0.1$. The third layer of the EM modules, located at the EM shower maximum, is segmented twice as finely in both η and ϕ to allow more precise location of EM shower centroids.

3.2.3 Preshower detectors

The preshower detectors aid in electron and photon identification and background rejection for both triggering and offline reconstruction. The detectors can also be used offline to correct the EM energy measurement of the central and end calorimeters for losses in the solenoid and upstream material, such as cables and supports. Their fast energy and position measurements allow preshower information to be included in the Level 1 trigger.

The central preshower (CPS) detector covers the region $|\eta_{det}| < 1.3$, and consists of three concentric cylindrical layers of triangular scintillator strips and is located in the nominal 5 cm gap between the solenoid and the CC (as shown in Fig. 3.3). The

[2]Interaction length λ_A: mean free path for protons in material. The typical value of λ_A for uranium, copper and iron are 10.5, 15.1 and 16.8 cm respectively [27].

three layers of scintillator are arranged in an $z-u-v$ geometry, with a u-stereo angle of 23.774° and a v-stereo angle of 24.016°. Between the solenoid and the CPS is a lead radiator which is 7/32 inch thick and 103 inch long. The solenoid itself is $0.9X_0$ thick, providing a total of about $2X_0$ of material for particles at normal incidence, increasing to about $4X_0$ at the largest angles.

The forward preshower (FPS) detectors cover $1.5 < |\eta_{det}| < 2.5$. Two FPS detectors (north and south) are mounted on the spherical heads of the EC cryostat, occupying the region between the luminosity monitor at the inner edge and the intercryostat detectors at the outer edge (see Fig. 3.3). Each detector is made of two layers, at different z, of two planes of scintillator strips; and the two layers are separated by a $2X_0$-thick lead-stainless steel absorber. The inner-side (near to the interaction region) layers are referred as the minimum ionizing particle, or MIP, layers while the outer layers are called the shower layers. Different types of particles have different signal characteristics in these two layers:

- Electrons: when charged particles passing through the MIP layer they will register minimum ionizing signals in that layer; electrons will readily shower in the absorber, leading to a cluster of energy, typically on the order of three strips wide in the shower layer that is spatially matched with the MIP layer signal.

- Heavier charged particles: they will produce a similar MIP signal as electrons in the MIP layer; but heavier charged particles are less likely to shower, so they typically produce a second MIP signal in the shower layer.

- Photons: they will not generally interact in the MIP layer so no signal from that layer, but they will produce a shower signal in the shower layer.

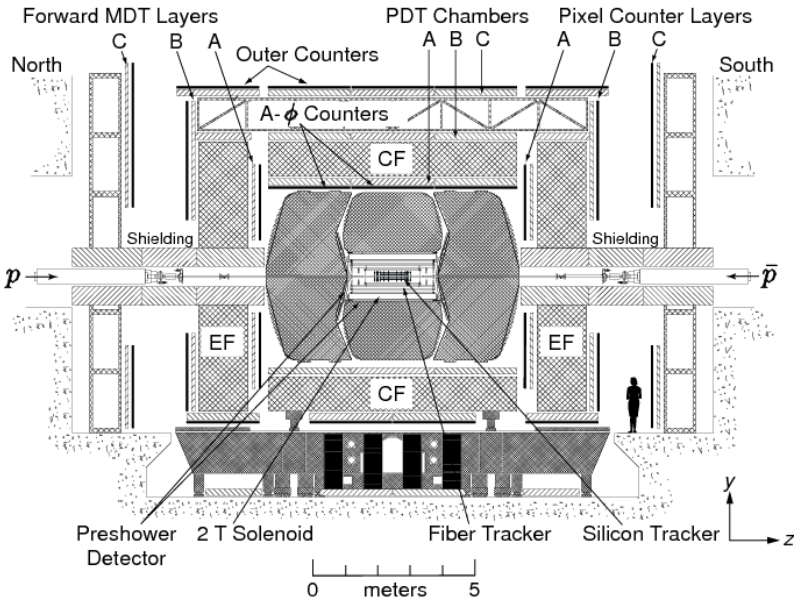

Figure 3.8: Cross-sectional view of the DØ Run 2 detector.

3.2.4 Muon system

The main components of the DØ Run 2 muon system are identified in Fig. 3.8. It consists of one layer of muon detectors (referred to as A in Fig. 3.8) before the toroidal magnet and two similar layers of detectors (referred to as B and C in Fig. 3.8) after the magnet. This provides the ability to reconstruct and measure the muon track parameters. Because of energy loss in the calorimeter, a muon produced in the $p\overline{p}$ interaction region must have a minimum energy of 2 to 2.5 GeV depending on the path, to pass through the calorimeter and reach layer A of the muon system. The muon energy must be at least 3 to 5 GeV to pass through both the uranium calorimeter and the iron toroid to reach all instrumented layers of the muon system.

For the purposes of triggering, a system of fast scintillation counters with time resolution of $\sigma(t) \approx 2$ ns is used. In the central muon system ($|\eta_{det}| \leq 1.0$) there are 630 scintillation counters in the A-layer (referred to as Aϕ counters), with an angular segmentation of 79 mrad in ϕ, and 372 counters in the C-layer (referred to as outer counters). In the forward region, which covers $1.0 \leq |\eta_{det}| \leq 2.0$, a total of

4214 scintillation counters (referred to as pixel counters) are used in the A, B, and C layers, providing three independent coordinate and time measurements along muon tracks. They have a segmentation of approximately 0.1 in η and approximately 79 mrad in ϕ.

The muon system tracking detectors consist of proportional drift tubes (PDTs) in the central region and mini drift tubes (MDTs) in the forward region. Both PDTs and MDTs are installed in the three layers, A, B, and C, which consist of 4, 3 and 3 detection planes, respectively (except the bottom A layer PDTs which have three planes). In the central region, approximately 55% of the central region is covered by three layers of PDTs and close to 90% is covered by at least two layers. A PDT cell, which is 10.1 cm across, contains seven gold-plated tungsten sense wires, read out at one end, and two delay lines located just before (after) the first (last) sense wires, each read out at both ends. Along with an anode wire at the center of each cell, vernier cathode pads [30] are located above and below the wires to provide information on the hit position along the wire. The gas mixture is 84% argon, 8% methane, and 8% CF_4. The operating high voltage is 2.3 kV for the pads and 4.7 kV for the wires. The drift velocity is approximately 10 cm/μs, for a maximum drift time of about 500 ns. For each PDT hit, the following information is recorded: the electron drift time, the time difference ΔT in the arrival time of the signal pulse at the end of the hit cell's wire and at the end of its readout partner's wire, and the charge deposition on the inner and outer vernier pads. Both ΔT and the charge deposition are used to determine the hit position along the wire. The single-wire resolution is approximately 1 mm due to the electron diffusion. In the forward region, MDTs are chosen for their short electron drift time (below 132 ns), good coordinate resolution (less than 1 mm), radiation hardness, high segmentation, and low occupancy. An MDT tube consists of eight cells, each with a 9.4×9.4 mm^2 internal cross-section and a 50 μm W-Au anode wire in the center. The MDT system uses a $CF_4 - CH_4$ (90-10%) gas mixture.

It is non-flammable, fast, exhibits no radiation aging, and has a wide operational plateau. Negative high voltage is applied to the cathode (-3200 V) and the anode wire is grounded. The maximum drift time for tracks that are perpendicular to the detector plane is 40 ns; for tracks inclined at 45°, the maximum drift time is 60 ns. The single cell resolution is measured to be 0.8 mm. The PDTs and MDTs provide high-accuracy coordinate measurements with a resolution of approximately 1 mm in the direction perpendicular to the sensitive wires which are arranged parallel to the toroidal field lines.

3.2.5 Magnet Field

The magnetic field inside the DØ detector is provided by both the solenoidal magnet and the toroidal magnets. A y-z view of the magnetic field with both the toroid and solenoid magnets at full current is shown in Fig. 3.9. The overall magnetic field has x, z diagonal symmetry – at a fixed y coordinate, the absolute value of the magnetic field at ($+x$, $+z$) is equal to the absolute value of the field at (-x, -z). DØ takes data equally in two polarities to concel the possible systematics due to the asymmetry of magnetic field. The field is not up-down symmetric because the toroid itself is not symmetric and the detector sits on a magnetic steel platform.

The superconducting solenoidal magnet locates between the CFT and the CPS, and it is designed to optimize the momentum resolution and tracking pattern recognition within the available space (2.73 m in length and 1.42 m in diameter) [28].

The central toroid is a square annulus 109 cm thick whose inner surface is about 318 cm from the Tevatron beamline; it covers the region $|\eta_{det}| \lesssim 1$. The magnet is wound using 20 coils of 10 turns each. The two end toroids are located at $454 \leq |z| \leq 610$ cm. In the center of each end toroids is a 183 cm square hole centered on the beamline; in x and y the magnets extend 426 cm from the beamline. The end toroid windings are eight coils of eight turns each.

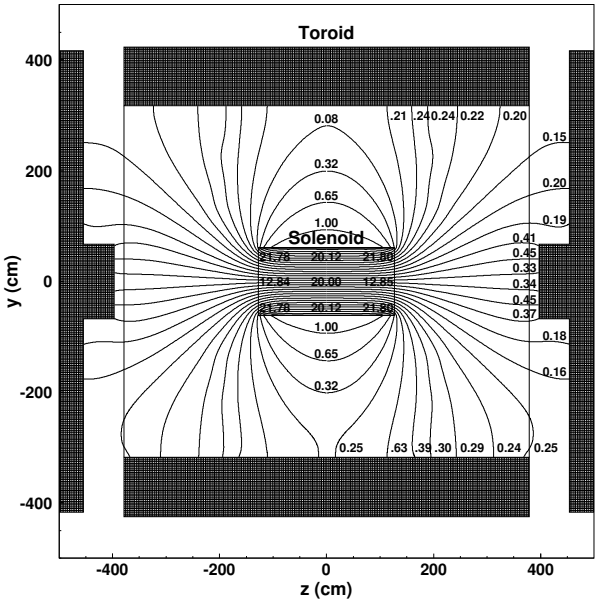

Figure 3.9: A y-z view of the DØ magnetic field (in kG) with both the toroidal and solenoidal magnets at full current (1500 and 4749 A, respectively). The field lines are projections onto the y-z plane.

The relative alignment between the solenoid and toroid is known to be 0.5-0.1 cm. If the solenoid is shifted 1 cm in the z direction, the variation in the momentum measurement is 0.1%; a $\pm$ 1 cm shift of the solenoid in the transverse direction gives a relative systematic error in the momentum of about 0.01%. A $\pm$1 cm shift of the toroid in the z direction gives an error of about 0.002% [26].

3.2.6 Luminosity nomitor

The primary purpose of the luminosity monitor (LM) is to determine the Tevatron luminosity at the DØ interaction region. This is accomplished by detecting inelastic $p\overline{p}$ collisions with a dedicated detector. The LM also serves to measure beam halo rates and to make a fast measurement of the z coordinate of the interaction vertex. The LM detector consists of two arrays of 24 plastic scintillation counters with PMT readout located at $z = \pm$ 140 cm (left plot in Fig. 3.10). A schematic drawing of an array is shown as the right plot in Fig. 3.10. The arrys are located in front of the

EC and occupy the radial region between the beam pipe and the forward preshower detector. The counters are 15 cm long and cover $2.7 < |\eta_{det}| < 4.4$.

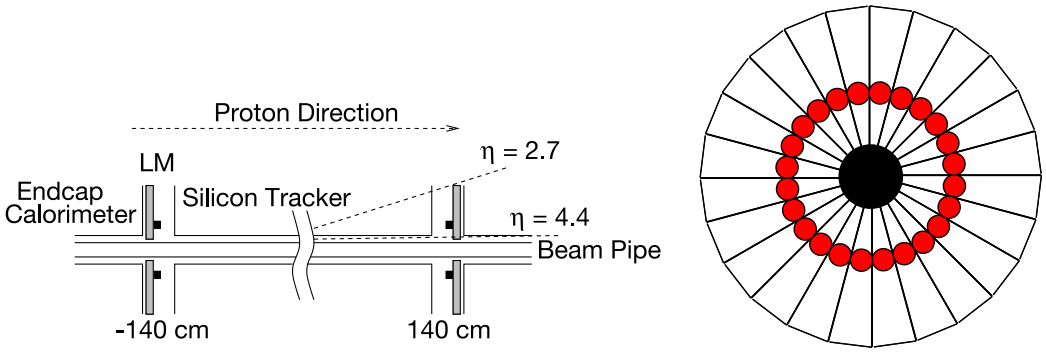

Figure 3.10: Schematic view of the location of the LM detector (left) and the geometry of the LM counters (right, solid dots showing the the locations of the PMTs)

3.2.7 Triggering

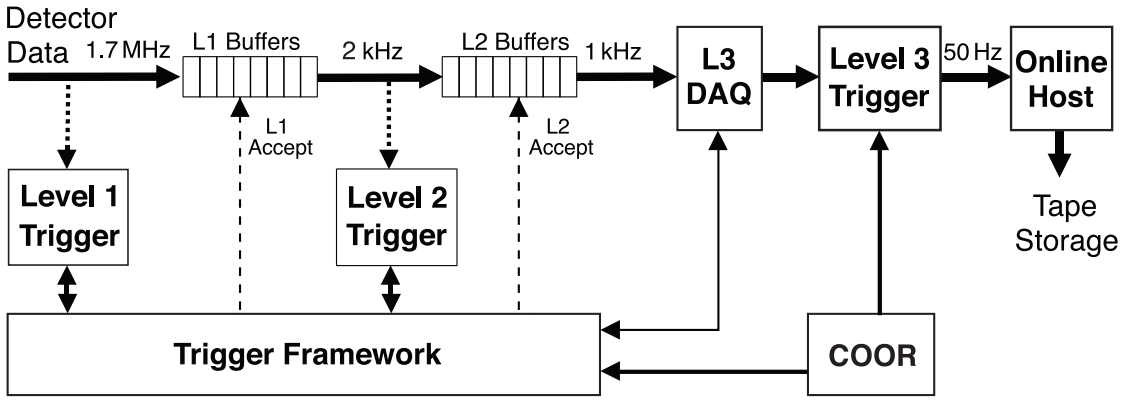

Figure 3.11: Overview of the DØ trigger and data acquisition systems.

With the increased luminosity and higher interaction rate delivered by the upgraded Tevatron, a significantly enhanced trigger is necessary to select the interesting physics events to be recorded. Three distinct levels form this new trigger system with each succeeding level examining fewer events but in greater detail and with more complexity. The first stage (Level 1 or L1) comprises a collection of hardware trigger

elements that provide a trigger accept rate of about 2 kHz. In the second stage (Level 2 or L2), hardware engines and embedded microprocessors associated with specific subdetectors provide information to a global processor to construct a trigger decision based on individual objects as well as object correlations. The L2 system reduces the trigger rate by a factor of about two and has an accept rate of approximately 1 kHz. Candidates passed by L1 and L2 are sent to a farm of Level 3 (L3) microprocessors; sophisticated algorithms reduce the rate to about 50 Hz and these events are recorded for offline reconstruction. An overview of the DØ trigger and data acquisition system is shown in Fig. 3.11.

A block diagram of the L1 and L2 trigger systems is shown in Fig. 3.12.

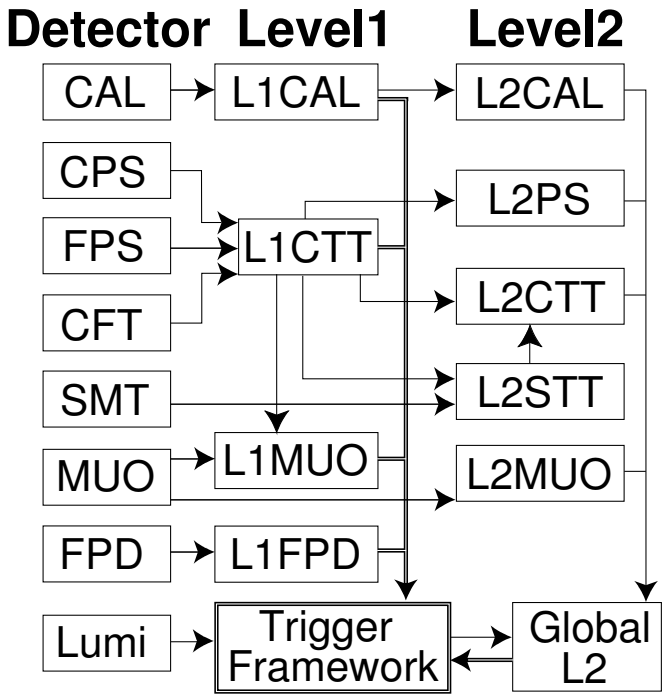

Figure 3.12: Block diagram of the DØ L1 and L2 trigger systems. The arrows show the flow of trigger-related data.

L1 is implemented in specialized hardware and examines every event for interesting features. The calorimeter trigger (L1Cal) looks for energy deposition patterns exceeding programmed limits on transverse energy deposits; the central track trig-

ger (L1CTT) and the muon system trigger (L1Muon) compare tracks, separately and together, to see if they exceed preset thresholds in transverse momentum. The L1 forward proton detector trigger (L1FPD) is used to select diffractively-produced events by triggering on protons or antiprotons scattered at very small angles. All events awaiting L1 trigger decisions are pipelined and thus make minimal contributions to the deadtime. In order to participate in the trigger decision, the L1 trigger decision must arrive at the trigger framework in 3.5 μs or less. The rate of L1 trigger accepts is limited by the maximum readout rates of the participating subsystems and by a desire to minimize the deadtime associated with the readout.

The L2 trigger provides detector-specific preprocessing engines and a global stage (L2Global) to test for correlations in physics signatures across detector subsystems. The L2 trigger system was designed to handle input rates of up to 10 kHz with a maximum accept rate of 1 kHz. L2 preprocessors collect data from the front-ends and L1 trigger system and analyze these data to form physics objects. L2 can also combine data across detectors to form higher quality physics objects and examine event-wide correlations in all L2 physics objects. The L2Global processor selects events based on the set of 128 selections applied at L1 and additional script-controlled criteria. Events passing L2 are tagged for full readout and further analysis in the L3 trigger.

The L3 trigger provides additional rejection both to enrich the physics samples and to maintain an acceptable throughput which can be recorded to tape. As a high level, fully programmable software trigger, L3 performs a limited reconstruction of events, reducing a nominal 1 kHz input rate to 50 Hz for offline analysis. Its decisions are based on complete physics objects as well as on the relationships between these objects (such as the rapidity or azimuthal angle separation for physics objects or their invariant mass).

CHAPTER IV

Object Reconstruction and Identification

After an event is written to tape it undergoes a full offline event reconstruction. The basic reconstructed data (tracks, calorimeter clusters, etc) are used to reconstruct physics objects, such as muons, electron, jets, $\not\!\!E_{\rm T}$ and so on. MC events will pass through the Geant3 [31] simulation and digitization to have the same format as real data, then they will go through the same reconstruction algorithm. In this chapter the object identifications and their efficiencies are described.

4.1 Primary Vertices

The reconstruction and identification of primary vertices consist of the following three steps:

(1) Track selection.

All tracks in the event passing the criteria:

- $p_T > 0.5$ GeV
- 2 or more SMT hits if the track $\eta - z$ is within the SMT geometric acceptance

are extrapolated back to a common point of origin along the z-axis. A z-clustering algorithm, which clusters tracks within 2 cm, is used to identify tracks belonging to different interactions.

(2) Vertex fitting.

The Adaptive vertex fitter algorithm [32] is used to get the location of each vertex. In this, track errors are reweighted according to their χ^2 contribution to the vertex, which is designed to reduce the contribution of distant tracks to the vertex fit.

(3) Primary vertex selection.

In order to separate the primary vertex from all vertices identified in the procedure above, a probabilistic approach is used [33]. Assuming that tracks from hard scattering have higher p_{T} than tracks from minimum bias (MB) vertices, the probability of a track coming from MB interaction could be achieved. For each selected vertex, the MB probability is calculated by multiplying the probability of all tracks associated with this vertex. The primary vertex is then selected as the one with the smallest MB probability. To ensure that a hard-scatter vertex of high quality is selected, it is required to be reconstructed from at least three tracks and have $|z_{PV}| \leq 50$ cm.

4.2 Muons

To reconstruct muon trajectories, the same algorithm is used in both the forward and central regions. A list of hits from the muon detector is first built. These hits are associated to form muon track segments, which are then used to form tracks in the muon system, called local tracks. The local tracks and the segments not used in the construction of local tracks are generically called local muons. A typical prompt muon candidate is defined by the presence of a local track in the muon system and a matched isolated track in the inner tracker. It has been found that the local muon momentum resolution is inferior to the resolution from the central tracking system, thus the momentum of a muon matched to a central track is taken to be the momentum measured in the central tracker. Despite the relatively high amount of energy lost by a muon in the calorimeter, the energy deposit of muons in an individual cell is close to the threshold level of the calorimeter noise-suppression algorithm, and

is therefore not well measured. Thus, the calorimeter information is not exploited to identify high-p_{T} muons but is used for muon identification in heavy flavor analyses.

The quality of a muon object is determined by three aspects: the muon identification in the muon system, the track reconstruction, and the isolation.

4.2.1 Identification criteria in the muon system

For the identification of local muon, three categories `loose`, `medium`, and `tight` are defined as follows.

- `loose`: a local muon has (a) at least one scintillator hit and at least two wire hits in the A layer of the muon system, or (b) at least one scintillator hit and at least two wire hits in the BC layers.

- `medium`: in the general case, a local muon is `medium` if it meets both conditions of (a) and (b), except that for $|\eta_{det}| < 1.6$, the BC scintillator requirement is dropped. For the particular case of the bottom part of the detector, where the support structure for the calorimeter is located ($\frac{5\pi}{4} < \phi < \frac{7\pi}{4}$ and $|\eta_{det}| < 1.6$), a local muon is `medium` if it fulfills either condition (a) or (b). In the particular case of a low-p_{T} muon, a local muon is `medium` if it fulfills condition (a), as its probability to reach the BC-layer is less than 70% due to energy loss in the toroid.

- `tight`: a local muon which belongs to the category of `medium` muons that meet both conditions (a) and (b), except that for $|\eta| < 1.6$, the BC scintillator requirement is dropped.

The number of categories is doubled depending on whether or not a veto against cosmic muons is required. The cosmic veto criterion demands that the scintillator hit times in each layer, if available, be consistent within 10 ns with those of a particle moving at the speed of light from the primary vertex. By default, the cosmic veto is

applied and it has a typical efficiency of about 98.5% for high-p_{T} muons. The muon identification criteria without the timing cuts are denoted by `looseNCV`, `mediumNCV` and `tightNCV`. The efficiencies of the identification in the muon system are shown in Fig. 4.1. The average reconstruction efficiencies are 88.9%, 80.8% and 72.0% for `loose`, `medium`, and `tight` operating points, respectively. If the cosmic veto is not required, these efficiencies increase to 90.9%, 82.5% and 73.1%, respectively.

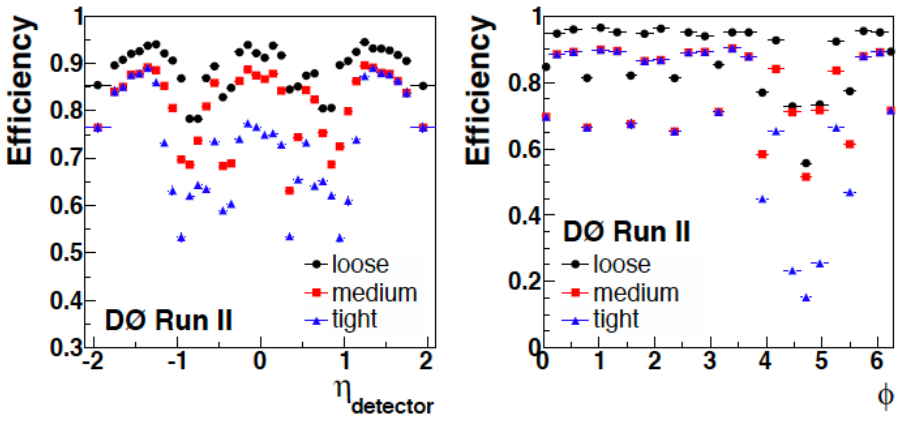

Figure 4.1: Efficiencies of the muon identification criteria in the muon system as functions of η_{det} (left) and ϕ (right).

4.2.2 Identification criteria in the central tracker

To control the purity of muons matched to central tracks, different qualities of track have been defined. They rely on the following track characteristics: (i) number of hits either in the SMT or CFT system; (ii) χ^2 per degree of freedom ($\chi^2/d.o.f.$) of the central track fit; (iii) *dca*: transverse impact parameter (distance of closest approach) with respect to the beamline. Four central track quality categories are defined: `trackloose`, `trackmedium`, `trackmediumSMT` and `tracktight`.

- `trackloose`: a track with $|dca| < 0.2$ cm. If the track has SMT hit the cut is tighten to $|dca| < 0.04$ cm;

- `trackmedium`: a track fulfills the `trackloose` requirement and $\chi^2/d.o.f. < 9.5$ and has at least 2 CFT hits;
- `trackmediumSMT`: a track fulfills the `trackmedium` requirement and has hits in SMT;
- `tracktight`: a track fulfills the `trackloose` requirement and $\chi^2/d.o.f. < 4$.

The efficiencies of the identification in the tracking system are shown in Fig. 4.2. The average efficiencies are 91.6%, 90.5%, 84.6% and 86.2% for the `trackloose`, `trackmedium`, `trackmediumSMT` and `tracktight` operating points, respectively.

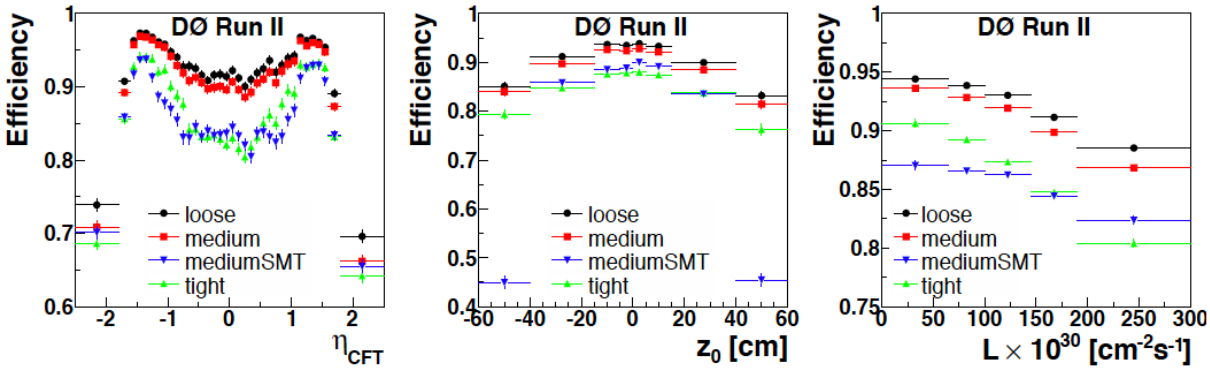

Figure 4.2: Efficiencies of the muon identification criteria in the tracking system as functions of η_{CFT} (left), z_0 (middle) and instantaneous luminosity (right).

4.2.3 Muon isolation

We select isolated muons arising from the primary vertex by rejecting secondary muons from semi-leptonic decays of b or c quarks, which are surrounded by additional particles due to quark fragmentation and other heavy hadron decay products. Three basic discriminating variables are formed:

- $\Delta R(\mu, jet) \equiv \sqrt{\Delta\eta^2(\mu, jet) + \Delta\phi^2(\mu, jet)}$ is the closest distance in the (η, ϕ) space of the muon to any jet with $p_{\mathrm{T}} > 15$ GeV, where the jets are reconstructed with a cone of radius 0.5.

- $I^{trk} \equiv \sum_{trk \in \Delta R < 0.5} p_T^{trk}$, is the scalar sum of transverse momenta of all tracks inside a $\Delta R(trk, \mu) < 0.5$ cone around the muon track with the exception of the muon track itself. To reject the contributions of tracks arising from other $p\overline{p}$ interactions in the same bunch crossing, the requirement of $\Delta z_0(\mu, trk) < 2$ cm is demanded for each track in the sum, where z_0 is the coordinate of the track at the point of closest approach to the beam axis.

- $I^{cal} \equiv \sum_{trk \in 0.1 < \Delta R < 0.4} E_T^{cluster}$, is the scalar sum of transverse energies of all calorimeter clusters inside a hollow cone around the muon defined by $0.1 < \Delta R(\mu, cluster) < 0.4$. Only energy deposits in the electromagnetic calorimeter and the first fine sampling layer of the hadron calorimeter are considered to reduce the impart of noise and other $p\overline{p}$ interactions in the same bunch crossing.

We also employ isolation variables I^{trk}/p_T^{μ} and I^{cal}/p_T^{μ} which offer higher efficiencies for high-p_{T} muons and more stringent rejection against secondary leptons from b and c quark decays at low p_{T}. Based on these five variables, several isolation criteria are defined as shown in Tab. 4.1, and their efficiencies are shown in Fig. 4.3. The efficiencies of isolation requirements are in the range of 87.3% to 98.6%, depending on the operating points.

Table 4.1: Muon isolation operating points

Operating point	I^{trk}	I^{cal}	I^{trk}/p_T^{μ}	I^{cal}/p_T^{μ}	$\Delta R(\mu, jet)$
`scaledLoose`	–	–	<0.20	<0.20	>0.5
`scaledMedium`	–	–	<0.15	<0.15	>0.5
`scaledTight`	–	–	<0.10	<0.10	>0.5
`tight`	< 2.5 GeV	< 2.5 GeV	–	–	>0.5
`trkTight`	< 2.5 GeV	< 10 GeV	–	–	>0.5
`trkScaledLoose`	–	–	<0.25	<0.40	>0.5
`trkScaledTight`	–	–	<0.12	<0.40	>0.5
`jetIso`	–	–	–	–	>0.5

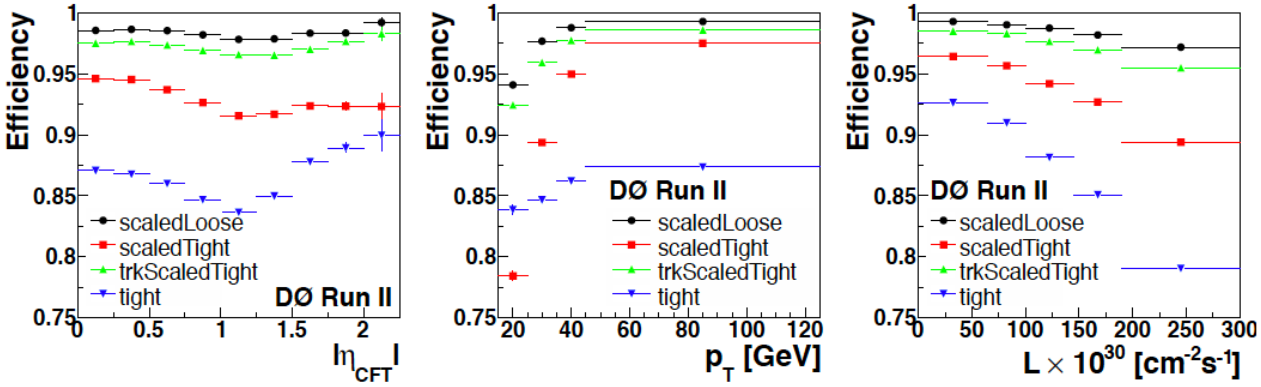

Figure 4.3: Efficiencies of the muon isolation criteria as functions of $|\eta_{CFT}|$ (left), p_{T} (middle) and instantaneous luminosity (right).

4.2.4 Muon Momentum resolution

The resolution of the muon momentum measured in the tracking system can be modeled by:

$$\sigma(\frac{1}{p_T}) = \frac{R_{CFT}^2}{L_{arm}^2}\sqrt{A^2 + \frac{B^2 \cosh\eta}{p_T^2}}, \tag{4.1}$$

where A is the resolution term related to the detector alignment and hit resolution, B describes the effect of multiple Coulomb scattering, $R_{CFT} = 52$ cm is the outer radius of the CFT detector, and L_{arm} is the radius corresponding to the outermost CFT hit along the track. The term R_{CFT}/L_{arm} is a correction that accounts for the lever arm used to measure the track momentum. Values of A and B are shown in Tab. 4.2. The typical resolution is $10\% - 16\%$ for tracks of $p_T = 40$ GeV.

Table 4.2: Muon momentum resolution parameters

Track Type	$A \times 10^3$ (GeV^{-}1)	$B \times 10^2$
With SMT hits	2.3 ± 0.2	2.5 ± 0.3
With SMT hits, $\|\eta_{CFT}\| > 1.6$	2.7 ± 0.4	2.2 ± 0.7
Without SMT hits	4.1 ± 0.7	2.9 ± 1.1

4.3 Jets

The hadronization of particles gives rise to jets. At the detector level, jets are made of calorimeter towers or cells, after energy deposition in the calorimeter by electromagnetic showering, hadronic showering, and ionization. Jet objects used in this analysis is called JCCB jets, which are reconstructed with Run 2 cone algorithm [44] on calorimeter towers with a cone size of $R_{cone} = 0.5$ in the $\eta - \phi$ plane.

The jets found using the jet finding algorithm are required to pass further quality criteria in order to remove fake jets:

- The total number of calorimeter towers that contain 90% of a jet's energy has to be larger than one, to reduce noise jets coming from a single hot cell;
- The ratio of the highest to next-to-highest E_{T} cell has to be smaller than 10 in order to remove jets clustered from hot cells.
- Reduction of electromagnetic and noise-like jets is obtained by requiring that the fraction of the energy deposited in the electromagnetic calorimeter is between 5% and 95%.
- Because of higher noise in the coarse hadronic layers compared to the other layers of the calorimeter, the energy fraction in this layer is required to be less than 40% of the jet energy.

4.3.1 Jet energy scale

The energy calibration of a jet is fundamentally different than for any other object in particle physics, since it does not correspond to a single well-defined particle such as an electron or a muon. The measured energy of a jet is not fully correlated to energy of its progenitor parton due to two effects: the parton-to-hadron fragmentation that leads to the creation of the jet, and the interaction of the final state hadrons with

the detector. The goal of the jet energy scale correction is to relate, on average, the jet energy measured in the detector to the energy of the final state particle jet. The particle jet energy E^{ptcl} can be related to the measured energy E^{meas} of the reconstructed jet via:

$$E^{ptcl} = \frac{E^{meas} - E_O}{R \cdot S} \tag{4.2}$$

where:

- E_O represents an offset energy, which results from electronics noises, pile-up, underlying events and so on;
- R represents the response of the calorimeter to the energy of the particles comprising the jets. This value is generally smaller than unity, because significant energy is lost in the non-sampled material before the calorimeter, and in non-instrumented regions between calorimeter modules.
- The function S represents corrections for the showing of particles in the detector. Due to the cone size algorithm in the reconstruction of a jet, energy from particles originating within a jet can spread to cells outside the cone radius. Conversely, energy deposited in cells inside this cone may be originated from other particle jets. Typically, this correction is close to unity.

The details about the determination of all parameters/function in Eqn. 4.2 can be found in [46]. Figure. 4.4 shows the magnitude of the total correction for jets energy, and Fig. 4.5 shows the size of the jets energy scale uncertainty. The overall correction factor to the jet energy in the CC varies within 1.4 - 1.5 (1.25 - 1.3) for jets $p_T = 25$ GeV (100 GeV). The total uncertainties at the same energies are within 1.4% - 1.8% in the CC, while at $|\eta_{det}| \sim 3.0$ the uncertainties increase to 3% - 3.5%. For b-jets, this uncertainty increases to 6% - 8%.

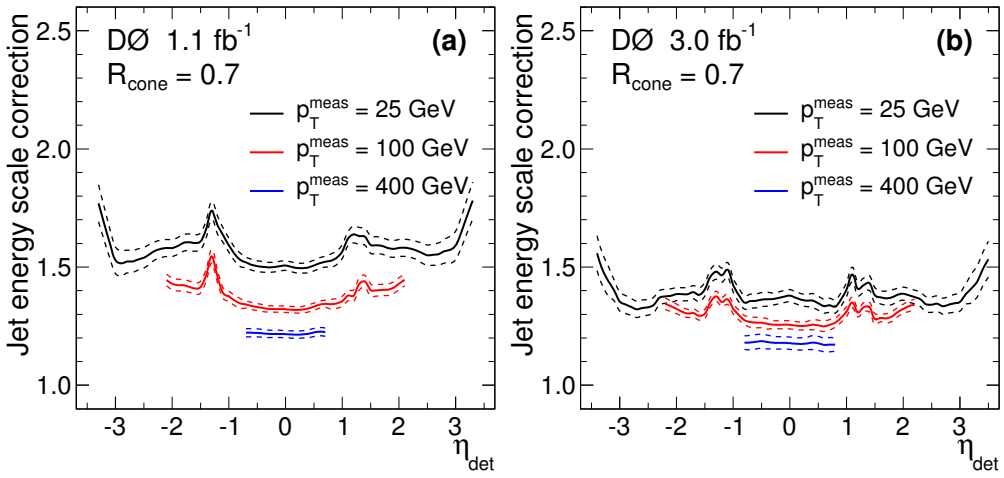

(a) (b)

Figure 4.4: Jet energy scale corrections, E^{ptcl}/E^{meas}, in (a) Run 2A and (b) Run 2B as a function of η_{det} for different uncorrected jet p_T value.

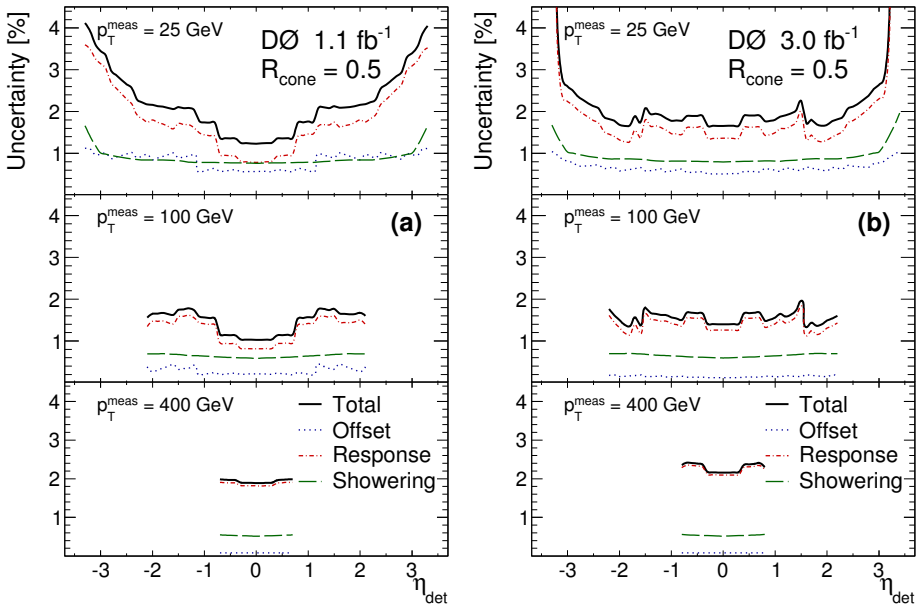

(a) (b)

Figure 4.5: Jet energy scale uncertainty in (a) Run 2A and (b) Run 2B as a function of η_{det} for different uncorrected jet p_T value.

4.4 B-tagging

The b quark occupies a special place among the fundamental fermions: on one hand, its mass (of the order of 5 GeV) is substantially larger than the mass of a

c quark. On the other hand, it is light enough to be produced copiously at high energy colliders. In particular, unlike the top quark, the b quark is lighter than the W boson, preventing decays to on-shell W bosons. As a result, it lives long enough for hadronization to occur before its decay. The average lifetime of b-flavored hadrons has been measured to be about 1.5 ps: this is sufficient long for b hadrons, even of moderate momentum, to travel distances in the order of mm. Combined with the relatively large mass of b hadrons, the use of precise tracking information allows the detection of the presence of b hadrons through their charged decay products. In addition, b hadron decays often lead to the production of high momentum leptons; especially at hadron colliders. The observation of such leptons provides easy access to samples with enhanced b-jet content. The identification of jets originating from the hadronization of b quarks are usually referred to as b-jet identification or b-tagging.

4.4.1 Jet taggability

The jet tagging algorithms described in the following sections are based entirely on tracking and vertexing of charged particles. Therefore, a very basic requirement is that there should be charged particle tracks associated with the (calorimeter) jet. Rather than incorporating such basic requirements in the tagging algorithms themselves, they are implemented as a separate step, which is called the taggability of a jet at DØ. The requirement for a jet to be taggable is that it should be within $\Delta R = 0.5$ from a so-called track jet. Track jets are reconstructed with a cone size of 0.5, starting from tracks having at least one hit in the SMT, a distance to the selected primary vertex less than 2 mm in the transverse plane and less than 4 mm in the z direction, and $p_T > 1$ GeV. Figure 4.6 shows the taggability efficiency as a function of z' and p_{T}.

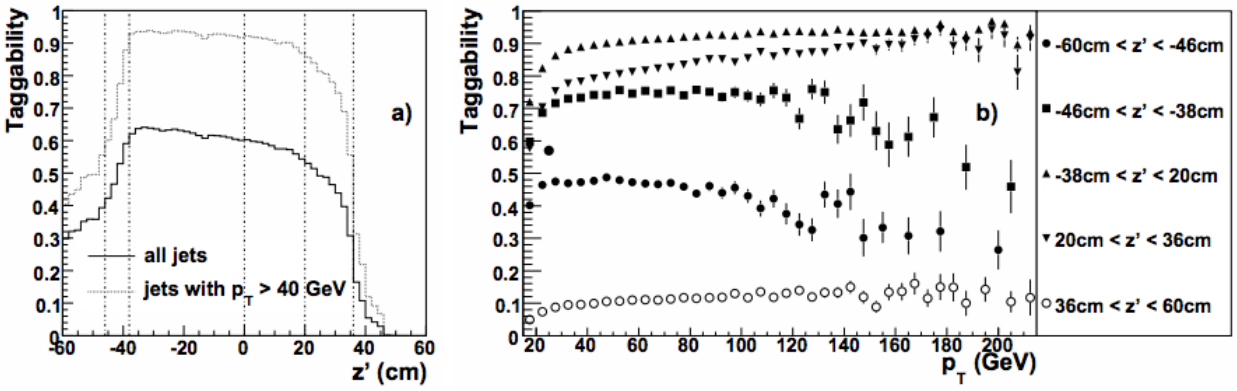

Figure 4.6: (left): taggability as a function of $z' \equiv |z| \times sign(\eta \times z)$. The vertical lines denote the boundaries chosen for the parametrization in p_{T} and $|\eta|$. (b): taggability as a function of jet p_{T}, in different bins of z'. The curves for the two central bins are very similar and have been combined.

4.4.2 B-tagging algorithms

There are three "intermediate" tools certified at DØ to identify (tag) whether a jet is produced from a b quark or not:

(1) Secondary Vertex Tagging (SVT) [47]. The vast majority of b-hadron decays give rise to multiple charged particles emanating from the b-hadron's decay point. The most intuitive tagging method is therefore to attempt to reconstruct this decay point explicitly and to require the presence of a displaced or secondary vertex. After the identification and selection of the primary interaction vertex, the reconstruction of secondary vertices starts from the track associated with each taggable calorimeter jet. The tracks considered must satisfy some selection criteria [47] to remove the effect from misreconstructed tracks. With different track selection cuts, there are 5 types of "SVT configurations", which are SuperLoose (SL), MediumLoose (ML), Loose "X-tra" (LX), Loose (L) and Tight (T). The SVT is no longer used as the final b-tagger tool in most of DØ analysis, but for each type of SVT configuration 27 variables [51] relevant to SVT are taken as input variables for the training of the MVA tagger (see Sect. 4.4.3).

(2) Jet Lifetime Probability Tagger (JLIP) [48]. Given the impact parameter value of a track, its probability to originate from the primary vertex can be calculated [48]. The probabilities of all tracks matched to a jet are then combined into one variable called the Jet Lifetime Probability (P_{JLIP}), which can be interpreted as the confidence level that all tracks in a jet originate from the primary vertex. Jets from light quark fragmentation are expected to present a uniform P_{JLIP} distribution between 0 and 1, whereas jets from c and b quarks will exhibit a peak at a very low P_{JLIP} value. The P_{JLIP} is also taken as an input variable for the MVA tagger.

(3) Counting Signed Impact Parameters (CSIP) [49]. In this method, there is no attempt to use reconstructed secondary vertices. Instead, the signed impact parameter (IP) significance $S_d = IP/\sigma_{IP}$ with respect to the primary vertex is calculated for all good tracks located within a $\Delta R = 0.5$ cone around the jet axis. We count the number of tracks with an IP significance above a given threshold. A new variable is calculated basing on this method – $CSIP_{COMB}$, which is a combination of track multiplicities passing various impact parameter thresholds [50], and the $CSIP_{COMB}$ is also used as an input variable for the MVA tagger.

4.4.3 Combined multivariate b-tagging algorithms

The three taggers mentioned above have been combined with a Random Forest (RF) which shows significant performance improvements compared to each individual tagger [51]. The so-called BL btagger is trained with b-jets from the QCD bb production as the signal and light-jets from the QCD inclusive samples as the background respectively. The output of MVA BL tagger, and its b-jet tagging efficiency and light-jet fake rate are shown in Fig. 4.7 (NN is the old b-tagger at DØ, the performance of NN tagger is also shown in Fig. 4.7 for comparison. NN tagger is not described in the thesis because we are not using it in this analysis).

Based on the value of MVA BL tagger, 12 operating points are defined as shown in

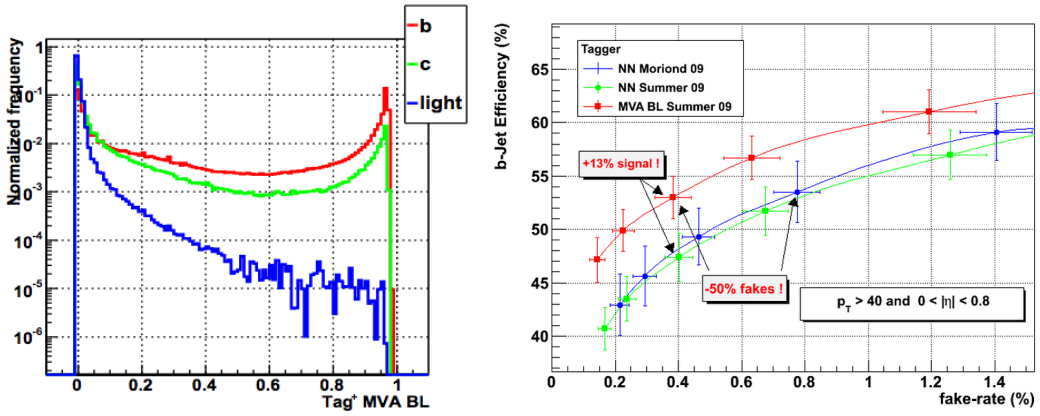

(a) (b)

Figure 4.7: Output of MVA BL tagger (left), the performance of MVA BL tagger (right).

Tab. 4.3. The efficiencies and scale factors for those 12 operating points are certified and provided by the B-ID group.

Table 4.3: Operating points of MVA BL tagger

Operating point	MVA BL cut (>)
MegaTight	0.925
UltraTight	0.9
VeryTight	0.85
Tight	0.775
Medium	0.65
oldLoose	0.5
Loose	0.45
L2	0.325
L3	0.25
L4	0.2
L5	0.15
L6	0.1

4.5 Electrons

The reconstruction algorithm of an EM object is similar to that of a jet object, except using a cone size of 0.2. The DØ EM ID group provides five definitions of electron ID, as shown in Tab. 4.4.

Table 4.4: Definition of EM ID

Definition	Point0		Point1		Point2		Point05	
	CC	EC	CC	EC	CC	EC	CC	EC
EMf[<]	0.90	0.90	0.90	0.90	0.90	0.90	0.90	0.97
IsoE0[<]	0.09	0.10	0.08	0.10	0.08	0.06	0.15	0.05
IsoHC4 [<]	4.0	eqn.1a	2.5	eqn.1a	2.5	eqn.1a	3.5	eqn.1b
Hmx7(CC)/Hmx8(EC)[<]	–	40	35	40	35	40	–	10
Sigphi[<]	–	eqn.2	–	eqn.2	–	eqn.2	–	eqn.2
NN7(CC)/NN4(EC)[>]	0.4	0.05	0.9	0.05	0.9	0.1	0.3	0.2
TrkMatch[>]	0.0	–	0.0	0.0	0.0	0.0	0.0	–
HoR[>]	0.6	–	–	–	–	–	–	–
Lhood8[>]	–	–	0.2	0.05	0.6	0.65	0.05	–
E/p[<]	–	–	8.0	–	3.0	6.0	8.0	–

eqn.1a IsoHC4 < 0.01 || IsoHC4 $<$ (-2.5 $\times|\eta_{det}| + 7.0$)
eqn.1b IsoHC4 < 0.01 || IsoHC4 $<$ (-2.0 $\times|\eta_{det}| + 5.0$)
eqn.2 $|\eta_{det}| \leq 2.6$: Sigphi $>$ (6.5 $\times(|\eta_{det}| - 0.82)^{-1} - 2.8$)

Some descriptions of variables listed in Tab. 4.4 are as follows.

- EMf: E_{EM}/E_{tot}, ratio of the energy deposited in the electromagnetic part of the calorimeter to the total energy including the hadronic calorimeter.

- IsoE0: $(E_{tot}^{R=0.4} - E_{EM}^{R=0.2})/E_{EM}^{R=0.2}$, calorimeter isolation is the fraction of calorimeter energy in the isolation region bound by the outer cone ($R = 0.4$) and the inner EM cluster cone ($R = 0.2$) to the energy of the EM cluster, the expected contributions from the MB interactions are subtracted from the energy in the isolation cone.

- IsoCH4: $\sum_{R>0.05}^{R<0.4} p_T^{trks}/E_{EM}^{R=0.2}$ track isolation calculated with the total track p_{T} (for tracks with $p_T^{trk} > 0.5$ GeV) in the hollow cone $0.05 < R < 0.4$ around the EM cluster.

- Hmx7/Hmx8: H-matrix represents lateral and longitudinal shower shapes of EM cluster, it is the χ^2 of the covariance matrix built for CC (EC) with 7 (8) input variables [34].

- Sigphi: shower width of the EM cluster at the third layer of the EM calorimeter in the $r - \phi$ plane.

- NN7/NN7: neural Networks trained with 7 (4) input variables for electrons in CC (photons in EC) [35].

- TrkMatch: track match probability calculated from the χ^2 distribution of the spatial separation between the EM cluster and the track found within a window of $\Delta\eta \times \Delta\phi = 0.05 \times 0.05$.

- HoR: Hits-on-Road discriminant [36].

- Lhood8: likelihood using 8 input variables [37].

- E/p: EM cluster energy divided by the matched track momentum.

4.6 $\not\!\!E_{\mathrm{T}}$

Particles that do not interact with the detector (such as neutrinos) do not leave any direct information in the detector. However, this information can be accessed indirectly via the missing transverse energy. Since Tevatron is a hadron collider, and only partons from proton and antiproton participate in the collision, the conservation of energy and momentum can be exploited only in the transverse plane. In the beam direction conservation of energy and momenta cannot be exploited as the interacting partons sample their energy from the incoming hadron based on the parton distribution function. The missing transverse energy vector is calculated as the negative vector sum of the transverse energy contents of all calorimeter cells with

an energy content of at least 100 MeV over the individual cells threshold. If muons are reconstructed in the event, their contribution is added to the visible energy in the calorimeter. A detailed description of the missing transverse energy calculation can be found in [39].

CHAPTER V

Offline Event Selection

The $ZH \rightarrow \ell^+\ell^- b\bar{b}$ analysis is performed in four independent channels defined by the sub-detectors used for lepton identification: the di-muon channel ($\mu\mu$), the muon + isolated track channel ($\mu\mu_{\rm TRK}$), the di-electron channel (ee), and the electron + ICR electron channel ($ee_{\rm ICR}$). The $\mu\mu_{\rm TRK}$ channel is designed to recover di-muon events in which one muon is not identified in the muon system (primarily because of gaps in the muon system coverage), but detected by the inner tracker. Similarly, the $ee_{\rm ICR}$ channel is recovering the di-electron events with one isolated track pointing toward one of the ICRs. This thesis only focuses on the di-muon channel, a brief description of other channels ($\mu\mu_{\rm TRK}$, ee and $ee_{\rm ICR}$) are presented in Appendix. B.

The $ZH \rightarrow \mu^+\mu^- b\bar{b}$ preselection requires a reconstructed Z candidate decaying into $\mu^+\mu^-$ plus at least two additional jets. The preselection is kept as loose as possible while maintaining good data-to-MC agreement in the control sample dominated by SM backgrounds. A multivariate technique is later used to further separate the signal from backgrounds.

5.1 Primary Vertex

A primary vertex (PV) is required with at least three associated tracks ($p_{\rm T}$>0.4 GeV and $\geq$2 SMT hits) and reconstructed z-position within 60 cm of the center of

the detector.

5.2 $Z \to \mu\mu$

Events are required to have at least two muons as defined in [52], and satisfying the following criteria:

- At least one muon have $p_{\mathrm{T}} > 15$ GeV and $|\eta_{\mathrm{det}}| < 1.5$;
- At least another muon have $p_{\mathrm{T}} > 10$ GeV and $|\eta_{\mathrm{det}}| < 2.0$;
- Muon ID requirement : `LooseNCV`;
- A matched central track satisfying the `trackloose` criteria;
- Δz (PV, μ) < 1 cm, where Δz (PV, μ) is the distance along the z-axis between the primary vertex and the muon track.

To remove muons coming from heavy flavor quarks, the following isolation requirements are applied in addition:

- At least one muon must satisfy $\Delta R(\mu, \mathrm{jet})>0.5$ with any jet has $p_{\mathrm{T}} > 20$ GeV and $|\eta_{det}| < 2.5$;
- If both muons satisfy the ΔR criterion, the leading p_{T} muon must satisfy the `scaledLoose` isolation requirement;
- If only one muon satisfies the ΔR criterion, that muon must satisfy the `scaledLoose` isolation requirement.

A good Z candidate is required in each event, reconstructed from a pair of selected muons:

- $70 < M_{\mu\mu} < 110$ GeV;

- pseudo-acolinearity > 0.05 (anti-cosmic);
- opposite electric charge;

The pseudo-acolinearity between two muons is calculated as $|\pi - \Delta(\phi_1, \phi_2)| + |(\pi - (\theta_1 + \theta_2))|$. By construction, this value is very small for cosmic muons.

5.3 Jets

At least two JCCB jets are required in each event, satisfying the following requirements:

- $p_{\mathrm{T}} > 20$ GeV;
- $|\eta_{\mathrm{det}}| < 2.5$;
- vertex confirmed (this requirement is not applied for Run 2A) and taggable.

In order to suppress additional jets originating from minimum-bias interactions, jets are required to originate from the primary vertex. The vertex confirmation requires that at least two tracks associated with the jet are matched to the primary vertex.

Because not both of the two muons have explicit cut on $\Delta R(\mu, j)$, there is a possibility that one of the muons from the $Z \to \mu\mu$ candidate is within the radius of a jet. In this analysis, all Z-candidate muons are excluded from JES muon corrections. The missing E_{T} is recomputed using the JES corrected jets and any muons not included in a jet.

5.4 b-Tagging

In order to further separate $H \to b\bar{b}$ decays from light jet backgrounds, jets are required to be tagged as b-jets using the MVA BL b-tagging algorithm developed by

the B-ID group. The b-tagging algorithm can be applied at multiple operating points with different b-tagging efficiency and light jet fake rate, by cutting on a pre-defined MVA output variable (see Section 4.4). Events with a b-tagged jet at the `MegaTight` operating point or higher and at least one additional b-tagged jet at the `L3` operating point or higher compose the double-tag (DT) sample. For the DT sample, if there are more than two b-tagged jets in a event, the di-jet system is formed by the two highest-p_{T} tagged jets. Events which do not satisfy the DT requirements, but do contain one jet b-tagged at the `MegaTight` operating point or higher, compose the single-tag (ST) sample. For the ST sample, the di-jet system of a event is formed by the tagged jet and the highest-p_{T} one of untagged jets. The usage of both DT and ST samples increases the signal acceptance and efficiency and improves the final search sensitivity. These b-tagging operating points are optimal for this analysis [56].

5.5 The naming convention of control samples

This analysis uses background-dominated control samples to assess the reliability of the background model. Generally, the control samples are selected with a looser requirement on the di-lepton mass ($40 < M_{\ell\ell} < 200$ GeV) and different jet requirements. Specifically, control samples are defined as following:

- *inclusive* : all di-lepton and primary vertex requirements are applied, except the looser di-lepton mass cut is used and all jet requirements are dropped;
- $0jet$: a subset of the *inclusive* sample consisting of events with exact 0 jet;
- $1jet$: a subset of the *inclusive* sample consisting of events with exact 1 jet;
- $2jet$-*multijet* : di-jet requirements (two or more jets) are applied but with looser di-lepton mass cut;

- $2jet\text{-}pretag$: all signal event selection requirements are applied but no b-tagging requirements applied;

CHAPTER VI

Background Modeling

In this analysis, the signal processes include $ZH \rightarrow \ell^+\ell^- b\bar{b}$, $\ell^+\ell^- c\bar{c}$ and $\ell^+\ell^-\tau^+\tau^-$. The dominant background process for the ZH search is the production of a Z/γ^* boson in association with jets (Z/γ^*+jets), with the Z boson decaying to two leptons. The remaining backgrounds come from $t\bar{t}$, diboson(WW, WZ, ZZ) and multijet production with non-prompt leptons, or with jets misidentified as leptons. With the exception of the multijet background, all contributions from other backgrounds and signal processes are estimated using the Monte Carlo (MC) simulation. However, MC simulation could not perfectly model data performances. Several reweightings (see Sect. 6.4) are applied to MC events to get the correct shape distribution of important variables. The overall normalization and the estimation of multijet background are described in Sect. 6.5.

6.1 Data Sample

The data sample used for this analysis was collected by the DØ detector from April 2002 to February 2006 (Run 2A) and from June 2006 to September 2011 (Run 2B). Run 2A data sample corresponds to an integrated luminosity of 1.1 fb^{-1}, covering runs from 151817 - 215670. Run 2B is further sub-divided into four periods according to time-dependent effects in the performance of the detector. We refer to them as

Run 2B1 (covering runs 221698 - 234913, corresponding to an integrated luminosity of 1.2 fb^{-1}), Run 2B2 (runs 237342 - 252918, 3.0 fb^{-1}), Run 2B3 (runs 255329 - 262856, 2.0 fb^{-1}) and Run 2B4 (runs 264071 - 275727, 2.4 fb^{-1}). For $\mu\mu$ channels, no explicit trigger is required, the measured trigger efficiency is consistent with 100% within 1%. After imposing data quality requirements, the integrated luminosity recorded by these triggers is 9.7 fb^{-1}.

The Common Samples Group skims used are shown in Tab. 6.1. The $\mu\mu$ events are selected from `2MUhighpt` skim, which is comprised of three logical skims: `SKIM_2MU1TRK` (at least two `Loose` muons, and at least one of which has $p_T > 15$ GeV), `SKIM_2MUhighpt` (at least two `Loose` muons with $p_T > 10$ GeV), and `SKIM_MU2TRKhighpt` (at least one `Medium` muon with $p_T > 15$ GeV, and at least two other tracks with $p_T > 15$ GeV).

Table 6.1: Common Samples Group Skims

Run 2A
CSG_CAF_<SKIM>_PASS3_p18.14.00
Run 2B1
CSG_CAF_<SKIM>_PASS2_p21.10.00
Run 2B2
CSG_CAF_<SKIM>_PASS4_p21.10.00_p20.12.00
CSG_CAF_<SKIM>_PASS4_p21.10.00_p20.12.01
CSG_CAF_<SKIM>_PASS4_p21.10.00_p20.12.02
CSG_CAF_<SKIM>_PASS4_p21.10.00_p20.12.04
CSG_CAF_<SKIM>_PASS4_p21.12.00_p20.12.05_allfix
Run 2B3
CSG_CAF_<SKIM>_PASS5_p21.18.00_p20.16.07_fix
CSG_CAF_<SKIM>_PASS5_p21.18.00_p20.16.07_reduced2
CSG_CAF_<SKIM>_PASS5_p21.18.00_p20.16.08
Run 2B4
CSG_CAF_<SKIM>_PASS6_p21.20.00_p20.18.02b
CSG_CAF_<SKIM>_PASS6_p21.20.00_p20.18.02b_fix
CSG_CAF_<SKIM>_PASS6_p21.21.00_p20.18.03
CSG_CAF_<SKIM>_PASS6_p21.22.00_p20.18.04
CSG_CAF_<SKIM>_PASS6_p21.22.00_p20.18.05

6.2 Multijet Sample

The Tevatron's $p\bar{p}$ collisions produce an enormous number of multijet events, some of them will be reconstructed as $ZH \to \ell^+\ell^- b\bar{b}$ events where jets are misidentified as leptons. This instrumental multijet background is not well modeled by the MC simulation, and thus has to be estimated from control samples in the data. The conventional approach is to reverse the cuts used to reject multijet background. In the $\mu\mu$ channel, a multijet event must contain a Z candidate which passes all event selection criteria, expect the two muons must fail the opposite-sign charge requirement, and events with both muon failing the $\Delta R(\mu, \text{jet})>0.5$ cut are also allowed. The event weight of the multijet sample will be scaled, so that together with the MC simulation, the total background estimation could match the data sample. The produces of determining those scale factors are described in Section 6.5.

6.3 Monte Carlo Samples

The MC samples used for this analysis are listed in Tab. 6.2. The ZH and diboson processes are simulated using `Pythia` [61], while the $t\bar{t}$ and Z/γ^*+jets processes are simulated with `Alpgen` [62]. The Z/γ^*+jets MC samples are generated separately for different number of additional partons. The events generated with `Alpgen` use `Pythia` for parton showering and hadronization. Because this procedure can generate additional jets, the `MLM` matching scheme [63] is adopted to avoid double counting of partons produced by `Alpgen` and those subsequently added by the parton showing in `Pythia`. The Z/γ^*+nlp samples only consist of Z/γ^* plus light flavor jets events (Z/γ^*+LF). To enhance the statistics of the events with heavy flavor jets, Z/γ^*+HF samples are generated specifically for $Z/\gamma^*+2b+nlp$ and $Z/\gamma^*+2c+nlp$. To avoid double counting, events with b or c quarks are removed from the Z/γ^*+nlp samples, and c quarks from the $Z/\gamma^*+2b+nlp$ samples [64].

Table 6.2: Run 2B CAF MC samples.

Sample	MC Dataset
$Z/\gamma^* \rightarrow mumu$	CSG_alpgenpythia_gamz+Nlp_mumu+Nlp_excl_RANGE_RELEASE_VERSION
	CSG_alpgenpythia_gamz+3lp_mumu+3lp_incl_RANGE_RELEASE_VERSION
Z/γ^*+bb	CSG_alpgenpythia_gamz+2b+Nlp_mumu+2b+Nlp_excl_RANGE_RELEASE_VERSION
	CSG_alpgenpythia_gamz+2b+2lp_mumu+2b+2lp_incl_RANGE_RELEASE_VERSION
Z/γ^*+cc	CSG_alpgenpythia_gamz+2c+Nlp_mumu+2c+Nlp_excl_RANGE_RELEASE_VERSION
	CSG_alpgenpythia_gamz+2c+2lp_mumu+2c+2lp_incl_RANGE_RELEASE_VERSION
$Z/\gamma^* \rightarrow \tau\tau$	(replace mumu by tautau above)
WZ	CSG_pythia_w+z_incl_RELEASE_VERSION
ZZ	CSG_pythia_z+z_incl_RELEASE_VERSION
WW	CSG_pythia_w+w_incl_RELEASE_VERSION
$t\bar{t}$	CSG_alpgenpythia_t+t+0lp_2l+2nu+2b_excl_m172_RELEASE_VERSION
	CSG_alpgenpythia_t+t+1lp_2l+2nu+2b+1lp_excl_m172_RELEASE_VERSION
	CSG_alpgenpythia_t+t+2lp_2l+2nu+2b+2lp_incl_m172_RELEASE_VERSION
	CSG_alpgenpythia_t+t+0lp_lnu+2b+2lpc_excl_m172_RELEASE_VERSION
	CSG_alpgenpythia_t+t+1lp_lnu+2b+3lpc_excl_m172_RELEASE_VERSION
	CSG_alpgenpythia_t+t+2lp_lnu+2b+4lpc_incl_m172_RELEASE_VERSION
$ZH(H \rightarrow bb)$	CSG_pythia_zh_2l+2b_mhMASS_RELEASE_VERSION
$ZH(H \rightarrow cc)$	CSG_pythia_hl+z_2c+2l_mhMASS_RELEASE_VERSION
$ZH(H \rightarrow \tau\tau)$	CSG_pythia_hl+z_2tau+2l_mhMASS_RELEASE_VERSION

Sample cross-sections were taken from several different sources. The NNLO $t\bar{t}$ cross section of 7.04 pb is taken from a calculation by Langenfeld, Moch and Uwer [85]. The NLO cross sections for the diboson processes are taken from MCFM [84]. Cross sections for the ZH samples are taken from [86]. The Z/γ^*+jets cross section is scaled to NNLO and additional NLO heavy-flavor scale factors are applied to Z/γ^*+HF samples (see Section 6.4.7).

All simulated samples are generated using the CTEQ6L1 [65] leading order parton distribution functions (PDF). To simulate the underlying event, consisting of all particles not originating from the hard scattering, a so-called DØ Tune A is used [66]; The generated MC samples were processed with the standard DØsimulation chain which includes a full GEANT 3 detector simulation. Zero-bias events (total inclusive trigger) taken from data are overlaid onto the MC events to model the effects of multiple $p\overline{p}$ interactions and detector noise. Finally, events were reconstructed using the DØ data reconstruction algorithms.

In Tab. 6.2, the `RANGE` stands for the dilepton invariant mass, which takes values 15_75, 75_130, 130_250, and 250_1960 in implicit units of GeV. The `N` indicates the number of additional light partons; it runs from 0 to 2 for Z/γ^*+LF MC samples, and runs from 0 to 1 for Z/γ^*+HF samples. The `RELEASE_VERSION` of four separate MC sets are : `p181400_v12` for Run 2A MC, `p211100_v13` for Run 2B1 MC, `p211800_v6` for Run 2B2 MC and `p212100_v4` for Run 2B3 MC. For the ZH samples, the Higgs mass is specified by the string `MASS`, which takes values 90, 95, ... 150 GeV.

6.4 Corrections to Monte Carlo

The MC samples are corrected to account for the detector effects that are not adequately modeled by the simulation. Some of the corrections are integrated with the DØ analysis framework (`vjets_cafe`), including luminosity reweighting, primary-vertex reweighting, lepton energy/ID efficiency correction, jet energy scaling and smearing, jet vertex confirmation/taggability/b-tagging scale factors, k-factors on the cross sections, Z-p_{T} and VH p_{T} reweighting. Other corrections are derived and applied within the ZH analysis, including trigger efficiency correction, lepton/jet angle reweighting and some speical corrections to parameters related to the `Alpgen` generator. All these corrections are described below.

6.4.1 Luminosity Reweighting

The performance of the detector is usually highly related to the instantaneous luminosity, in order to provide a realistic simulation of the detector response to beam conditions, an actual data event collected using zero-bias triggers is used to define the baseline detector response for each MC event. However, the instantaneous luminosity for the zero-bias overlay does not match the luminosity profile of the data sample, so the event weight of each MC events is scaled to match the measured luminosity profile from data. See Fig. 6.1.

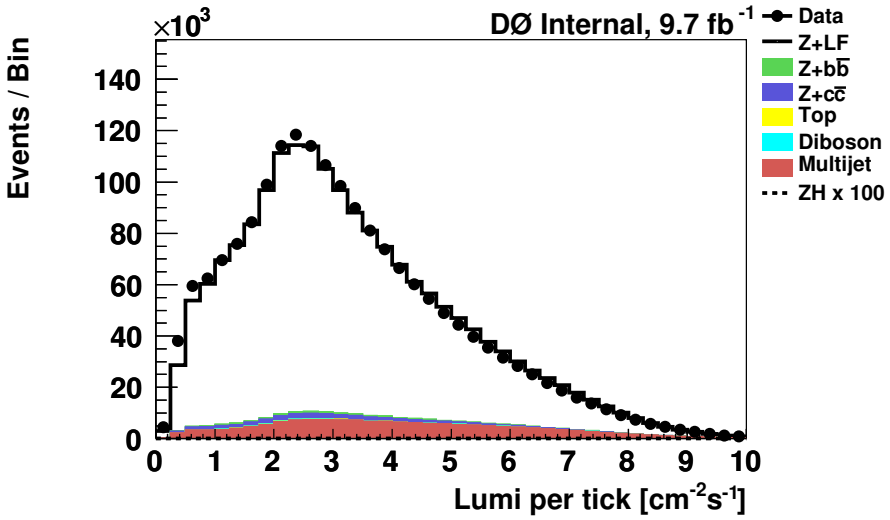

Figure 6.1: The instantaneous luminosity distributions of data and MC samples with all lepton channels combined, after lepton selection but before any jet requirements. The MC distribution has been reweighted.

6.4.2 Primary-Vertex Reweighting

The z profile of the primary collision during a store changes shape due to the growth of the emittance of the colliding beams, becoming broader later in the store. In the MC generation, a Gaussian distribution with a fixed width of 25 cm is used for the primary vertex distribution. To provide a more realistic model, the MC primary vertex z-position of MC events is reweighted to match the measured distribution from data (See Fig. 6.2).

6.4.3 Lepton ID Efficiency Corrections

For the MC leptons, scale factors are applied to take into account the difference in lepton identification efficiency between data and MC. For MC electrons, they are applied in two steps [67]. The correction factors for the preselection are applied as a function of ϕ_{mod} in CC and detector η in EC first. Then the correction factors for the electron selection efficiency are applied as a function of instantaneous luminosity, detector η and p_{T}. For MC muons, two corrections are applied : one for the mis-modeling in the muon identification efficiency, and the other for the efficiency of

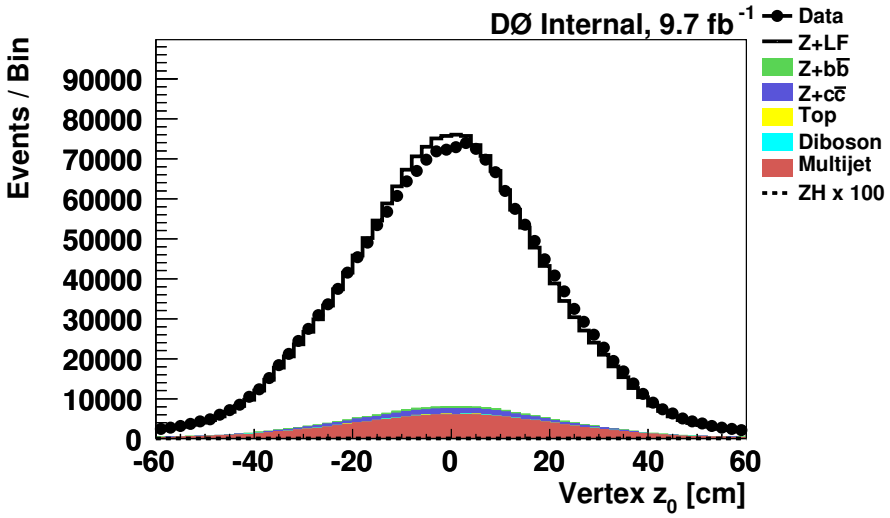

Figure 6.2: The primary vertex z distribution of data and MC samples for all lepton channels combined, after lepton selection but before any jet requirements. The MC distribution has been reweighted.

reconstructing the matched track based upon the loose track requirements.

6.4.4 Lepton Energy Corrections

The energy resolution of the EM shower in the MC events generated by the DØ simulation system is slightly better than observed in the data. Additionally, the EM resolution is improved by applying a calibration based on the H-Matrix value and ϕ_{mod} of the EM shower [68]. This calibration is processed to correct electron energies in both data and MC. Subsequently, the energies of MC electrons have to be smeared to agree with data. The p_{T} of MC muons and isolated tracks is also smeared similarly.

6.4.5 Jet Shifting Smearing and Removal

To account for differences in efficiency between data and MC, all MC jets are corrected by the Jet Shifting, Smearing, and Removal (JSSR) processor [69]. A flavor-dependent JSSR is used for quarks and gluon jets accordingly. The smearing parameters are obtained by fitting the p_{T} imbalance of the $Z \rightarrow ee$ plus single jet events for both data and MC. The derived corrections for jets in the very forward EC

$(2.4 < |\eta_{det}| < 3.2)$ are statistically limited in accuracy. The corrections derived for $1.6 < |\eta_{det}| < 2.4$ region are applied for the very forward EC region.

6.4.6 Corrections to the `Alpgen` parameters

Possible corrections to the `Alpgen` parameters used in the simulation, such as renormalization (factorization) scale, $k_\perp$-factor used to determine the scale of α_s at each vertex, parton matching cluster p_{T} threshold and cluster radius, have been studied [75]. Only the correction for the p_{T} threshold is applied, but the remaining effects are treated as systematic uncertainties.

6.4.7 Z/γ^*+jets Cross Section

MC event generators often use only LO calculations when producing events. To predict the total number of events at higher order, the event weights are scaled by a k-factor which is the ratio of the LO cross-section to the highest order calculation that is available: typically NLO or NNLO.

The inclusive Z/γ^* cross sections determined by `Alpgen` are Leading-Log (LL) calculations and have been scaled to the NNLO inclusive Z/γ^* calculations [71]. As this scale factor is not a typical NNLO/LO k-factor, it is referred to as a k'-factor, and has been found to be 1.30. This factor is then used to scale all of the `Alpgen` Z/γ^* plus light jets samples and an error of 6% is quoted due to variations of factorization scale, PDFs, and generator cuts.

The scale factor for the heavy flavor process is achieved in the following way. Using `MCFM` [84], k-factors (NLO/LO) are determined for Z/γ^*+$b\bar{b}$, Z/γ^*+$c\bar{c}$, and Z/γ^*+LP processes. The heavy-flavor scale factor is determined by dividing the k_{HF} by the k_{LF}. The `Alpgen` Z/γ^*+HF cross sections are scaled by this additional factor

given by [72]:

$$k' \times HF_{b\bar{b}} = 1.30 \times 1.52 = 1.96, \quad (6.1)$$

$$k' \times HF_{c\bar{c}} = 1.30 \times 1.67 = 2.15. \quad (6.2)$$

6.4.8 Cross Sections for Other Processes

The diboson and $t\bar{t}$ cross-sections are corrected by similar k-factors, which are calculated as the ratio of the NLO (`MCFM` [84]) cross sections to the LO (`Pythia` and `Alpgen`) cross sections using CTEQ6.1M PDFs. The resulting k-factors:

$$k(ZZ) = 1.030, \quad (6.3)$$

$$k(WZ) = 1.062, \quad (6.4)$$

$$k(WW) = 1.005, \quad (6.5)$$

$$k(t\bar{t}) = 1.06. \quad (6.6)$$

6.4.9 Z-p_{T} Reweighting

The Z boson p_{T} distribution is poorly modeled by both the `Pythia` and `Alpgen` MC generators, especially for events with small p_{T}. The discrepancy is corrected in MC by reweighting the Z-p_{T} distribution to match what we observed in the data. The correction is derived from the p_{T} distribution at the generator level and the observed spectrum in the unfolded data [73].

After the reweighting, improved agreement between data and MC is observed for the Z boson p_{T} distribution in all leptonic samples. as shown in Fig. 6.3.

6.4.10 VH p_{T} Reweighting

We correct the generator level p_{T} of the ZH system, p_{T}^{ZH}, in the signal samples to match the predicted distribution from `Resbos` [76], according to the prescription

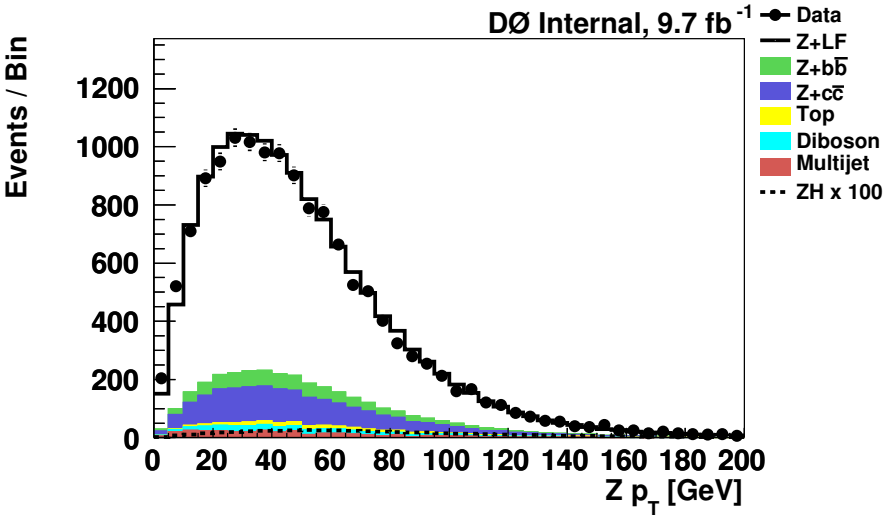

Figure 6.3: The Z-boson p_{T} distribution, requiring at least two jets.

in Ref. [77]. In Fig. 6.4, we compare the distribution of p_{T}^{ZH} obtained from the DØ `Pythia` samples (before ant after the reweighting is applied) used for this analysis (for M_H=115 GeV) to that obtained from `Resbos`.

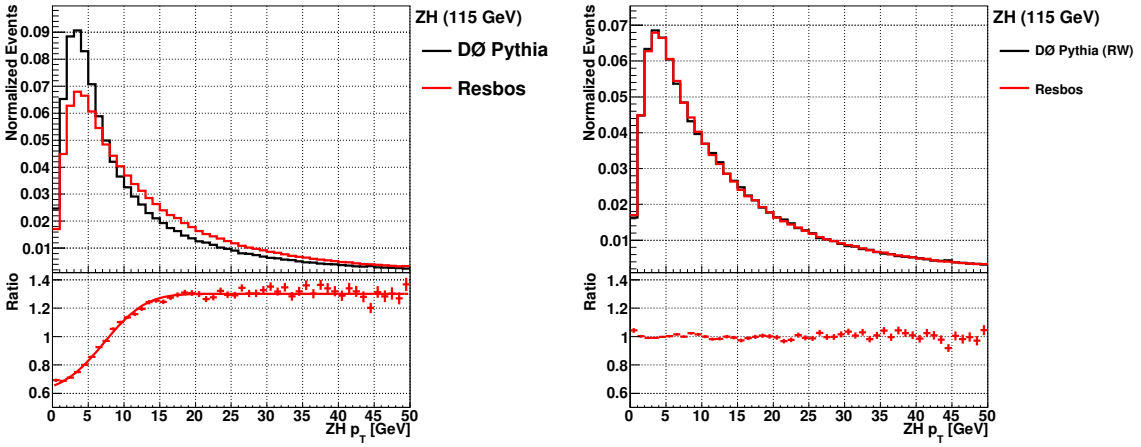

Figure 6.4: Comparison of the p_{T}^{ZH} distributions in `Resbos` and `Pythia` for M_H=115 GeV [77]. On the left, no correction is applied to the `Pythia` sample. On the right, the `Pythia` sample has been reweighted to match the `Resbos` sample. The ratios of the `Resbos` to the `Pythia` samples are also shown. The ratio of the uncorrected `Pythia` sample to the `Resbos` sample is fit to an error function.

6.4.11 Vertex Confirmation/Jet Taggability Scale Factors

In the event selection criteria of Run 2B epochs, a jet is required to be vertex-confirmed and taggable. The difference in the efficiencies for this selection between data and MC events are corrected with scale factors, which are the ratio of the efficiencies for data and MC samples, provided by the Jet ID group based on studies di-jet samples. The efficiencies are parametrized as a function of jet p_{T}, η, and the z-coordinate of the primary vertex. Vertex confirmation was not applied for the Run 2A samples so no correction factors were applied.

It has been found that the official vertex confirmation/taggability scale factors from the Jet ID group do not fit for ZH analysis quite well. Taking the jet $p_T = 30$ GeV case in $0 < Z_{vertex} < 20$ cm region as an example, the efficiency and scale factors provided by the Jet ID group are shown in the top two plots of Fig. 6.5, and the middle two plots show the efficiency and scale factors measured from ZH analysis using the Z/γ^*+1jet sample of the $\mu\mu$ Run 2B34 epoch. The features in these two sets of measurement could be summarized as the following :

- The efficiencies for the vertex confirmation and taggability requirements from the Jet ID group are $\sim 90\%$ for both data and MC.
- The scale factors for the vertex confirmation and taggability are close to 1, except at low p_T where the scale factor dips down by $\sim 10\%$ at $|\eta| < 0.5$.
- The efficiencies for the vertex confirmation and taggability requirements from our measurement are $\sim 75\%$ for both data and MC.
- The scale factors for the vertex confirmation and taggability from our measurement are close to 1, and largely flat in η without a dip at $|\eta| < 0.5$.

Possible source of this difference are investigated. The procedure by the Jet ID group is described in D0note 6058. In order to remove the contamination from min-

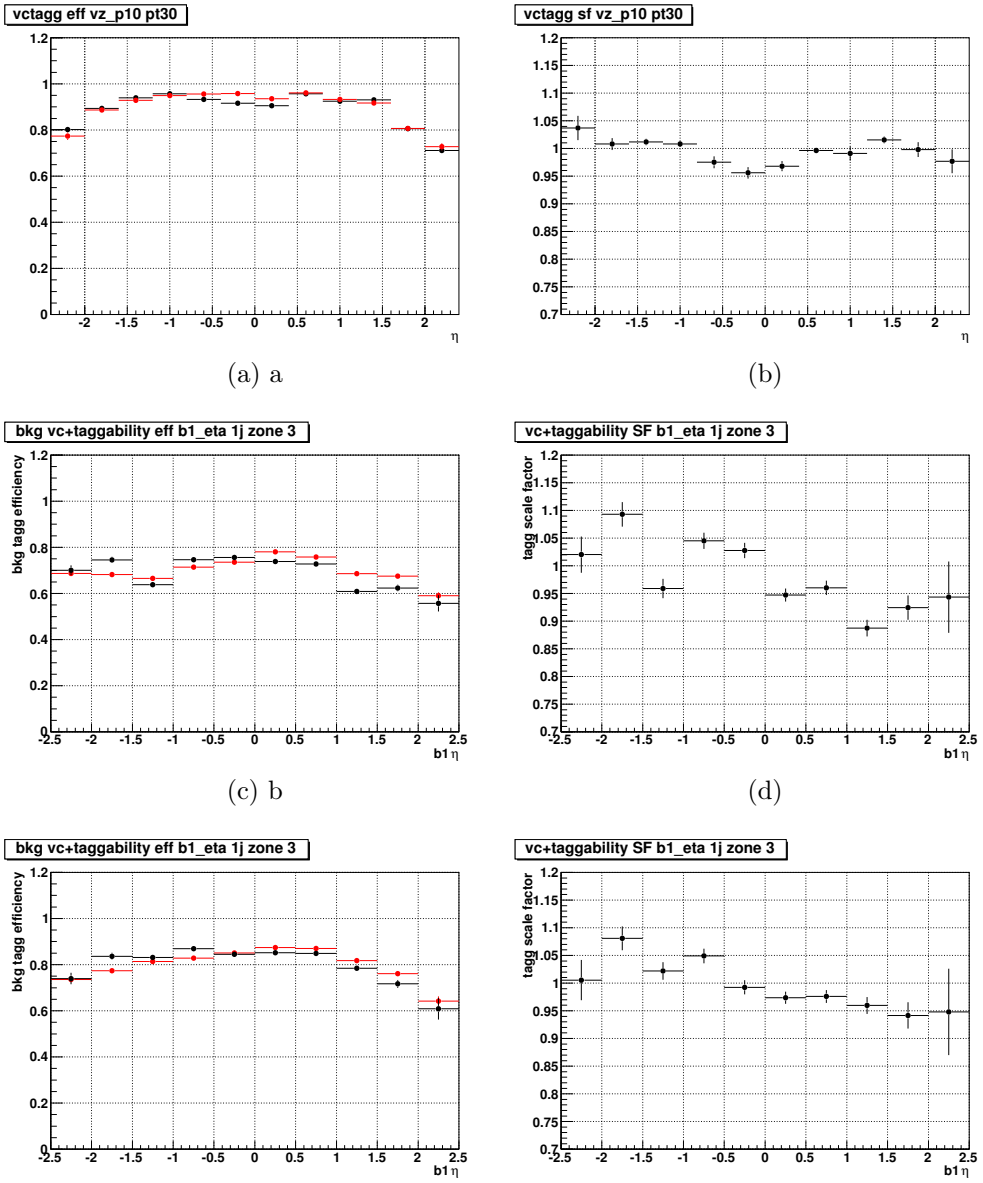

(a) a (b)

(c) b (d)

(e) c (f)

Figure 6.5: The efficiencies (left) and scale factors (right) of the vertex confirmation and taggability requirements for $p_T = 30$ GeV in primary veertex region $0 < Z_{vertex} < 20$ cm (a) provided by the Jet ID group, (b) measured from ZH analysis, (c) measured from the Z/γ^*+1jet sample in ZH analysis, with requirements of $\delta\phi(Z, jet) > 3$ and $Asym_{p_t} < 0.3$ applied. The black and red circles are data and MC, respectively.

imum bias jets, two requirements are imposed on the tag and probe jets: (1) two jets be back-to-back in ϕ direction ($\Delta\phi_(j, j) > 3$) and (2) the p_T asymmetry between two jets be small ($|p_T^{j1} - p_T^{j2}|/(p_T^{j1} + p_T^{j2}) < 0.3$). In Fig. 6.6, similar distributions(Z

boson is used as the "tag" jet) are shown in our samples using Z/γ^*+1jet events. The requirement of the small p_T asymmetry seems to select the vertex confirmed and taggable jets preferentially. This is likely the source of difference between the efficiencies.

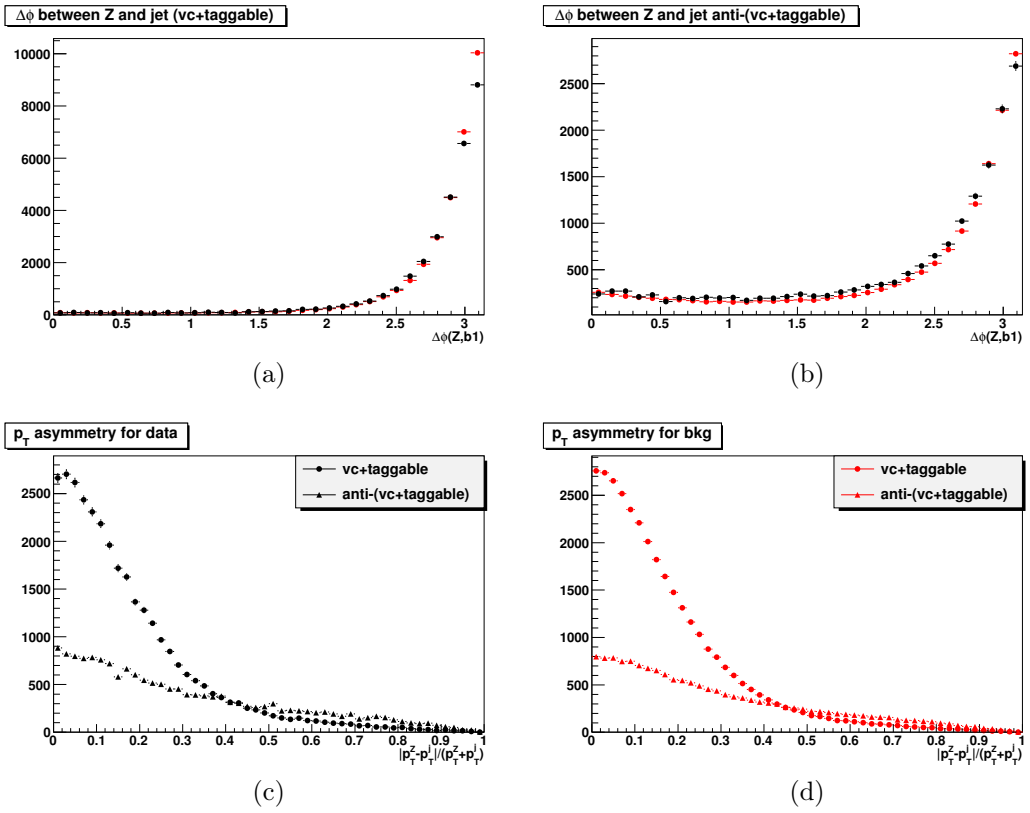

Figure 6.6: (a) $\Delta\phi$ between Z and a jet in $Z+1$ jet events where the jet is vertex confirmed and taggable (red and black points are data and MC, respectively), (b) $\Delta\phi$ between Z and a jet in $Z+1$ jet events where the jet fails the vertex confirmation or taggability (red and black points are data and MC, respectively), (c) p_T asymmetry for data (black circles and triangles are jets that passes the vertex confirmation and taggability, and jets that fails at least one of the requirements) and (d) p_T asymmetry for MC (red circles and triangles are jets that passes the vertex confirmation and taggability, and jets that fails at least one of the requirements).

Then the same back-to-back and small p_T asymmetry requirements are applied on the Run 2B34 Z/γ^*+1jet sample, except that we use the Z in the event as a tag. The results are shown in the bottom two plots of Figs.6.5. As can be seen, the efficiencies improve by $\sim$ 10% in both the vertex confirmation efficiencies and

the vertex confirmation and taggability efficiencies. On the other hand, applying the minimum bias jet rejection changes the scale factors by only a small amount.

Based on these observations, the official scale factors for the vertex confirmation and taggability requirements from the Jet ID group are still applied to MC samples in this analysis, but assigning 100% systematic uncertainty to cover the inconsistency between our efficiency measurement and the Jet ID group's.

6.4.12 Scale Factors for b-tagging

The Tag Rate Functions (TRFs) have been measured by the b-id group as described in [78]. The scale factors (SF_i) for jets to pass each b-tagging requirement i are calculated as the ratio of the data TRFs and the MC TRFs. Because we do not use the b-tagging discriminant in our multivariate analysis, it would be sufficient to use these scale factors to our simulated event weights. However, we instead apply pseudo-continuous scale factors which have been found to be able to improve the accuracy of our background model.

We define the pseudo-continuous scale factor SF_i^{cont} for a jet that satisfies the b-tagging requirement i, but fails the b-tagging requirement $i+1$:

$$SF_i^{cont} = \frac{N_{pretag}D_i - N_{pretag}D_{i+1}}{N_{pretag}M_i - N_{pretag}M_{i+1}} \tag{6.7}$$

where D_i is the data TRF for that jet, and M_i is the MC TRF for that jet, and N_{pretag} is the number of events prior to any b-tagging requirement. Given that $M_i = D_i/SF_i$, this reduces to:

$$SF_i^{cont} = SF_i SF_{i+1} \frac{D_i - D_{i+1}}{SF_{i+1}D_i - SF_i D_{i+1}} \tag{6.8}$$

To evaluate the uncertainty on SF_i^{cont}, we simultaneously shift SF_i and SF_{i+1} by their respective uncertainties. We assume that the uncertainty on the difference

$D_i - D_{i+1}$ is small, and therefore do not account for the uncertainty on the TRFs.

6.4.13 Trigger Corrections

Although no explicit trigger requirement is made in the $\mu\mu$ channel, it remains necessary to correct for trigger acceptance effects that are not well modeled by the MC. Trigger efficiencies do not exist for the inclusive triggering method. Therefore a correction has to be developed based on a reference sample, in which we require that the leading muon with $|\eta_{\text{det}}| < 1.5$ passed one of the triggers in the SingleMuonOR trigger suite. A SingleMuonOR trigger parameterization is applied to all MC, which is shown to agree with SingleMuonOR data in most important kinematic distributions. Various kinematic distributions between SingleMuonOR triggered data and MC for the $\mu\mu$ channel are shown in Fig. 6.7 - 6.11, taking Run 2B34 data epoch as an example.

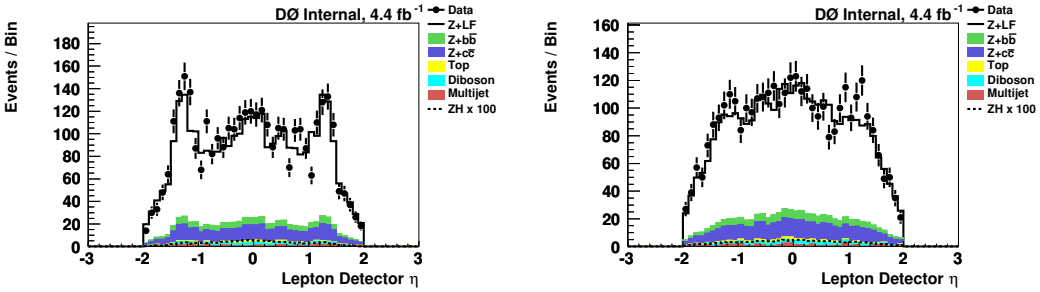

Figure 6.7: Data/MC comparison of the detector η distributions for lead μ(left) and second μ(right) for single-muon-OR-triggered Run 2b34 $\mu\mu$ in pretag control sample (including jet requirements).

The correction was derived from the ratio of inclusively-triggered data to the SingleMuonOR reference sample. A shape-only correction is derived from the zero-jet bin, parametrized in the η_{det} of the muon fired the trigger, the η_{det} of the other muon, as well as the missing transverse energy. This correction is also used for other jet multiplicity bins. Figure. 6.13 show the various components of the $\mu\mu$ trigger correction, taking Run 2B34 epoch as an example. Note that by construction, only

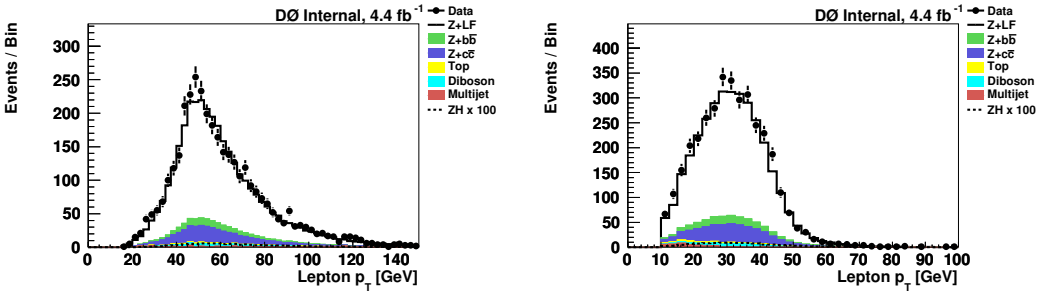

Figure 6.8: Data/MC comparison of the pt distributions for lead μ(left) and second μ(right) distributions for single-muon-OR-triggered Run 2b34 $\mu\mu$ in pretag control sample (including jet requirements).

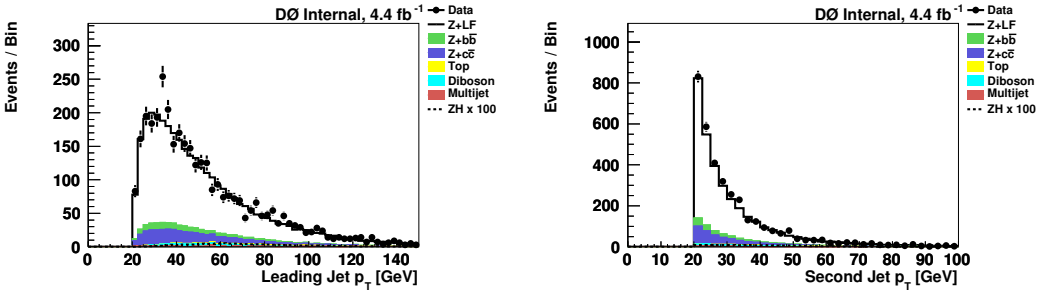

Figure 6.9: Data/MC comparison of the pt distributions for lead jet(left) and second jet(right) for single-muon-OR-triggered Run 2b34 $\mu\mu$ in pretag control sample.

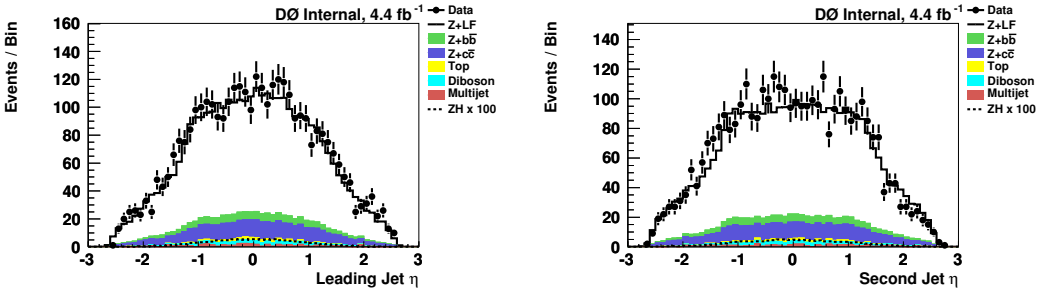

Figure 6.10: Data/MC comparison of the η distributions for lead jet(left) and second jet(right) for single-muon-OR-triggered Run 2b34 $\mu\mu$ in pretag control sample.

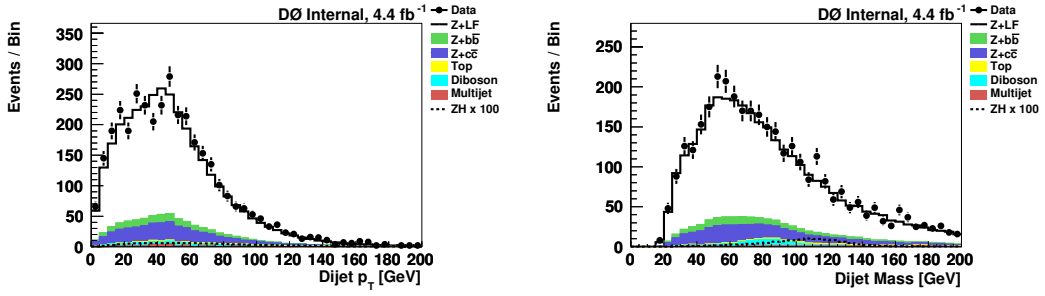

Figure 6.11: Data/MC comparison of the Dijet pt(left) and mass(right) distributions for single-muon-OR-triggered Run 2b34 $\mu\mu$ in pretag control sample.

the factor that is dependent on the jet multiplicity is allowed to change the overall normalization. To validate that usage, we have made the ratio of normalized $\not\!\!E_{\mathrm{T}}$ distribution between inclusive and single Muon triggers for each different jet bins. As shown in Fig. 6.12, the ratio is consistent in different jet bins within 1σ statistical fluctuation. This shape correction is applied to all jet multiplicity bins, but the overall scale of the correction is measured and applied separately for each bin. This scale is set by the ratio of the event yields in the inclusively triggered and reference samples.

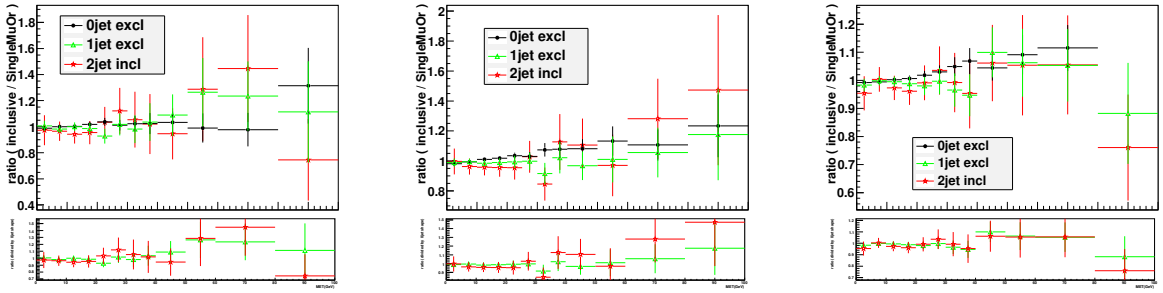

(a) (b) (c)

Figure 6.12: The ratio of normalized $\not\!\!E_{\mathrm{T}}$ distributions between inclusive and single muon triggers. The bottom part is the ratio respect to the zero-jet bin.

The correction is evaluated and applied to every MC event. Using this correction, agreement between inclusively-triggered data and background is substantially improved. The method to derive the correction, and the corresponding uncertainty is described in [79].

We note that because we use the SingleMuonOR trigger efficiency, we should, In principle, an uncertainty of the SingleMuonOR trigger efficiency should be propagated to the final results. The trigger group recommends a flat 5% uncertainty. However, any such uncertainty will be removed by the normalization procedure described in Section 6.5. Therefore, the trigger efficiency is not considered as a source of systematic uncertainties.

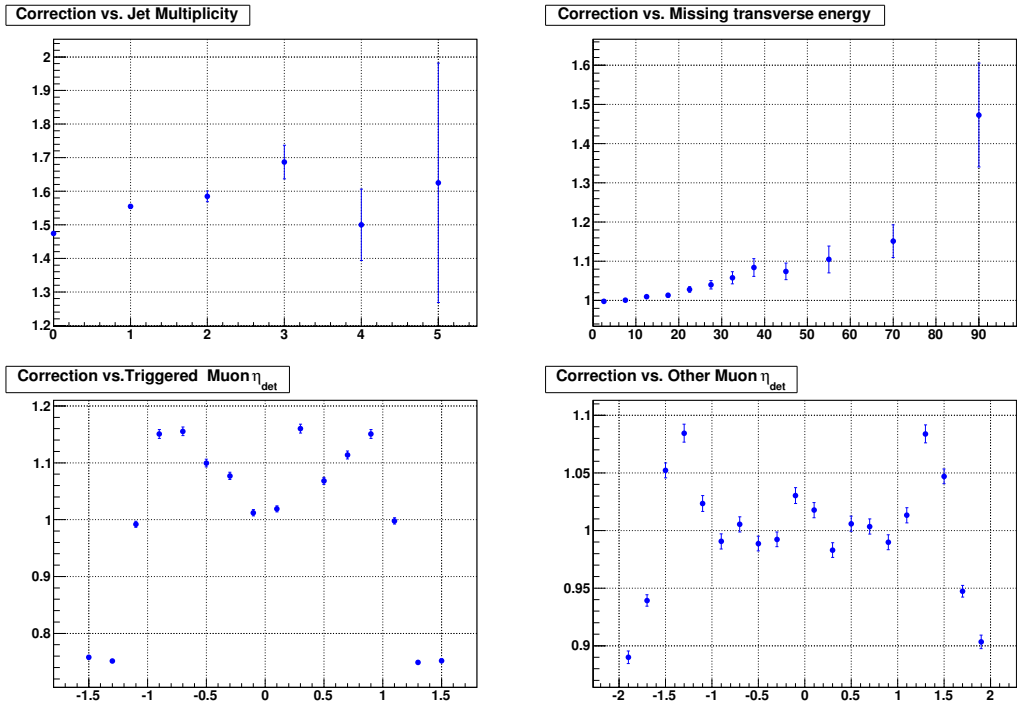

Figure 6.13: Components of the $\mu\mu$ trigger correction for Run 2b34. From left to right: dependence on jet multiplicity, missing transverse energy, triggered muon detector η and untriggered muon detector η.

6.4.14 Lepton/Jet Angle Reweighting

The W/Z+jets MC samples generated with a combination of `Alpgen` and `Pythia` do not reproduce the η distribution of decay leptons and jets accurately. Also, it is well-known that the detector response to jets in the ICR is poorly modeled. A three-step reweighting is performed to correct reconstructed jet and lepton angles for

Z/γ^*+jets samples.

(1) Reweight Z/γ^*+jets events as a function of the leading lepton η, using the function form developed for the WH analysis. This reweighting is independent of data epochs, and has been verified to work well for the ZH analysis (see Figure 6.14).

(2) After the lepton η reweighting is applied, correct the jet η distribution. The reweighting functions are derived from the pretag sample, by taking the ratio of jet η distributions between data after the subtraction of the non-Z backgrounds and the sum of Z background. The ratio is shown in Figure 6.15 along with a second-order polynomial fit using the for the data epochs of Run 2A, Run 2B12 and Run 2B34. The jets detected within the ICR ($1.0 < |\eta| < 1.6$) are discarded in this study in order to avoid bias due to the low E_T jet horn in this region.

(3) After applying the jet η reweighting described above, the correction for the jets in the ICR is performed in a way similar to step (2), except now requiring $1.0 < |\eta_{jet}| < 1.6$. The fit results for the three data epochs are shown in Figure 6.16, the an upside-down Gaussian is used as fitting functions.

6.4.15 Unclustered Energy Reweighting

The Unclustered Energy is defined as the scalar sum of energy deposited in the electromagnetic calorimeter, hadronic calorimeters as well as the ICD region, but which are not accounted for parts of a clustered object (jet, electromagnetic object or a muon). The unclustered objects are used in the calculation of $\not\!\!E_{\rm T}$, which is a quite powerful variable to distinguish the signal from backgrounds. Even after all corrections applied, MC simulation still could not model the unclustered energy quite well. Then reweighting factors are derived from a control region of $m_Z < 70$ GeV or $m_Z > 110$ GeV, by taking the ratio of the (data-qcd) sample and all MC background samples (See Fig. 6.17). This correction is derived and applied for 0jet, 1jet, $\geq$2jets events separately. The unclustered energy distribution after the correction are shown

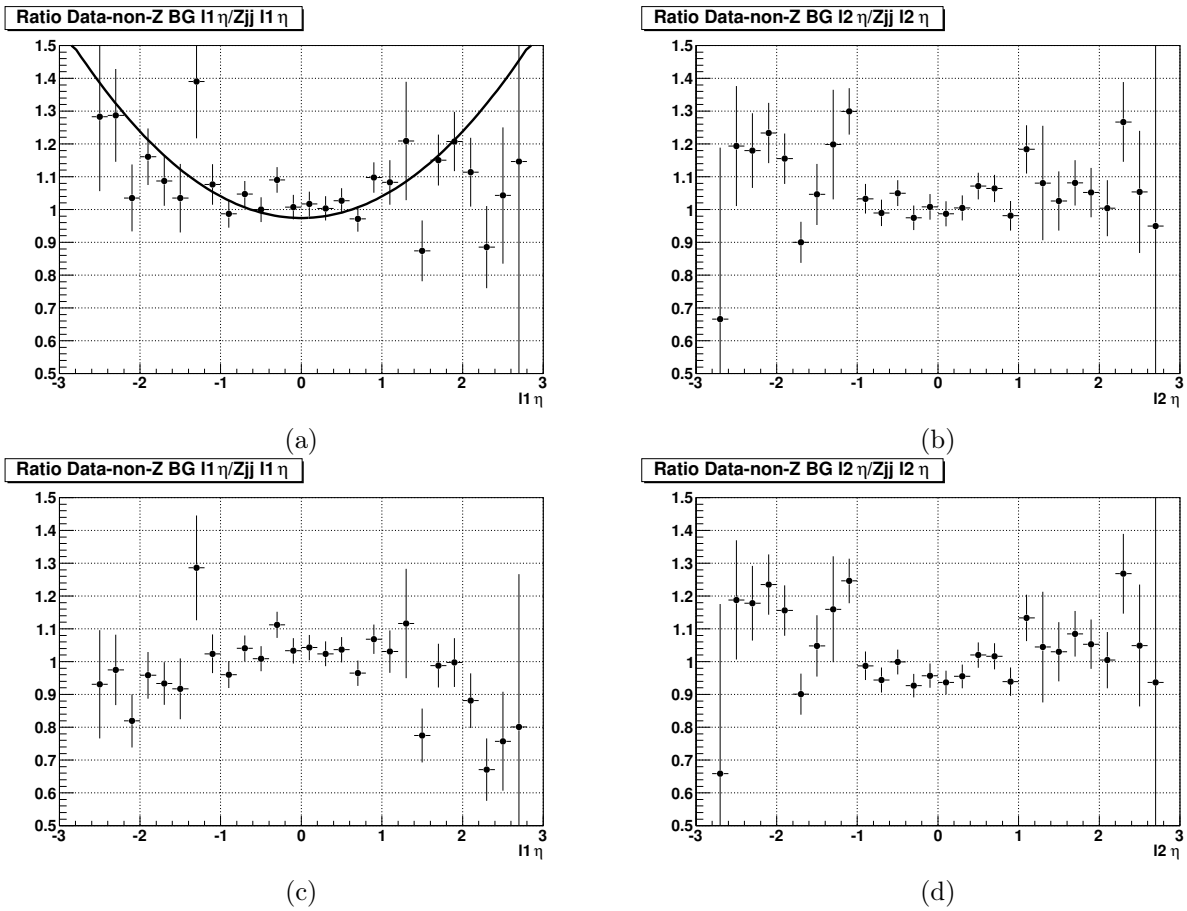

Figure 6.14: The ratio of the (data - non-Z bkg) to the Z/γ^*+jets bkg for the leading muon η (left) and the sub-leading muon η (right), before (top) and after (bottom) the correction.

in Fig. 6.18.

6.5 Background Normalization

6.5.1 Combined Normalization

With all corrections described in the Sect. 6.4, we are trying our best to make the MC simulation matching data distribution. However, even after all those corrections, the MC simulation is not perfect. And more importantly, the uncertainties on the Z/γ^*+jets cross section is large ($\sim$ 20%). In order to improve the accuracy of the background modeling, scale factors adjusting the contribution of each background are

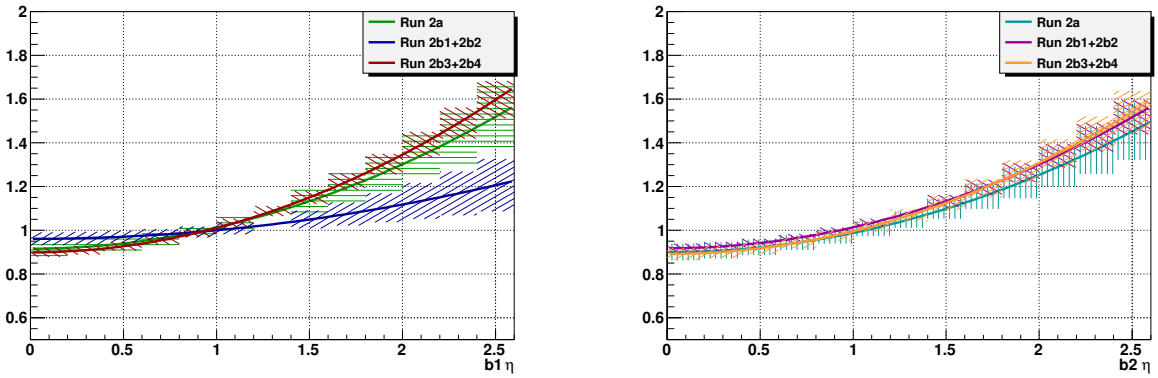

(a) (b)

Figure 6.15: The fits to the ratio of jet (not in ICR) η distributions for (a) the leading jet and (b) the sub-leading jet.

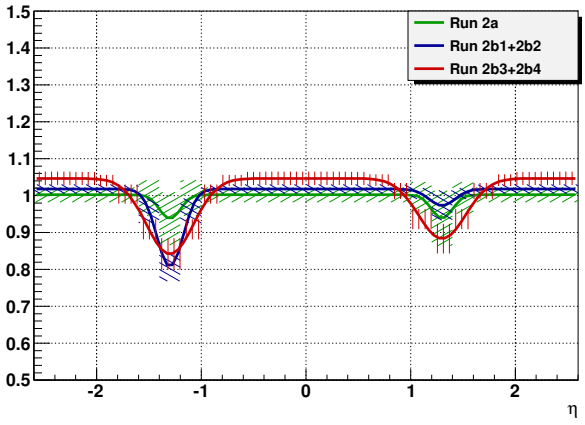

(a)

Figure 6.16: The ratio of the jet (in ICR) η distributions between data minus QCD background and the rest of the backgrounds after the jet-η reweighting (fit to upside-down Gaussian).

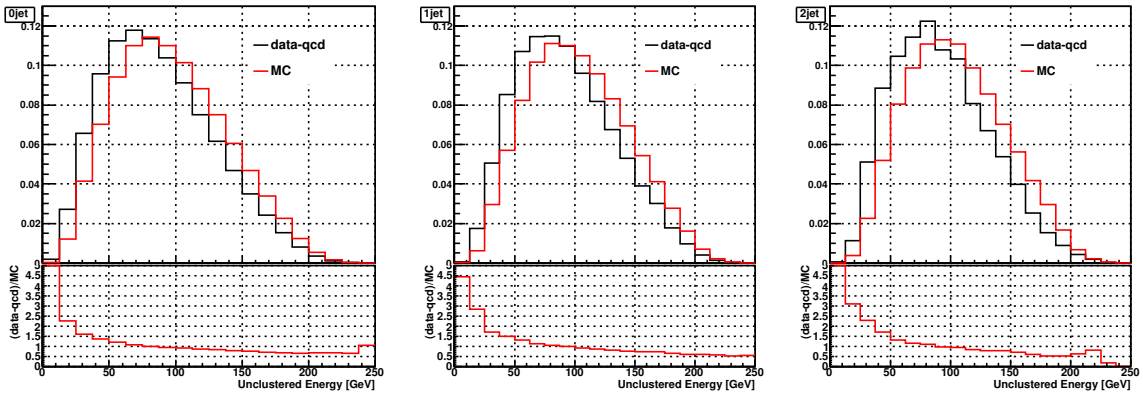

Figure 6.17: Unclustered Energy correction functions for all jet bin multiplicities from $\mu\mu$ events

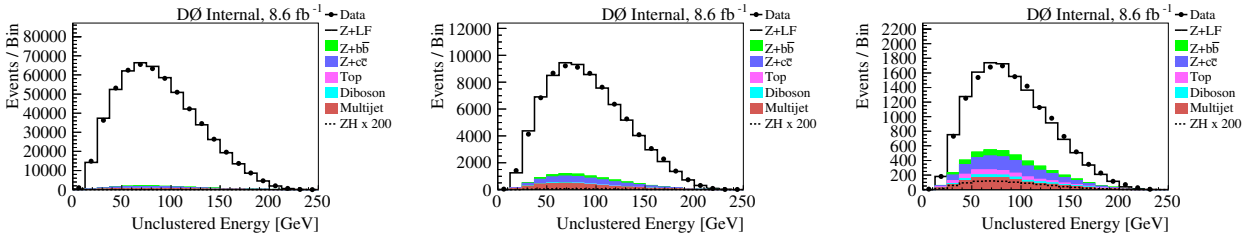

(a) (b) (c)

Figure 6.18: Unclustered Energy distribution after corrections in (1)left: 0jet bin (2)middle: 1jet bin (3)right: >2jets bin.

fit to the observed data in pre-tag control samples. The fit adjusts the normalization of shape templates in the di-lepton invariant mass from each background sample to obtain the best agreement with the pre-tag data.

By including all lepton channels and jet-multiplicity bins, a combined fit is able to disentangle and account for different types of effects. The fit is performed for Run 2A Run 2B1, Run 2B2 and Run 2B34 epochs independently, there are 20 independent channels as shown in Table 6.3:

The fit uses the following templates:

Table 6.3: List of Channels.

Run 2A	ee(CCCC)	ee(CCEC)	ee_{ICR}	$\mu\mu$	$\mu\mu_{\text{TRK}}$
Run 2B1	ee(CCCC)	ee(CCEC)	ee_{ICR}	$\mu\mu$	$\mu\mu_{\text{TRK}}$
Run 2B2	ee(CCCC)	ee(CCEC)	ee_{ICR}	$\mu\mu$	$\mu\mu_{\text{TRK}}$
Run 2B34	ee(CCCC)	ee(CCEC)	ee_{ICR}	$\mu\mu$	$\mu\mu_{\text{TRK}}$

- D_m^{ij}, the data;
- Q_m^{ij}, the multijet control sample;
- Z_m^{ij}, the simulated Z/γ^*+jets samples, including $Z/\gamma^*+b\bar{b}$ and $Z/\gamma^*+c\bar{c}$ samples;
- O_m^{ij}, all other simulated samples;

where m indexes the dilepton mass bin, $i = 1, 2, ..., 20$ which indexes channels listed in Tab. 6.3), and $j = 0, 1, 2$ which indexes the jet-multiplicity bins (0jet, 1jet and $\geq$ 2jets). The fit minimizes the following χ^2:

$$\chi^2 = \sum_{\text{chan}(i)} \sum_{\text{jet}(j)} \sum_{\text{mass}(m)} \frac{\left(D_m^{ij} - \alpha^{ij} \cdot Q_m^{ij} - k_{\mathcal{L}} \cdot k_\epsilon^i \cdot \left(k_Z^j \cdot Z_m^{ij} + O_m^{ij}\right)\right)^2}{D_m^{ij}} \tag{6.9}$$

where the parameters of the fit are:

- α^{ij}, the multijet scale factors that apply to Q_m^{ij};
- $k_{\mathcal{L}}$ (fixed to unity), a luminosity correction factor that applies to Z_m^{ij} and O_m^{ij};
- k_ϵ^i, the lepton efficiency scale factors (independent of jet-multiplicity) for channel i that are applied to Z_m^{ij} and O_m^{ij};
- k_Z^j, the Z/γ^*+jets cross section scale factors that apply to Z_m^{ij}. The k_Z^j are expected to be independent of data-taking periods, since these are the cross section scale factor for the Z/γ^*+jets production, any time-dependent detector

effects should be absorbed by k_ϵ^i. In particular, k_Z^0 is fixed to 1.0, which is equivalent to assuming that the inclusive Z/γ^* cross-section is known exactly.

The normalization factors are determined by a two-step fitting procedure:
(1) All parameters are free and fit in the extended range $40 < M_{\ell\ell} < 150$ GeV, of which α^{ij} will be determined at this stage. The low di-lepton invariant mass region is dominated by multijet events, and is used in the combined fit to constrain the multijet normalization. As the cuts differ for each channel and the efficiency may depend on jet-multiplicity, a separate multijet scale-factor (α^{ij}) is fit for each channel and jet-multiplicity bin.
(2) The multijet factors α^{ij} are fixed and the fit is repeated in a tighter mass range $60 < M_{\ell\ell} < 150$ GeV. As the inclusive Z/γ^*+jets cross-section, dominated by the zero-jet bin, is known to much better accuracy than the Z/γ^*+$2j$ cross-section, the zero-jet bin is used to constrain lepton efficiency factors (k_ϵ^i), which is applied to every MC sample. The 1jet ($\geq$ 2jets) sample is used to determine k_Z^1 (k_Z^2).

The normalization results for the Run 2A data are not consistent with the results from the Run 2B data. For this reason, two separate fits are performed: 1) using the Run 2A channels only, and 2) using the Run 2B channels only. The fit results for the Run 2A and Run 2B data samples are presented in Tables 6.4 and 6.5, respectively. To account for this observed discrepancy, an additional systematic uncertainty is applied, as discussed in Section 7.3.

The α^{ij} varies significantly with jet multiplicity in the $\mu\mu$ channels. This may be understood by noting that this parameter is the ratio of the selection efficiency for multijet events in the analysis sample to the selection efficiency in the multijet control sample. In the case of the $\mu\mu$ channel, these two samples differ by the muon isolation requirement. Therefore, the presence of additional hadronic activity can have a large impact on this ratio.

Table 6.4: Combined normalization fit results for Run 2A. Only the statistical uncertainties are shown. By construction, the uncertainty on α^{ij} is zero for the $\mu\mu_{\mathrm{TRK}}$ channels. Likewise, the uncertainty on k_Z^0 is also zero.

Channel	k_ϵ^i	α^{i0}	α^{i1}	α^{i2}
		Run 2A		
CC-CC	1.031 ± 0.005	0.34 ± 0.01	0.29 ± 0.03	0.14 ± 0.06
CC-EC	1.013 ± 0.005	0.331 ± 0.006	0.27 ± 0.01	0.29 ± 0.03
ee_{ICR}	1.018 ± 0.007	0.117 ± 0.010	0.07 ± 0.02	0.01 ± 0.03
$\mu\mu$	0.925 ± 0.003	1.4 ± 0.1	0.46 ± 0.03	0.44 ± 0.05
$\mu\mu_{\mathrm{TRK}}$	0.907 ± 0.009	1	1	1

k_Z^0	1
k_Z^1	0.970 ± 0.007
k_Z^2	1.06 ± 0.02

6.5.2 Internal Consistency of the Normalization Procedure

As a cross check, we repeat the normalization procedure independently for each channel. All the tables could be found in Appendix A. Because the parameters k_ϵ^i and α^{ij} are sensitive to a specific channel, we expect small difference in the values of these parameters from the combined fit and from the independent fits. The results for k_ϵ^i and α^{ij} are in general agreement with these expectations. The k_Z^j parameters are constrained by all channels, more variations are possible, but values are all consistent within the statistical uncertainties of the independent fits.

6.6 Event yields at the preselection level

With all the corrections applied to MC samples, the event yields for each epoch of the di-muon channel may be found in Tab. 6.6 - 6.9. The uncertainty in the table associated with each background is only the statistical uncertainty from the available MC statistics A selection of event yield plots of inclusive and $2j$-pretag samples are included in Appendix. C.

Table 6.5: Combined normalization fit results for Run 2B. Only the statistical uncertainties are shown. on α^{ij} is zero for the $\mu\mu_{\mathrm{TRK}}$ channels. Likewise, the uncertainty on k_Z^0 is also zero.

Channel	k_ϵ^i	α^{i0}	α^{i1}	α^{i2}
		Run 2B1		
CC-CC	0.989 ± 0.005	0.179 ± 0.005	0.129 ± 0.004	0.140 ± 0.010
CC-EC	0.973 ± 0.005	0.168 ± 0.002	0.147 ± 0.003	0.152 ± 0.005
ee_{ICR}	0.968 ± 0.006	0.108 ± 0.002	0.079 ± 0.003	0.099 ± 0.006
$\mu\mu$	0.968 ± 0.003	1.400 ± 0.200	0.440 ± 0.020	0.310 ± 0.030
$\mu\mu_{\mathrm{TRK}}$	1.04 ± 0.01	1	1	1
		Run 2B2		
CC-CC	1.015 ± 0.003	0.099 ± 0.001	0.114 ± 0.002	0.139 ± 0.005
CC-EC	1.008 ± 0.004	0.095 ± 0.001	0.111 ± 0.001	0.137 ± 0.002
ee_{ICR}	0.918 ± 0.004	0.077 ± 0.002	0.065 ± 0.003	0.061 ± 0.005
$\mu\mu$	0.982 ± 0.002	1.500 ± 0.100	0.410 ± 0.020	0.410 ± 0.020
$\mu\mu_{\mathrm{TRK}}$	1.034 ± 0.007	1	1	1
		Run 2B34		
CC-CC	1.044 ± 0.003	0.131 ± 0.001	0.122 ± 0.002	0.133 ± 0.004
CC-EC	1.040 ± 0.003	0.116 ± 0.001	0.112 ± 0.001	0.111 ± 0.001
ee_{ICR}	1.013 ± 0.004	0.080 ± 0.002	0.071 ± 0.002	0.061 ± 0.004
$\mu\mu$	0.990 ± 0.002	1.190 ± 0.080	0.440 ± 0.020	0.350 ± 0.020
$\mu\mu_{\mathrm{TRK}}$	1.013 ± 0.005	1	1	1

k_Z^0	1
k_Z^1	0.895 ± 0.003
k_Z^2	0.935 ± 0.007

Run 2A dimuon

	inclusive	$2j$-multijet	$2j$-pretag	ST	DT
data	107288	2393	1698	58	24
all bkg	106941 ± 125	2400 ± 14	1740.4 ± 7.9	61.0 ± 1.7	26.1 ± 1.2
Multijet	2722 ± 53	283 ± 11	53.5 ± 4.8	4.8 ± 1.5	2.6 ± 1.1
Zjj	100882 ± 113	1622.3 ± 7.1	1320.1 ± 5.7	5.21 ± 0.48	0.363 ± 0.095
$Zb\bar{b}$	844.5 ± 3.2	120.7 ± 1.3	99.9 ± 1.2	28.34 ± 0.61	11.56 ± 0.36
$Zc\bar{c}$	2210.6 ± 7.4	257.3 ± 2.7	210.3 ± 2.4	14.17 ± 0.54	3.01 ± 0.27
ZZ	52.03 ± 0.26	19.52 ± 0.17	16.30 ± 0.15	1.383 ± 0.049	1.007 ± 0.039
WZ	59.08 ± 0.34	19.06 ± 0.20	15.81 ± 0.18	0.709 ± 0.038	0.096 ± 0.017
WW	75.7 ± 1.2	7.46 ± 0.42	2.29 ± 0.24	0.132 ± 0.044	0.0061 ± 0.0047
$t\bar{t}$	95.41 ± 0.54	70.74 ± 0.48	22.23 ± 0.26	6.21 ± 0.14	7.43 ± 0.13
$ZH(125)$	1.1990 ± 0.0059	0.7080 ± 0.0048	0.5902 ± 0.0044	0.1621 ± 0.0024	0.1717 ± 0.0022

Table 6.6: Event yields for the dimuon ($\mu\mu$) channel – Run 2A.

Run 2B1 dimuon

	inclusive	$2j$-multijet	$2j$-pretag	ST	DT
data	97754	2142	1599	49	24
all bkg	97924 ± 60	2194.2 ± 7.6	1669.1 ± 3.8	63.7 ± 1.3	31.32 ± 0.84
Multijet	1923 ± 45	163.5 ± 7.1	29.9 ± 3.0	5.2 ± 1.3	2.16 ± 0.82
Zjj	92899 ± 41	1547.1 ± 2.6	1283.8 ± 2.3	4.47 ± 0.16	0.308 ± 0.046
$Zb\bar{b}$	782.9 ± 1.0	112.15 ± 0.39	93.76 ± 0.34	27.46 ± 0.17	13.96 ± 0.12
$Zc\bar{c}$	2025.1 ± 2.2	241.67 ± 0.49	199.50 ± 0.38	17.05 ± 0.11	3.550 ± 0.059
ZZ	53.67 ± 0.20	20.76 ± 0.12	17.55 ± 0.11	1.543 ± 0.037	1.423 ± 0.033
WZ	61.47 ± 0.25	20.06 ± 0.14	16.83 ± 0.13	0.859 ± 0.027	0.144 ± 0.014
WW	74.31 ± 0.48	7.43 ± 0.16	2.282 ± 0.088	0.132 ± 0.022	0.0212 ± 0.0086
$t\bar{t}$	104.90 ± 0.49	81.47 ± 0.44	25.41 ± 0.24	6.94 ± 0.12	9.75 ± 0.14
$ZH(125)$	1.2078 ± 0.0063	0.7489 ± 0.0051	0.6297 ± 0.0046	0.1712 ± 0.0025	0.2201 ± 0.0025

Table 6.7: Event yields for the dimuon ($\mu\mu$) channel – Run 2B1.

Run 2B2 dimuon

	inclusive	$2j$-multijet	$2j$-pretag	ST	DT
data	216179	5071	3734	137	56
all bkg	216036 ± 130	5132 ± 18	3782 ± 11	124.8 ± 2.1	59.2 ± 1.8
Multijet	4757 ± 72	515 ± 15	108.9 ± 6.7	9.4 ± 2.0	7.4 ± 1.7
Zjj	204313 ± 108	3525.5 ± 10.0	2879.3 ± 9.0	5.01 ± 0.21	0.171 ± 0.023
$Zb\bar{b}$	1763.4 ± 2.5	257.7 ± 1.0	211.48 ± 0.94	59.39 ± 0.52	25.63 ± 0.30
$Zc\bar{c}$	4566.4 ± 5.6	548.8 ± 2.1	445.9 ± 1.8	30.35 ± 0.48	5.16 ± 0.18
ZZ	116.11 ± 0.40	46.04 ± 0.27	38.48 ± 0.25	3.146 ± 0.084	2.612 ± 0.072
WZ	131.99 ± 0.63	44.09 ± 0.38	36.61 ± 0.35	1.554 ± 0.075	0.221 ± 0.031
WW	161.0 ± 1.2	16.95 ± 0.44	5.42 ± 0.25	0.238 ± 0.058	0.0114 ± 0.0079
$t\bar{t}$	226.9 ± 1.1	178.1 ± 1.1	55.87 ± 0.56	15.64 ± 0.33	18.03 ± 0.32
$ZH(125)$	2.613 ± 0.015	1.699 ± 0.013	1.409 ± 0.012	0.3909 ± 0.0066	0.4152 ± 0.0062

Table 6.8: Event yields for the dimuon ($\mu\mu$) channel – Run 2B2.

Run 2B3-4 dimuon

	inclusive	$2j$-multijet	$2j$-pretag	ST	DT
data	319124	7586	5621	191	93
all bkg	319356 ± 228	7536 ± 26	5610 ± 20	183.7 ± 2.6	90.9 ± 1.9
Multijet	6332 ± 73	715 ± 16	136.5 ± 6.9	11.6 ± 2.0	8.1 ± 1.7
Zjj	303010 ± 216	5255 ± 20	4330 ± 18	14.7 ± 1.3	0.97 ± 0.36
$Zb\bar{b}$	2505.5 ± 3.6	366.5 ± 1.5	303.6 ± 1.3	84.07 ± 0.67	40.19 ± 0.45
$Zc\bar{c}$	6579.9 ± 8.5	783.0 ± 3.0	638.0 ± 2.6	44.45 ± 0.64	8.79 ± 0.29
ZZ	172.7 ± 1.0	68.66 ± 0.64	57.20 ± 0.58	4.86 ± 0.19	4.20 ± 0.17
WZ	196.9 ± 1.5	67.58 ± 0.87	56.33 ± 0.78	2.30 ± 0.16	0.396 ± 0.076
WW	232.7 ± 1.8	24.20 ± 0.63	7.26 ± 0.35	0.469 ± 0.096	0.170 ± 0.088
$t\bar{t}$	325.9 ± 2.2	255.9 ± 2.0	80.8 ± 1.1	21.32 ± 0.56	28.12 ± 0.58
$ZH(125)$	3.787 ± 0.031	2.462 ± 0.025	2.056 ± 0.023	0.538 ± 0.012	0.667 ± 0.013

Table 6.9: Event yields for the dimuon ($\mu\mu$) channel – Run 2B34.

CHAPTER VII

Data Analysis

After a good background modeling achieved in the control region, some high-level techniques are used in this analysis to approach a better sensitivity of the Higgs search. A kinematic fit is used to improve the di-jet invariant mass resolution (Sect. 7.1). The multivariate technique is used to further separate the signal from backgrounds in the signal regions (Sect. 7.2). At the end of this chapter, the systematic uncertainties are discussed (Sect. 7.3).

7.1 Kinematic Fit

As we are searching for the SM Higgs boson in the $b\bar{b}$ decay mode, the invariant mass of the two b-jet will give the mass of the reconstructed Higgs boson. For $M_H \lesssim 130$ GeV, the Higgs boson width is quite narrow ($\Gamma_H < 10$ MeV); however, the detector resolution of the dijet invariant mass at such mass range is ~ 17 GeV. So it is important to improve the dijet invariant mass resolution at the analysis level. A so-called "kinematic fit" procedure is adopted in the ZH analysis to improve the resolution of the dijet invariant mass. This procedure is based on the fact that:
(1) in the DØ detector, lepton energies are measured more precisely than jet energies.
(2) there is no neutrino in the final states of $ZH \to \ell^+\ell^- b\bar{b}$, so the transverse momentum of the ZH system should be balanced in its center-of-mass frame.

(3) furthermore, the p_{T} boost of the ZH system is moderate for the majority of events.

To make optimal use of the available kinematic information, the energies and angles of the two leptons that form the Z candidate, the two jets that form the Higgs candidate, and the third jet (if present), are fit within their resolutions to values which minimizes a log likelihood function (see Sect. 7.1.1) with following constraints:

- the $M_{\ell\ell}$ distribution should follow a Breit-Wigner distribution with a mean of $M_Z = 91.188$ GeV and a width of $\Gamma_Z = 2.4952$ GeV;
- the vector sum of the p_{T} along x and y directions, Σp_x and Σp_y, should both follow a Gaussian distribution with a mean of 0 GeV and a width of 7 GeV.

When there are three jets in a event, all these three jets are fit using the same constraints as in the case of a two jet event, with the modification that the third jet is included in the calculation of Σp_x and Σp_y. If a event has more than three jets, it is treated as the three jets case: two jets from the dijet system as described in Sect. 5.4, and one more highest-p_{T} jet from the remaining ones. The fit contains twelve independent observables for events with two jets: four particles $\times$ three variables (E for electrons/jets or $1/p_{\mathrm{T}}$ for muons, η_{det} and ϕ). For events with three jets, there are three more variables (E, η_{det} and ϕ) for the third jet.

Performance of this kinematic fit was studied using the Run 2B $\mu\mu$ samples at the pretag level. Typically, this technique yields an improvement of 15% in the dijet mass resolution, depending on M_H. When $M_H = 125$ GeV, the dijet mass resolution is approximately 15 GeV after the kinematic fit (i.e 12% improvement, as shown in Fig. 7.1). Also, the peak value of the dijet invariant mass moved to the right position after the kinematic fit.

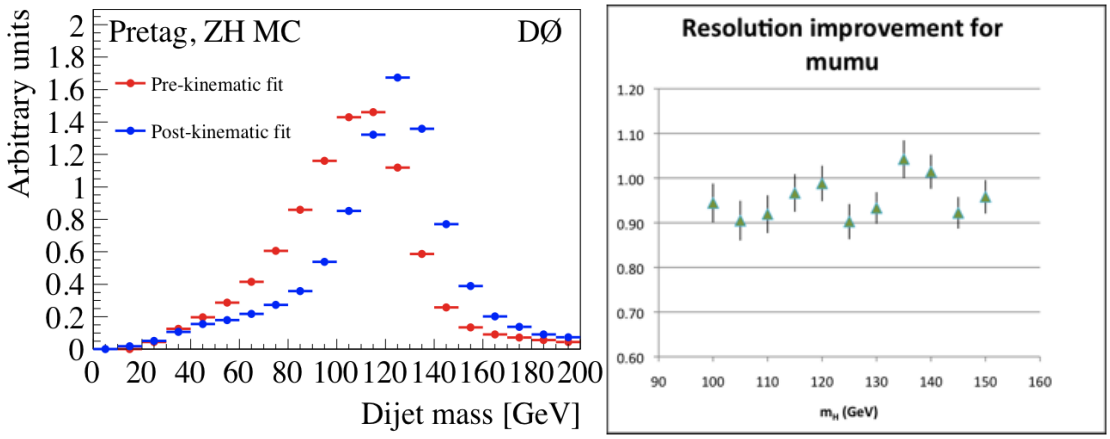

(a) (b)

Figure 7.1: The dijet mass resolution improvement from kinematic fit for (a) $M_H = 125$ GeV, and (b) all M_H values.

7.1.1 Likelihood fit

The kinematic fit minimizes a negative log likelihood function:

$$-\ln L_{fit} = -\sum_i \ln f_i(y_i^{obs}, y_i^{pred}) - \sum_j \ln C_j \tag{7.1}$$

f_i is the probability density (transfer function) for a variable y_i^{pred} being measured as y_i^{obs}, where i stands for E or $1/p_{\mathrm{T}}$, η_{det} and ϕ of all the leptons and jets included in the fit. The η_{det} and ϕ measurements of both lepton and jet are assumed to have a Gaussian transfer function, with a width equals to their resolutions. (see Sect. 7.1.2). The transverse momenta of muons are measured by the tracking system. The uncertainties on the curvature measurement and therefore $1/p_T$ are assumed to be a Gaussian distribution (see Sect. 7.1.3). The transfer functions for the jet energy resolution has a non-Gaussian form, and the detail is described in Sect. 7.1.4.

The C_j (j = BW, $\sum p_x$, $\sum p_y$) are the probability densities for the three kinematic constraints:

- The relativistic Breit-Wigner function used for the Z mass constraint is

$$C_{BW} = \frac{1}{(m^2 - m_Z^2)^2 + m_Z^2\Gamma_Z^2},\ M_Z = 91.188\text{GeV},\ \Gamma_Z = 2.4952\text{GeV} \quad (7.2)$$

- The constraints on $\sum p_x$ and $\sum p_y$ are

$$\begin{aligned} -\ln C_{\sum p_x} &= \frac{1}{2}\frac{(\sum p_x^{obs} - \sum p_x^{pred})^2}{\sigma^2} \\ -\ln C_{\sum p_y} &= \frac{1}{2}\frac{(\sum p_y^{obs} - \sum p_y^{pred})^2}{\sigma^2} \end{aligned} \quad (7.3)$$

where $\sigma = 7$ GeV is measured from ZH MC samples.

7.1.2 Lepton and Jet Angular Resolutions

The resolutions of the angles, listed in Tab. 7.1, are measured using the ZH MC samples and found to be constants. All lepton/jet flavors are assumed to have the same angular resolution.

Table 7.1: Lepton and jet angular resolutions.

	η_{det}	ϕ
Lepton	0.005	0.001
Jet	0.08	0.08

7.1.3 Muon Energy Resolution

The muon energy resolution is estimated from the p_T and angular resolutions of the muon track using $Z \to \mu\mu$ and $J/\psi \to \mu\mu$ events. The muon p_T resolution function is a function of muon p_T and η_{det} as shown in Eqn. 7.4, with coefficients listed in Tab. 7.2 [80].

$$\sigma(\frac{1}{p_T}) = \begin{cases} \sigma_0 + \frac{\sigma_1}{p_T} & |\eta| \leq \eta_0 \\ \sqrt{(\sigma_0 + \frac{\sigma_1}{p_T})^2 + ((c_0 + \frac{c_1}{p_T}) \times (|\eta| - |\eta_0|))^2} & |\eta| > \eta_0 \end{cases} \tag{7.4}$$

where $\eta_0 = 1.28$.

Table 7.2: Muon p_T resolution function coefficients.

	Value
σ_0	0.00244113
σ_1	0.010204
c_0	0.00677562
c_1	0.0485938

7.1.4 Jet Energy Transfer Functions

The jet energy transfer functions are derived from the ZH MC samples for three types of jets; 1) light-quark jets or gluon jets, 2) b-quark jets without a muon, and 3) b-quark jets with a muon. For the two jets that form the Higgs boson candidate, the transfer function for the b-quark jets with or without a muon is used, depending on whether the jet contains a muon or not. For the third jet, if present, the light-quark transfer function is adopted, unless the jet is identified as a jet with a muon and for that case the transfer function for the b-quark jets with a muon is used. The transfer function is parametrized as

$$\begin{aligned} TF(E^{obs}, E^{pred}) \quad &= \tfrac{1}{\sqrt{2\pi}\sigma_a}\alpha \cdot (1-\gamma) \cdot exp(-\tfrac{(x-\mu_a)^2}{2\sigma_a^2}) \\ &+ \tfrac{1}{\sqrt{2\pi}\sigma_b}\beta \cdot (1-\gamma) \cdot exp(-\tfrac{(x-\mu_b)^2}{2\sigma_b^2}) + \tfrac{\gamma}{2} \end{aligned} \tag{7.5}$$

where

$$
\begin{aligned}
x &= \frac{E^{obs} - E^{pred}}{E^{pred}} \\
\mu_a &= (p_1 + \frac{p_2}{E^{pred}}) - \beta \cdot p_5 \\
\mu_b &= (p_1 + \frac{p_2}{E^{pred}}) - \alpha \cdot p_5 \\
\sigma_a &= (p3 + \frac{p4}{E^{pred}})\sqrt{1 + \frac{p_6}{1+p_7}} \\
\sigma_b &= (p3 + \frac{p4}{E^{pred}})\sqrt{\frac{p_7}{1+p_7}} \\
\alpha &= \frac{1}{1+p_6} \\
\beta &= \frac{p_6}{1+p_6} \\
\gamma &= \frac{p_8}{1+p_8}
\end{aligned}
\tag{7.6}
$$

The transfer functions are derived separately in three η_{det} regions: $0.0 < |\eta_{det}| < 0.8$, $0.8 < |\eta_{det}| < 1.6$ and $1.6 < |\eta_{det}| < 2.5$. The parameters p_1–p_8 are listed for three types of jets and three η_{det} regions in Tab. 7.3. Figure 7.2 shows the transfer functions.

Table 7.3: Parameters for the transfer functions. Three η_{det} regions, eta1, eta2 and eta3, correspond to $0.0 < \eta_{det} < 0.8$, $0.8 < \eta_{det} < 1.6$, and $1.6 < \eta_{det} < 2.5$, respectively.

	light jet			b-quark jet			b-quark jet with a muon		
	eta1	eta2	eta3	eta1	eta2	eta3	eta1	eta2	eta3
p_1	-0.100	-0.156	-0.184	-0.0264	-0.112	-0.149	-0.107	-0.170	-0.227
p_2	2.46	8.07	15.3	-6.91	-2.43	2.59	1.52	7.47	17.3
p_3	0.0899	0.123	0.131	0.0711	0.145	0.181	0.0970	0.162	0.159
p_4	3.40	4.31	5.30	4.69	3.55	1.86	3.61	2.76	1.83
p_5	0.235	0.193	0.219	0.298	0.0730	0.00637	0.268	0.102	0.272
p_6	0.234	0.538	0.430	7.25	0.298	4.36e-6	3.91	0.0687	0.124
p_7	0.918	1.42	1.16	8.51e7	0.753	1.15	2.29e7	0.292	0.786
p_8	0.0147	0.00557	0.00697	0.0113	0.00510	0.00582	0.0108	0.00689	0.0105

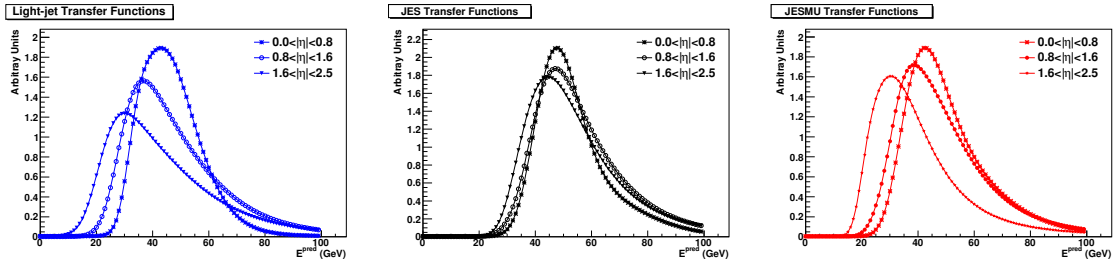

(a) (b) (c)

Figure 7.2: The transfer functions at $E = 40$ GeV for the (a) light-quark jets, (b) b-quark jets without a muon, and (c) b-quark jets with a muon. for $E = 40$ GeV.

7.2 Multivariate Analysis

In order to improve the separation of signal from background using the most significant kinematic information, a multivariate analysis (MVA) using the TMVA software package, version 4.1.0 [81] is used. Of the many options available, the random forest (RF) outperformed other techniques, as it is found to have more efficient use of correlated input variables (in the ZH analysis, variables before and after kinematic fit are all used as inputs for MVA).

A two-step process is performed in this analysis:

(1) in the first step, a dedicated RF ($t\bar{t}$ RF), which takes $t\bar{t}$ as the only background and ZH as the signal, is trained. The $t\bar{t}$ is the second dominant background in this analysis, and more importantly, it is a reducible background – some unique signatures of $t\bar{t}$ events, for instance the presence of a large $\not\!\!E_{\mathrm{T}}$, making it distinguishable from our signal. The distributions of the $t\bar{t}$ RF variable can be found in Sect. 7.2.1. At the end of this step, all the post-tag events are split to two independent samples according to its $t\bar{t}$ RF value – $t\bar{t}$ enriched region ($t\bar{t}$ RF ≤ 0.5) and $t\bar{t}$ depleted region ($t\bar{t}$ RF >0.5).

(2) in the second step, for each of the $t\bar{t}$ enriched and depleted samples, a global RF variable is trained to separate the signal from all backgrounds. The distributions

of the global RF variable can be found in Sect. 7.2.2. The global RF is the final discriminant variable used to extract the limit on the Higgs production cross section.

In both steps, ST and DT events are treated independently, and the discriminant is trained separately for each assumed value of M_H. In total, four final discriminant distributions are obtained for each Higgs mass point: for ST events in the 1) $t\bar{t}$ enriched and 2) depleted regions, and for DT events in the 3) $t\bar{t}$ enriched and 4) depleted regions. All lepton channels and epochs are combined together during the RF training. The event yields of all lepton channels summed together are shown in Tab. 7.4, and event yields in $t\bar{t}$ enriched region and $t\bar{t}$ depleted regions are summarized in Tab. 7.5 and 7.6, respectively. From those tables, it is clearly seen that the main sensitivity comes from the DT $t\bar{t}$ depleted region, where the $S/\sqrt{B}$ value has been improved by $\sim 27\%$ comparing to the value before employing the $t\bar{t}$ RF (Tab. 7.4). Though the contribution from the $t\bar{t}$ enriched regions is only a few percent of the total sensitivity, they are still included in the analysis to make the systematic uncertainties under control.

Table 7.4: Event yields in the without applying a requirement on the $t\bar{t}$ RF, summed over all epochs and lepton channels.

	inclusive	$2j$-multijet	$2j$-pretag	ST	DT
data	1.84517e+06	34175	25849	886	373
all bkg	1841683 ± 432	33748 ± 46	25658 ± 33	824.3 ± 4.9	366.4 ± 3.3
Multijet	160746 ± 200	4579 ± 34	1284 ± 17	54.4 ± 4.0	25.7 ± 3.0
Zjj	1630391 ± 382	22594 ± 30	19253 ± 27	59.6 ± 1.8	3.50 ± 0.44
$Zb\bar{b}$	12768.7 ± 8.0	1603.6 ± 3.0	1375.1 ± 2.8	389.0 ± 1.4	179.02 ± 0.91
$Zc\bar{c}$	33693 ± 18	3461.4 ± 6.0	2930.0 ± 5.4	211.1 ± 1.3	39.82 ± 0.57
ZZ	811.0 ± 1.6	291.92 ± 0.96	252.28 ± 0.88	21.00 ± 0.29	17.71 ± 0.26
WZ	958.7 ± 2.3	292.1 ± 1.3	254.5 ± 1.2	10.91 ± 0.25	1.33 ± 0.10
WW	1144.5 ± 3.6	74.3 ± 1.0	23.68 ± 0.57	1.16 ± 0.13	0.252 ± 0.091
$t\bar{t}$	1170.3 ± 2.9	851.9 ± 2.6	284.8 ± 1.4	77.18 ± 0.75	99.02 ± 0.78
$ZH(125)$	17.326 ± 0.047	10.524 ± 0.038	9.193 ± 0.036	2.491 ± 0.019	2.892 ± 0.020

To avoid any training or optimization biases, the MC samples are randomly divided into three orthogonal sub-samples: 25% of the events are used to train the RFs (for both the $t\bar{t}$ RF and the global RF), 25% of the events are used to test the RF

Table 7.5: Event yields in the $t\bar{t}$ enriched sample, summed over all epochs and lepton channels.

	$2j$-pretag	ST	DT
data	7245	159	160
all bkg	7032 ± 19	149.5 ± 3.1	166.4 ± 2.8
Multijet	596 ± 13	23.8 ± 3.0	18.5 ± 2.7
Zjj	4963 ± 14	4.74 ± 0.43	1.16 ± 0.26
$Zb\bar{b}$	370.0 ± 1.5	35.04 ± 0.46	45.17 ± 0.47
$Zc\bar{c}$	751.5 ± 2.8	15.41 ± 0.36	9.78 ± 0.27
ZZ	33.44 ± 0.33	1.395 ± 0.077	1.383 ± 0.083
WZ	39.86 ± 0.50	0.876 ± 0.088	0.481 ± 0.060
WW	19.70 ± 0.53	0.80 ± 0.11	0.227 ± 0.089
$t\bar{t}$	258.2 ± 1.4	67.43 ± 0.70	89.71 ± 0.75
$ZH(125)$	1.321 ± 0.015	0.1792 ± 0.0055	0.1814 ± 0.0056

Table 7.6: Event yields in the $t\bar{t}$ depleted sample, summed over all epochs and lepton channels.

	$2j$-pretag	ST	DT
data	23351	727	213
all bkg	23289 ± 30	674.8 ± 3.7	200.0 ± 1.8
Multijet	930 ± 13	30.6 ± 2.7	7.3 ± 1.4
Zjj	17891 ± 26	54.9 ± 1.7	2.35 ± 0.35
$Zb\bar{b}$	1247.8 ± 2.7	353.9 ± 1.4	133.85 ± 0.78
$Zc\bar{c}$	2701.5 ± 5.2	195.7 ± 1.3	30.04 ± 0.50
ZZ	236.43 ± 0.85	19.61 ± 0.28	16.33 ± 0.25
WZ	235.9 ± 1.2	10.03 ± 0.23	0.848 ± 0.083
WW	6.07 ± 0.27	0.354 ± 0.077	0.025 ± 0.014
$t\bar{t}$	40.64 ± 0.54	9.75 ± 0.25	9.31 ± 0.21
$ZH(125)$	8.497 ± 0.034	2.311 ± 0.019	2.710 ± 0.019

performance (for both the $t\bar{t}$ RF and the global RF), and the remaining 50% of the events (the evaluation sample) are used in the statistical analysis to produce control plots and extract limits. The evaluation sample is independent of both the training and testing samples and the training/optimization bias will be minimized.

Table 7.7 shows the input variables used for the RF training, and distributions of a few selected input variables are shown in Fig. 7.3-7.4 for ST and DT events.

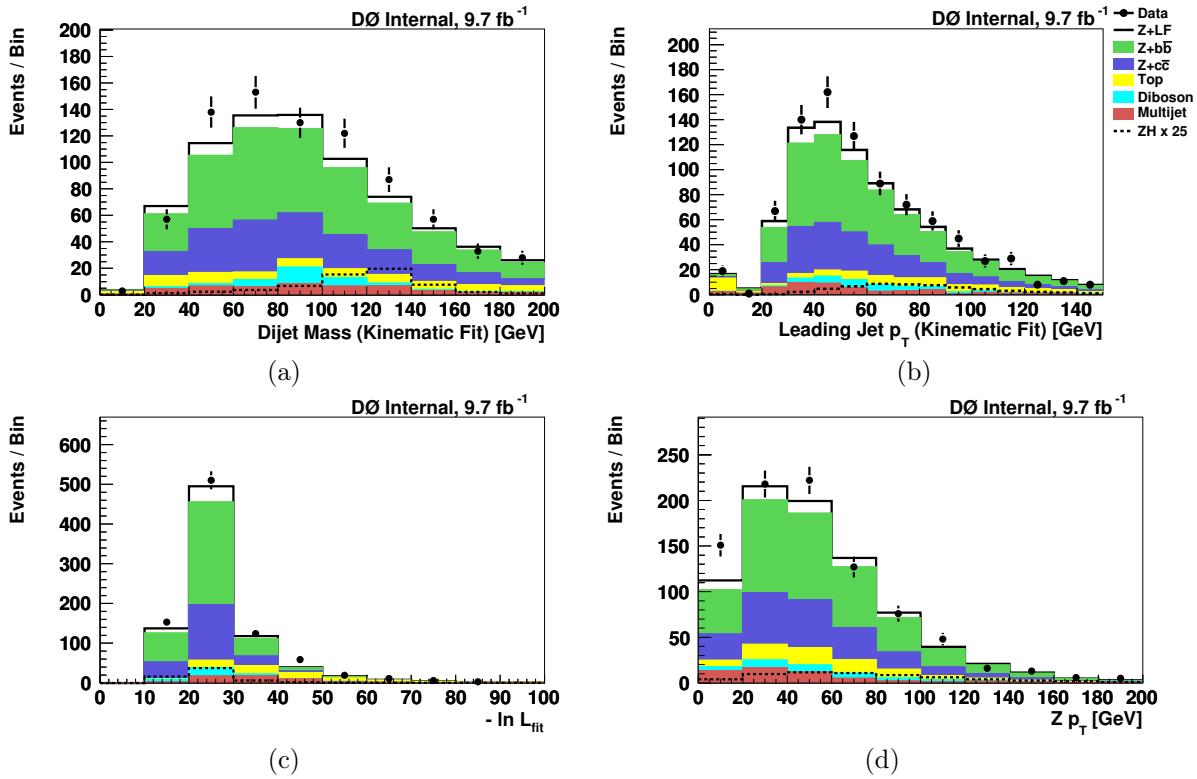

Figure 7.3: Distribution in ST events (summed over all lepton channels and epochs) of (a) the dijet mass from the kinematic fit, (b) the p_{T} of the leading jet from the kinematic fit, (c) $-\ln L_{fit}$ from the kinematic fit, and (d) the p_{T} of the dilepton system.

7.2.1 The $t\bar{t}$ RF

Taking the $M_H = 125$ GeV case as an example, the $t\bar{t}$ RF output from the training and testing samples are compared in Fig. 7.5. These plots, as well as those in Fig. 7.7 and 7.9, are the only RF output plots presented using the training (25%) and

Table 7.7: Variables used for the $t\bar{t}$ and global RF training.

variables	definition	$t\bar{t}$ RF	global RF
$M_{bb}(M_{bb}{}^{fit})$	invariant mass of the dijet system before (after) the kinematic fit	$\surd$	$\surd$
$p_{\mathrm{T}}^{b1}(p_{\mathrm{T}}^{b1\,fit})$	transverse momentum of the leading jet before (after) kinematic fit	$\surd$	$\surd$
$p_{\mathrm{T}}^{b2}(p_{\mathrm{T}}^{b2\,fit})$	transverse momentum of the other jet before (after) kinematic fit	$\surd$	$\surd$
p_{T}^{bb}	transverse momentum of the dijet system before the kinematic fit	$\surd$	$\surd$
$\Delta\phi(b_1, b_2)$	$\Delta\phi$ between the two jets in the dijet system	–	$\surd$
$\Delta\eta(b_1, b_2)$	$\Delta\eta$ between the two jets in the dijet system	–	$\surd$
$M(\sum \vec{j_i})$	invariant mass of all jets in the event (the multijet mass)	$\surd$	$\surd$
$p_{\mathrm{T}}(\sum \vec{j_i})$	transverse momentum of all jets in the event	$\surd$	$\surd$
$H_T(\sum \vec{j_i})$	scalar sum of the transverse momenta of all jets in the event	$\surd$	–
$p_{\mathrm{T}}^{bb}/(\lvert p_{\mathrm{T}}^{b1}\rvert + \lvert p_{\mathrm{T}}^{b2}\rvert)$	ratio of dijet system p_T over the scalar sum of the p_T of the two jets	$\surd$	–
M_{ll}	invariant mass of the dilepton system	$\surd$	–
p_{T}^{Z}	transverse momentum of the dilepton system	$\surd$	$\surd$
$\Delta\phi(\ell_1, \ell_2)$	$\Delta\phi$ between the two leptons	$\surd$	$\surd$
colinearity(ℓ_1, ℓ_2)	cosine of the angle between the two leptons (colinearity)	$\surd$	$\surd$
$\Delta\phi(Z, jj)$	angle between the dilepton and dijet system in ϕ direction	$\surd$	$\surd$
$\cos(\theta^*)$	angle between the incoming proton and the Z in the zero momentum frame [82]	–	$\surd$
$M(\ell\ell bb)$	Invariant mass the dilepton plus dijet system	–	$\surd$
$H_T(\ell\ell bb)$	Scalar sum of the transverse momenta of the leptons and jets	–	$\surd$
$\not{E}_{\mathrm{T}}$	missing transverse energy of the event	$\surd$	–
$\not{E}_{\mathrm{T}}^{sig}$	the $\not{E}_{\mathrm{T}}$ significance [83]	$\surd$	$\surd$
$-\ln\ L_{fit}$	Log likelihood from the kinematic fit	$\surd$	$\surd$
$t\bar{t}$ `RF`	$t\bar{t}$ RF output	–	$\surd$

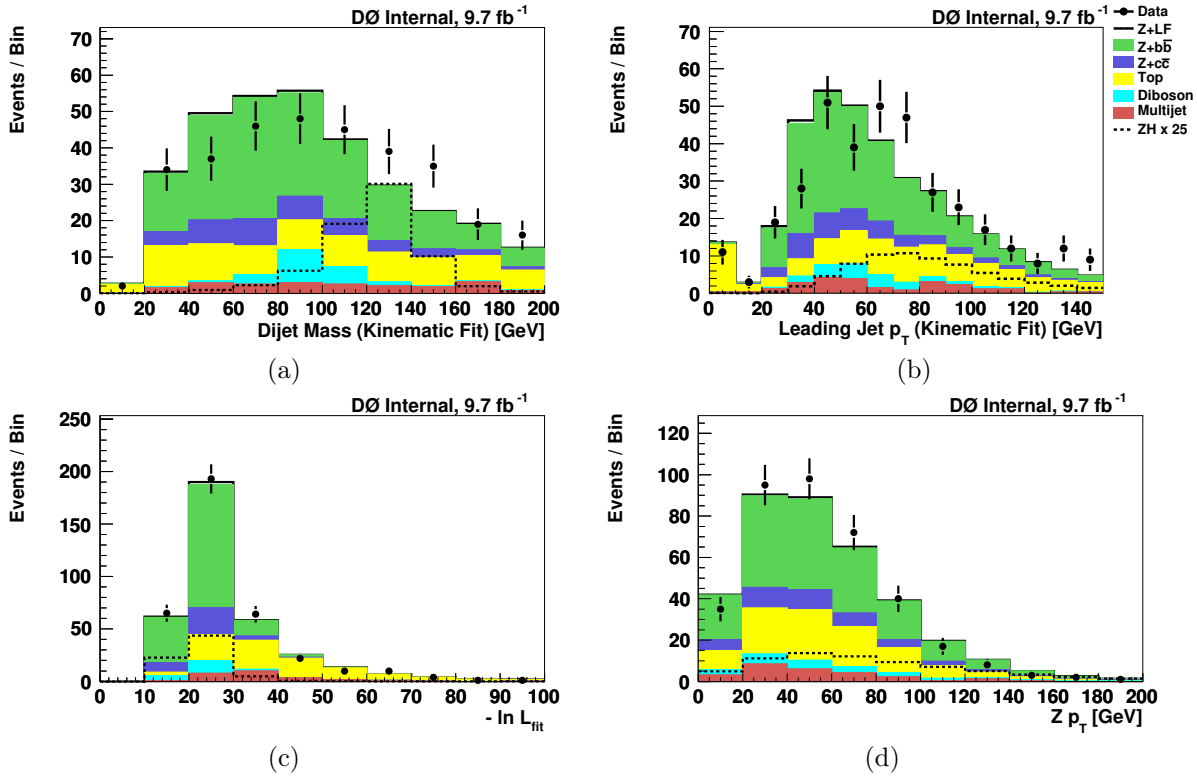

Figure 7.4: Distribution in DT events (summed over all lepton channels and epochs) of (a) the dijet mass from the kinematic fit (b) the p_{T} of the leading jet from the kinematic fit, (c) $-\ln L_{fit}$ from the kinematic fit, and (d) the p_{T} of the dilepton system.

testing (25%) samples. All other plots use the independent evaluation sample (50%). The distributions of the $t\bar{t}$ RF output ($M_H = 125$ GeV) for the evaluation sample are shown in Fig. 7.6.

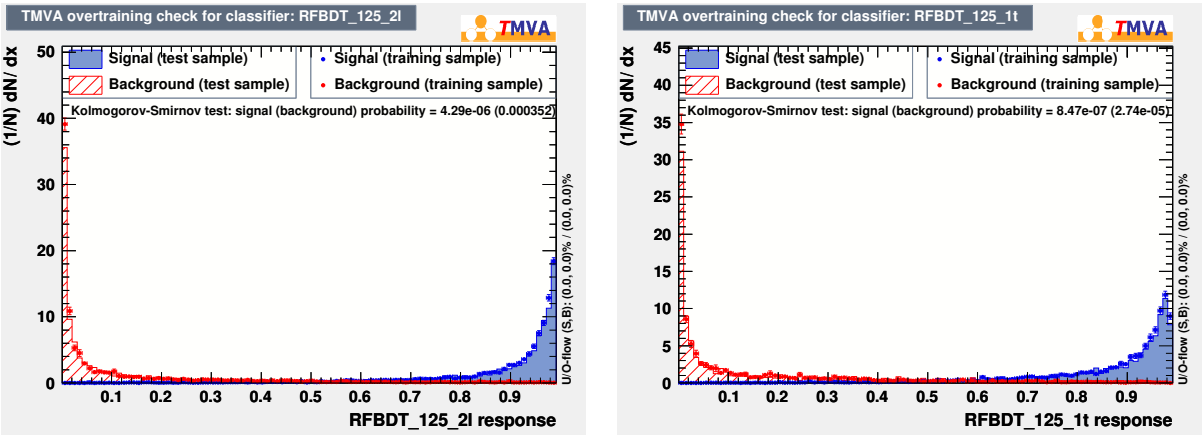

(a) all DT (b) all ST

Figure 7.5: The $t\bar{t}$ RF output of the testing and training samples ($m_H = 125$ GeV) for all lepton channels combined: (a) DT and (b) ST.

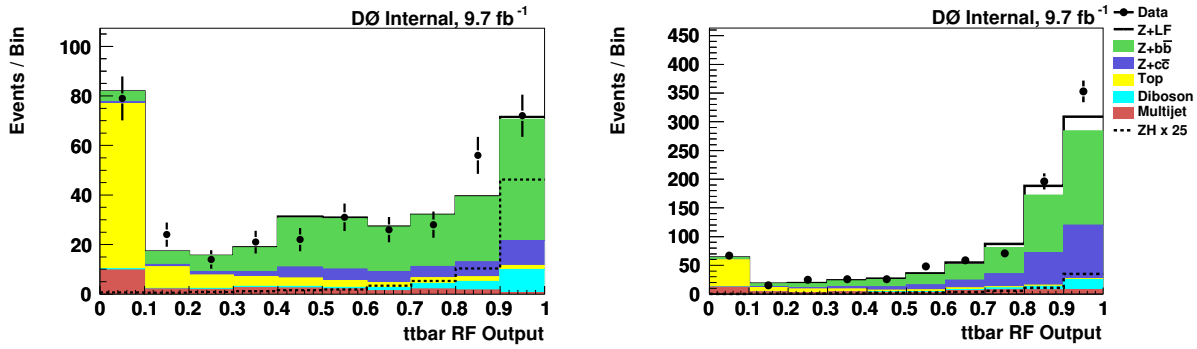

(a) all DT (b) all ST

Figure 7.6: The $t\bar{t}$ RF output ($m_H = 125$ GeV) for all lepton channels combined (a) DT and (b) ST.

The $t\bar{t}$ enriched sample consisted of events with $t\bar{t}$ RF < 0.5; and the $t\bar{t}$ depleted sample with $t\bar{t}$ RF > 0.5. This cut is chosen by optimizing the signal over background ratio, considering all Higgs mass points from 90 to 150 GeV.

7.2.2 The Global RF

Comparisons of the global RF (M_H = 125 GeV) from the training and testing samples are shown in Fig. 7.7. The global RF distribution of the evaluation sample for a Higgs mass of 125 GeV in the $t\bar{t}$ enriched and depleted regions are shown in Figure 7.8. Figure 7.9 shows the comparision of the global RF distributions between the evaluation sample and the sum of the testing and training samples, which has demonstrated that there is no bias introduced by using the same samples to train the $t\bar{t}$ RF and the global RF.

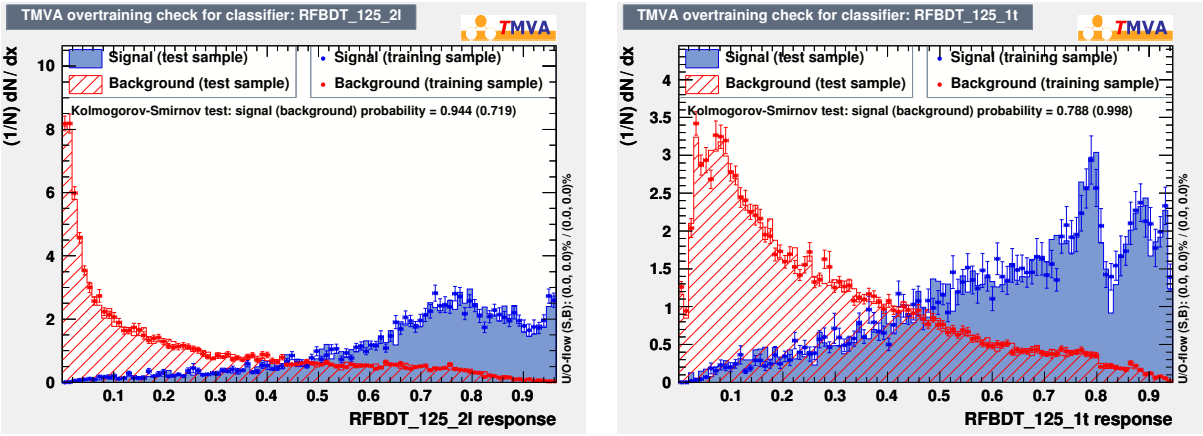

(a) all DT (b) all ST

Figure 7.7: The final discriminant output of the testing and training samples (m_H = 125 GeV) for all lepton channels combined: (a) DT and (b) ST. Here the $t\bar{t}$ enriched and depleted regions are added together.

7.3 Systematic Uncertainties

The impact of systematic uncertainties on the predicted global RF distributions is quantified for the signal and each background source. Unless otherwise stated, each source of systematic uncertainty is considered to be 100% correlated for each process across all samples.

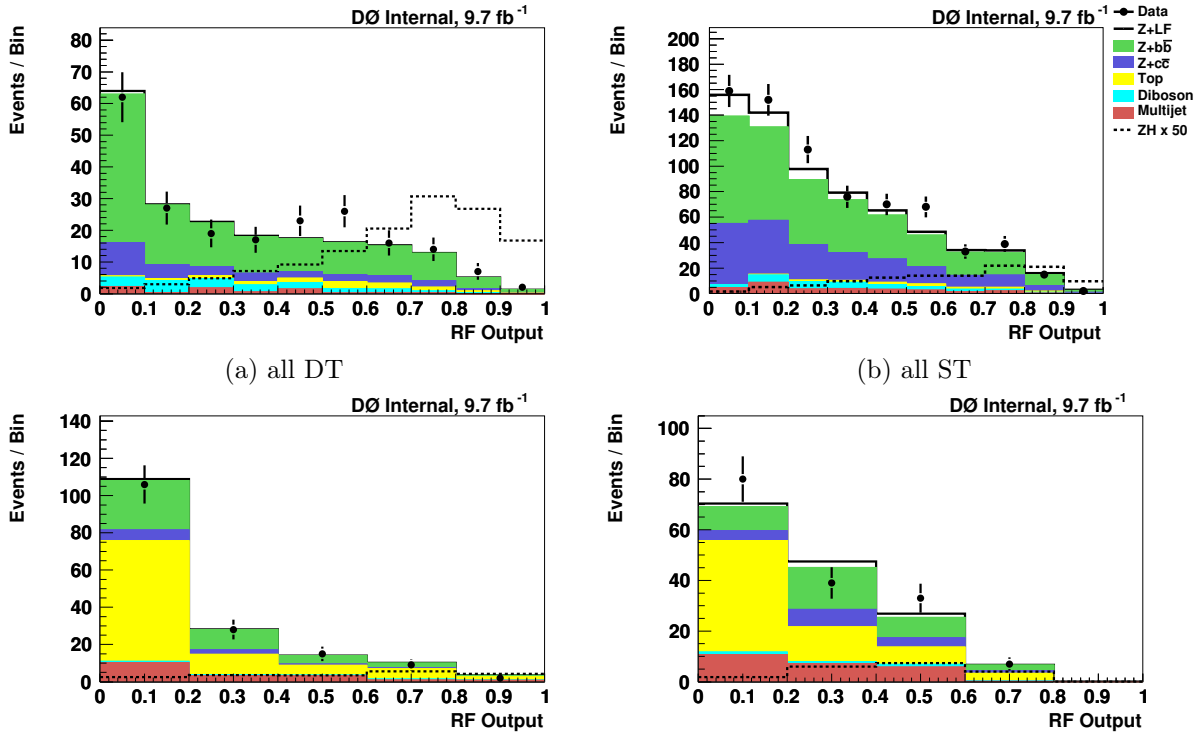

(a) all DT

(b) all ST

(c) all DT

(d) all ST

Figure 7.8: The final discriminant output (m_H = 125 GeV) for all lepton channels combined (a) DT and (b) ST final discriminant output in the $t\bar{t}$ depleted region; (c) DT and (d) ST final discriminant output in the $t\bar{t}$ enriched region.

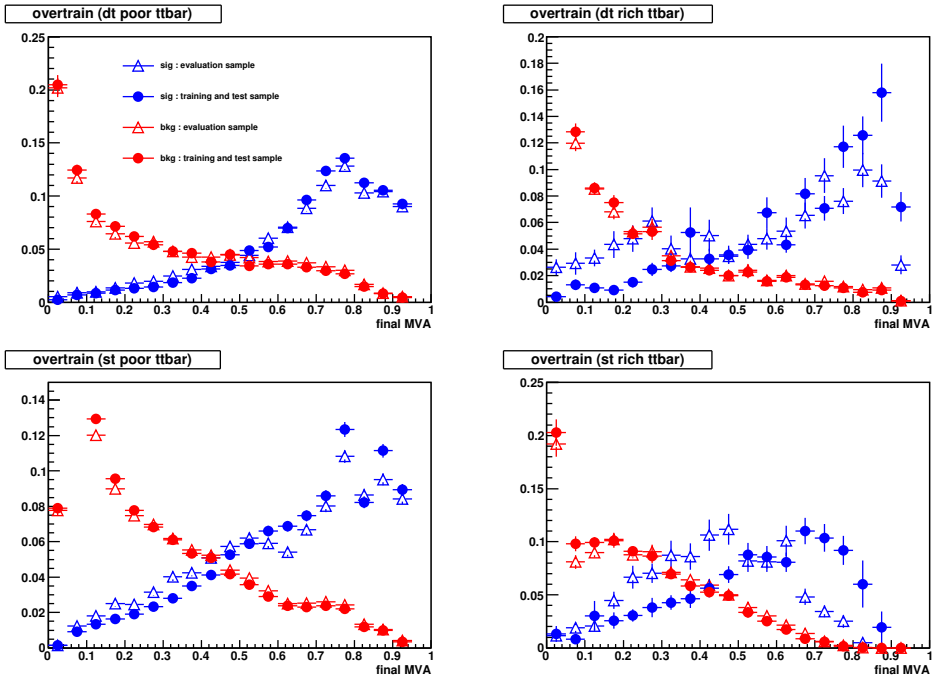

Figure 7.9: The final discriminant output of evaluation sample and the sum of testing and training samples ($m_H = 125$ GeV) for all lepton channels combined: (top left) DT events in the $t\bar{t}$ depleted region; (top right) DT events in the $t\bar{t}$ enriched region; (bottom left) ST events in the $t\bar{t}$ depleted region; (bottom right) ST events in the $t\bar{t}$-enriched region.

7.3.1 Normalization and Cross-Section Uncertainties

The uncertainties due to the normalization and production cross-sections are so-called flat systematics which scale all affected events and the corresponding RF distributions by a constant factor. All flat systematic uncertainties are summarized in Tab. 7.8.

Table 7.8: Systematic uncertainties that are common across all samples. Systematic uncertainties for ZH production shown in this table are obtained for $M_H = 125$ GeV. Relative uncertainties are given in percentage. When two numbers are given, the first is for Run 2B and the second is for Run 2A.

Relative uncertainties (%)							
Contribution	ZH	Multijet	Z+LF	$Z + b\bar{b}$	$Z + c\bar{c}$	Dibosons	$t\bar{t}$
Multijet Normalization	–	10	–	–	–	–	–
k_Z^2	–	–	0.7 / 1.8	0.7 / 1.8	0.7 / 1.8	–	–
$\sigma_\epsilon^{\mathrm{COR}}$	1.6 / 6.9	–	–	–	–	1.6 / 6.9	1.6 / 6.9
$\sigma_\epsilon^{i,\mathrm{IND}}$	5 / 3	–	5 / 3	5 / 3	5 / 3	5 / 3	5 / 3
Cross Sections	6	–	–	20	20	7	10
Run 2A Normalization	- / 9	–	–	–	–	- / 9	- / 9
PDFs	0.6	–	1.0	2.4	1.1	0.7	5.9

In this analysis, no dedicated uncertainties are assigned for the integrated luminosity and the lepton identification efficiencies, because they are absorbed by the uncertainties on the normalization procedure. The determination of the normalization constants (α^{ij}, k_ϵ^i and k_Z^j, where i stands for each channel and j stands for jet multiplicity bin) is described in Sect. 6.5, and the results quoted in Tab. 6.4 and 6.5 show statistical uncertainties only. Systematic uncertainties for the normalization procedure are evaluated in the following way:

- The uncertainties on the normalization of the multijet background (α^{ij}) are determined from the statistical uncertainties on the fit, typically around 10%. They are uncorrelated across channels but are correlated within each channel (i.e., between the ST/DT samples, and between the $t\bar{t}$ depleted and enriched regions).

- $\sigma_\epsilon^{\mathrm{COR}}$ – uncertainty from the lepton efficiency factor k_ϵ^i. In the normalization procedure, k_ϵ^i is determined using zero-jets events, which are dominated by the Z/γ^* background. That means the normalization of the $t\bar{t}$, diboson, and ZH samples will be effected by the inclusive Z boson cross section. In the "standard" normalization procedure, the k_Z^0 is fixed to 1.0 as we assume the inclusive Z/γ^*+jets cross section is known exactly. If k_Z^0 is allowed to vary according to the uncertainty on the inclusive Z cross section (6%), then it gives rise to an uncertainty on the value of k_ϵ^i. This is correlated across all channels.

- k_Z^2 uncertainty – the statistical uncertainty on the k_Z^2 from the combined fit, which is correlated across all channels.

- $\sigma_\epsilon^{i,\mathrm{IND}}$ – the RMS of the discrepancies in k_Z^2 between the value obtained from the combined normalization and the value obtained from the fit in each channel (see Tab. A.6 and A.12). This uncertainty is taken to be uncorrelated across channels.

- In the combined fit (see Eqn. 6.9), it is implicitly assumed that k_Z^j are the cross section scale factors for the Z/γ^*+jets production, so they are expected to be independent of data-taking periods. However, it is observed that the Z/γ^*+$2j$ cross section factors k_Z^2 obtained from Run 2A and Run 2B epoch (see Tab. 6.4 and 6.5) are inconsistent with each other. Because the Run 2B data is itself divided into several data-taking epochs that have mutually consistent values of k_Z^2, it is concluded that this is a discrepancy associated with Run 2A data only. So combined normalizations are performed separately for Run 2A and Run 2B epoch; and an systematic, $r(A/B) = 9\%$, large enough to cover the discrepancy in k_Z^2 is only applied to Run 2A MC samples.

The remaining uncertainties from cross-sections (with corrections described in Sect. 6.4.7) are applied to the corresponding MC samples. For the diboson and

$Z + HF$ backgrounds, the cross section uncertainties are taken to be 7% [84] and 20% [84], respectively. The cross section uncertainties for the $t\bar{t}$ background and the signal are 10% [85] and 6% [86], respectively.

A PDF uncertainty, which is actually an uncertainty on the acceptance $\times$ efficiency due to PDF, is estimated by calculating the change in event yields for each of the twenty PDF eigenvectors in CTEQ6M. These twenty uncertainties are then added in quadrature to produce a single flat uncertainty. The difference in the absolute cross section has been removed from this change in event yields. This procedure is repeated independently for each of the the following categories: signal (taking the uncertainty from the Higgs mass point with the largest change), Z/γ^*+LF, $Z/\gamma^*+c\bar{c}$, $Z/\gamma^*+b\bar{b}$, diboson and $t\bar{t}$. They are treated as correlated across all channels and all samples.

7.3.2 Systematics Changing the Shape of global RF distribution

Sources of systematic uncertainty affecting the shapes of the final discriminant distributions are the jet reconstruction uncertainties (which will effect the number of events in the signal region) and other sources that will effect event weights. Any corrections applied to MC samples would be a source of uncertainty effecting event weights. For the corrections integrated in the DØ offline analysis framework, their uncertainties are provided by the ID group with corresponding packages. For those corrections developed specifically in the ZH analysis, the covariance matrix of all model parameters is propagated to the error of the event weights, and the event weights are varied by $\pm 1\sigma$. In some cases, this method is not possible or may not adequately account for systematic uncertainties, then the event weights are adjusted by the recommended uncertainty for the correction. The magnitude of these "shape" systematic uncertainties are summarized in Tab. 7.9 - 7.10, the average per bin (of the global RF distribution) change in the predicted number of events for each sample and each shape dependent systematics is displayed.

Table 7.9: Systematic uncertainties on ST events in the $t\bar{t}$ depleted and enriched regions. Systematic uncertainties for ZH shown in this table are obtained for $M_H = 125$ GeV. Relative uncertainties are given in percentage. As these uncertainties change the shape of the global RF distributions, the numbers are referring to average per-bin changes. If a range is given in the table, it means the uncertainty varies channel by channel and we only list the range.

Relative uncertainties (%) in the $t\bar{t}$ depleted region for ST events

Contribution	ZH	Multijet	Z+LF	$Z + b\bar{b}$	$Z + c\bar{c}$	Dibosons	$t\bar{t}$
Jet Energy Scale	0.6	–	3.1	2.3	2.3	4.8	0.3
Jet Energy Resolution	0.7	–	2.7	1.3	1.6	1.0	1.1
Jet ID	0.6	–	1.5	0.0	0.5	0.7	0.7
Jet Taggability	2.0	–	1.9	1.7	1.7	1.8	2.2
Heavy Flavor Tagging Efficiency	0.5	–	–	1.6	3.9	–	0.7
Light Flavor Tagging Efficiency	–	–	68	–	–	2.9	–
Trigger	0.4-2	–	0.03-2	0.2-2	0.2-2	0.2-2	0.5-2
Zp_T Model	–	–	1.6	1.7	1.5	–	–
Z+jets Jet Angles	–	–	1.7	1.7	1.7	–	–
Alpgen MLM	–	–	0.2	–	–	–	–
Alpgen Scale	–	–	0.3	0.5	0.5	–	–
Underlying Event	–	–	0.4	0.4	0.4	–	–

Relative uncertainties (%) in the $t\bar{t}$ enriched region for ST events

Contribution	ZH	Multijet	Z+LF	$Z + b\bar{b}$	$Z + c\bar{c}$	Dibosons	$t\bar{t}$
Jet Energy Scale	7.5	–	4.6	1.7	3.9	11	2.5
Jet Energy Resolution	0.2	–	4.5	0.7	3.1	3.9	0.7
Jet ID	1.2	–	2.1	1.0	1.2	0.9	0.7
Jet Taggability	2.1	–	7.3	2.7	3.0	2.0	3.2
Heavy Flavor Tagging Efficiency	0.5	–	–	1.3	4.8	–	0.8
Light Flavor Tagging Efficiency	–	–	73	–	–	4.1	–
Trigger	1-4	–	1-4	0.7-4	0.7-4	1-8	1-8
Zp_T Model	–	–	3.3	1.5	1.4	–	–
Z+jets Jet Angles	–	–	1.7	2.3	2.7	–	–
Alpgen MLM	–	–	0.4	–	–	–	–
Alpgen Scale	–	–	0.7	0.7	0.7	–	–
Underlying Event	–	–	0.9	1.1	1.1	–	–

Table 7.10: Systematic uncertainties on DT events in the $t\bar{t}$ depleted and enriched regions. Systematic uncertainties for ZH shown in this table are obtained for $M_H = 125$ GeV. Relative uncertainties are given in percentage. As these uncertainties change the shape of the global RF distributions, the numbers are referring to average per-bin changes. If a range is given in the table, it means the uncertainty varies channel by channel and we only list the range.

$ZH \to \ell\ell b\bar{b}$ Relative uncertainties (%) in the $t\bar{t}$ depleted region for DT events

Contribution	ZH	Multijet	Z+LF	$Z + b\bar{b}$	$Z + c\bar{c}$	Dibosons	$t\bar{t}$
Jet Energy Scale	0.5	–	4.6	3.0	1.3	4.5	1.4
Jet Energy Resolution	0.4	–	7.0	1.8	2.9	0.9	0.9
Jet ID	0.6	–	7.9	0.3	0.5	0.5	0.5
Jet Taggability	1.7	–	7.0	1.5	1.5	3.0	1.7
Heavy Flavor Tagging Efficiency	4.4	–	–	5.0	5.6	–	3.8
Light Flavor Tagging Efficiency	–	–	75	–	–	4.7	–
Trigger	0.4-2	–	0.6-6	0.3-2	0.3-3	0.4-2	0.6-5
Z_{p_T} Model	–	–	2.9	1.4	1.9	–	–
Z+jets Jet Angles	–	–	1.9	3.5	3.8	–	–
Alpgen MLM	–	–	0.2	–	–	–	–
Alpgen Scale	–	–	0.4	0.5	0.5	–	–
Underlying Event	–	–	0.5	0.4	0.4	–	–

$ZH \to \ell\ell b\bar{b}$ Relative uncertainties (%) in the $t\bar{t}$ enriched region for DT events

Contribution	ZH	Multijet	Z+LF	$Z + b\bar{b}$	$Z + c\bar{c}$	Dibosons	$t\bar{t}$
Jet Energy Scale	6.6	–	0.8	1.6	2.2	5.9	1.5
Jet Energy Resolution	1.4	–	267	1.4	2.1	4.0	0.4
Jet ID	0.9	–	0.6	0.5	3.6	2.8	0.6
Jet Taggability	2.0	–	0.9	1.6	1.9	3.1	2.1
Heavy Flavor Tagging Efficiency	4.0	–	–	5.1	6.6	–	4.2
Light Flavor Tagging Efficiency	–	–	72	–	–	–	–
Trigger	1-3	–	1-3	0.6-3	0.7-4	0.7-4	1-3
Z_{p_T} Model	–	–	1.8	1.4	1.5	–	–
Z+jets Jet Angles	–	–	1.4	3.7	2.3	–	–
Alpgen MLM	–	–	0.5	–	–	–	–
Alpgen Scale	–	–	0.8	0.5	0.4	–	–
Underlying Event	–	–	0.9	0.7	0.5	–	–

More details about the shape-related uncertainites are as follows:

- The uncertainties related to jet reconstruction. In addition to the nominal reconstruction, jets are also reconstructed using values fluctuated at $\pm 1\sigma$ for Jet Energy Scale (JES) and Jet Energy Resolution (RES) and -1σ for jet-ID efficiency to produce five systematic ntuples in addition to the nominal ntuples for each channel. The systematic ntuples are normalized using the same procedure as the nominal ntuples. The MVA trained on the nominal ntuple is then applied (without retraining) to these systematic ntuples.

- The scale factors for the joint vertex confirmation and taggability requirement are implemented through the use of event weights. Therefore the corresponding systematic uncertainties are now treated through event weights as well.

- The uncertainty of the Z/γ^*+jets jet reweighting (described in Sect. 6.4.14) is varied by 1/2 of the correction.

- Three shape dependent systematics are considered for the `Alpgen`+`Pythia` modeling of V+Jets production. The Alpgen reweighting performed to correct the M_{jj} distribution is applied at $\pm 1\sigma$ from the χ^2 fit for the best MLM matching point (**AlpMLM**). The factorization and renormalization parameters in Alpgen+Pythia are applied at one-half and twice of the nominal value (**AlpScale**). Additionally, we apply a systematic uncertainty for the underlying event model in Alpgen+Pythia [74]. The uncertainties are varied independently and applied event-by-event.

CHAPTER VIII

Limit On the Higgs Production Cross Section

As seen from the previous chapter, no excess of data over the predicted background is observed. An upper limit on the ZH production cross section times the branching ratio (of $H \to b\bar{b}$) is set. In Sect. 8.1, a modified frequentist statistical technique used in this analysis for setting the limit is described. To validate the Higgs search procedure, the cross section for the di-boson production is measured in the same final state and the result is presented in Sect. 8.2. The Higgs search result of $ZH \to \ell^+\ell^- b\bar{b}$ at DØ is presented in Sect. 8.3.

8.1 Modified frequentist method

In high energy physics, the number of occurrences of a new particle usually follows a Poisson distribution, which is the probability distribution of the number of occurrences of an event that happens rarely (small cross section and acceptance) but has very many opportunities (large integrated luminosity) to happen. The probability of observing d events in the data, given p events predicted is:

$$P(d|p) = \frac{p^d e^{-p}}{d!} = \prod_i^{Nbins} \frac{p_i^{d_i} e^{-p_i}}{d_i!} \tag{8.1}$$

The second part of Eqn. 8.1 means if multiple independent bins (for example, global RF distributions of all channels) are considered, the total probability is just the product of all probabilities from each individual bin. For the signal-plus-background hypothesis (H_{s+b}), $p_i = s_i + b_i$, where s_i and b_i denote for predicted numbers of signal events and background events, respectively. For the background-only hypothesis (H_b), $p_i = b_i$. As discussed in Sect. 7.3, the values of s_i and b_i depend on a set of parameters θ (nuisance parameters) which have non-zero uncertainties. Thus the probability of observing d events under hypothesis H could be analytically expressed as:

$$P(d|H) = \int P(d|H,\theta)d\theta = \int P(d|p(H,\theta))\pi(\theta)d\theta \tag{8.2}$$

where $\pi(\theta)$ is the probability density function for a nuisance parameter which typically has a Gaussian distribution:

$$\pi(\theta) = \prod_k \frac{1}{\sigma_k\sqrt{2\pi}} e^{-\frac{(\theta_k-\theta_k^0)^2}{2\sigma_k^2}} \tag{8.3}$$

Given number of observed data, a set of nuisance parameters that best fit to the data observation within the constraints of their uncertainties can be determined. This fit is performed by minimizing the following χ^2 function:

$$\begin{aligned} \chi^2(H,\theta) &= -2\ln(P(d|H,\theta)) = -2\ln[\prod_i^{Nbins} \frac{p_i^{d_i}e^{-p_i}}{d_i!} \prod_k \frac{1}{\sigma_k\sqrt{2\pi}} e^{-\frac{(\theta_k-\theta_k^0)^2}{2\sigma_k^2}}] \\ &\approx 2\sum_i^{Nbins} [p_i(H,\theta) - d_i - d_i\ln(\tfrac{p_i(H,\theta)}{d_i})] + \sum_k (R_k(H)^2) \end{aligned} \tag{8.4}$$

where $R_k = (\theta_k - \theta_k^0)/\sigma_k$ and an approximation $\ln(d_i!) \approx d_i ln(d_i) - d_i$ (which is valid for moderately high values) has been used. Assuming $\hat{\theta}_b$ ($\hat{\theta}_{s+b}$) is the set of nuisance parameters that minimize Eqn. 8.4 for H_b (H_{s+b}), and $\hat{p}_i(H_b)$ ($\hat{p}_i(H_{s+b})$) is the associated prediction, a test statistic – profile log-likelihood ratio (LLR) is defined

as

$$
\begin{aligned}
LLR &= -2ln(\tfrac{P(d|H_{s+b},\hat{\theta}_{s+b})}{P(d|H_b,\hat{\theta}_b)}) \\
&= \chi^2(H_{s+b},\hat{\theta}_{s+b}) - \chi^2(H_b,\hat{\theta}_b) \\
&= 2\sum_{i}^{Nbins}[\hat{p_i}(H_{s+b}) - \hat{p_i}(H_b) - d_i ln(\tfrac{\hat{p_i}(H_{s+b})}{\hat{p_i}(H_b)})] + \sum_k(\hat{R_k}(H_{s+b})^2 - \hat{R_k}(H_b)^2)
\end{aligned}
\tag{8.5}
$$

In the representation of LLR, probability density functions of H_b and H_{s+b} hypotheses could be generated numerically using large numbers of pseudo-experiments as described in the following procedure:

- randomly sample nuisance parameters from their Gaussian distributions, and obtain the expected number of signal events (s_i) and background events (b_i);
- generate pseudo-data :
  $d_i^{H_b}$: randomly sample a Poisson distribution with a mean value of $p_i(H_b) = b_i$
  $d_i^{H_{s+b}}$: randomly sample a Poisson distribution with a mean value of $p_i(H_{s+b}) = s_i + b_i$;
- obtain the H_b hypothesis LLR value of this pseudo-experiment: $\hat{p_i}(H_b)$ and $\hat{R_k}(H_b)$ are obtained by fitting b_i to $d_i^{H_b}$ (by minimizing the χ^2 function defined in Eqn. 8.4); $\hat{p_i}(H_{s+b})$ and $\hat{R_k}(H_{s+b})$ are obtained by fitting $(s_i + b_i)$ to $d_i^{H_b}$; then LLR(H_b) is calculated as Eqn. 8.5 with replacing d_i by $d_i^{H_b}$;
- the LLR(H_{s+b}) value is obtained similarly, but replacing $d_i^{H_b}$ with $d_i^{H_{s+b}}$ everywhere in the H_b case.

The observed LLR value is obtained by fitting the predict events number of H_b and H_{s+b} hypotheses to d_i^{obs}, and then replacing d_i by d_i^{obs} in Eqn. 8.5. Figure 8.1 can be referred as an example for the LLR distribution of the H_b hypothesis (blue line) and the H_{s+b} hypothesis (red line), and the observed LLR value from the data (black line). By construction, the peak of LLR(H_b) distribution is always at the positive

side, the peak of LLR(H_{s+b}) distribution is always at the negative side. Minimal overlap between LLR(H_b) and LLR(H_{s+b}) distributions indicate high sensitivity to the search for the signal process. The value of LLR_{obs} relative to LLR(H_b) and LLR(H_{s+b}) distributions indicates whether the data appears to be more signal-like or background-like.

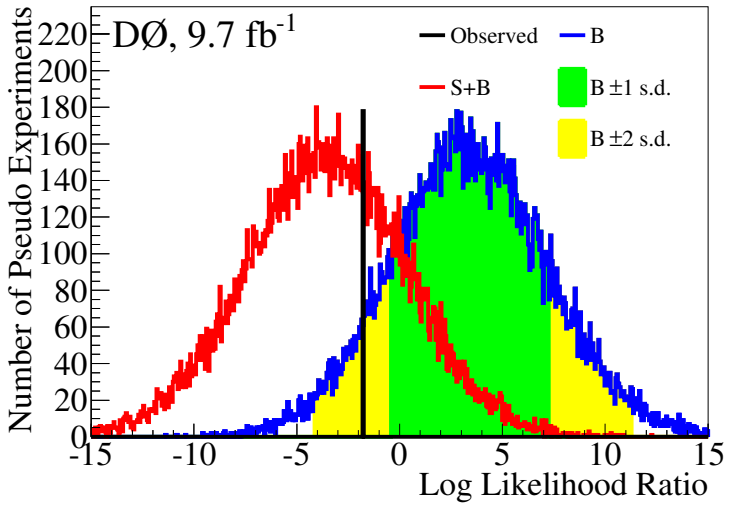

Figure 8.1: LLR distributions obtained from B (blue) and $S + B$ (red) pseudo-experiments, using the RF output as the final variable, for the VZ search. The vertical black line indicates the LLR obtained from the Run 2 data.

The confidence level of a certain hypothesis can be calculated as the probability for that hypothesis to produce an outcome more background-like than that observed in the data:

$$CL_H = P_H(LLR_H > LLR_{obs}) = \int_{LLR_{obs}}^{\infty} \frac{\partial P_H}{\partial \chi} d\chi \tag{8.6}$$

A traditional Frequentist hypothesis test relies solely on the value CL_{S+B} to evaluate exclusion limits for model parameters. However, large downward fluctuations in the data or poor background modeling can generate exclusions that may not be reproducible with larger statistics or a modified background modeling. To protect against

this pathology, a modified Frequentist statistic is defined as:

$$CL_S = \frac{CL_{S+B}}{CL_B} \tag{8.7}$$

To exclude the signal model at a level of CL_s^{exl}, it is required to have $CL_s < 1 - CL_s^{exl}$. For example the signal hypothesis is excluded at 95% confidence level if $CL_s < 5\%$.

8.1.1 Configuration of `COLLIE` package

In this analysis, the `COLLIE` (COnfidence Level LImit Evaluator) package [87] is used to perform the pseudo-experiments, construct confidence levels and evaluate exclusion limits. Some of configuration parameters for the `COLLIE` package are listed below.

The `COLLIE generateBinMap` algorithm is used to determine the binning used in the statistical analysis, starting from histograms with 1200 bins each. A target number of bins per histogram (summarized in Tab. 8.1 is set, the algorithm starts from the right of the distribution (i.e. the high S/B region) and merges bins until constraints on the signal and background content in that bin are satisfied. These constraints are summarized in Tab. 8.2. Once the constraints are satisfied, the merged bin is defined and the procedure is repeated with the remaining bins. In the first 20% of bins, no other constraints are applied. In the next 40% of the bins, the algorithm additionally requires that the signal plus background content grows linearly with the bin. Subsequently, the algorithm will choose either a linear or quadratically increasing bin content, depending on the number of events remaining.

Table 8.1: Target number of bins per b-tag sample for the `COLLIE generateBinMap` algorithm.

Region	$\mu\mu$	$\mu\mu_{\mathrm{TRK}}$	CCCC	CCEC	ee_{ICR}
$t\bar{t}$ depleted	40	20	40	40	20
$t\bar{t}$ enriched	20	10	20	20	10

Table 8.2: Constraints on signal and background bin content used by the `COLLIE` `generateBinMap` algorithm.

Value	Description
≥ 0.10	Total signal plus background yield
$\geq 10^{-4}$	Total background yield
$\leq 20\%$	Fractional statistical uncertainty on the signal plus background yield
$\leq 25\%$	Fractional statistical uncertainty on the background yield

8.2 Results for Diboson Production

To validate the search procedure, a measurement of diboson (VZ) production cross section is performed in the $\ell^+\ell^- jj$ final states. Signal events are coming from $ZZ \to \ell^+\ell^- b\bar{b}$ (or $c\bar{c}$) and $WZ \to c\bar{s}\ell^+\ell^-$ processes. The same event selection and analysis techniques (such as rewieghting to MC samples, normalization, kinematic fit, MVA and statistical analysis methods) as for the ZH search are used for this VZ cross section measurement. The diboson signal is comprised of 66% (93%) ZZ production and 34% (7%) WZ production in the ST (DT) sample. The WW process is considered to be a background. New RFs are trained to distinguish the WZ and ZZ events from other SM processes. The MC samples, RF configuration and list of input variables used for the diboson search are identical to the ones used in the ZH search. Figure 8.2 and 8.3 show the global RF and post-kinematic fit dijet mass distributions after the likelihood fit, separately for ST and DT events in the $t\bar{t}$-depleted region.

Figure 8.1 compares the LLR value observed in the data to distributions obtained from B and $S+B$ pseudo-experiments. The VZ cross section (σ_{VZ}), in units of the SM value, is obtained by maximizing L_{S+B} with respect to the nuisance parameters and a signal scale factor f, keeping the ratio of the ZZ and WZ cross sections fixed to the SM prediction. It is found that $f = 0.8 \pm 0.6$, which translates to $\sigma_{VZ} = 3.5 \pm 2.5$ pb. Figure 8.4 compares this measurement to the SM cross section, and to the distribution of results obtained from B and $S + B$ pseudo-experiments. The probability (p-value) that the B hypothesis results in a cross section greater than the measurement from

the data is 0.071, equivalent to 1.5 s.d.. The expected p-value is 0.032, corresponding to 1.9 s.d.

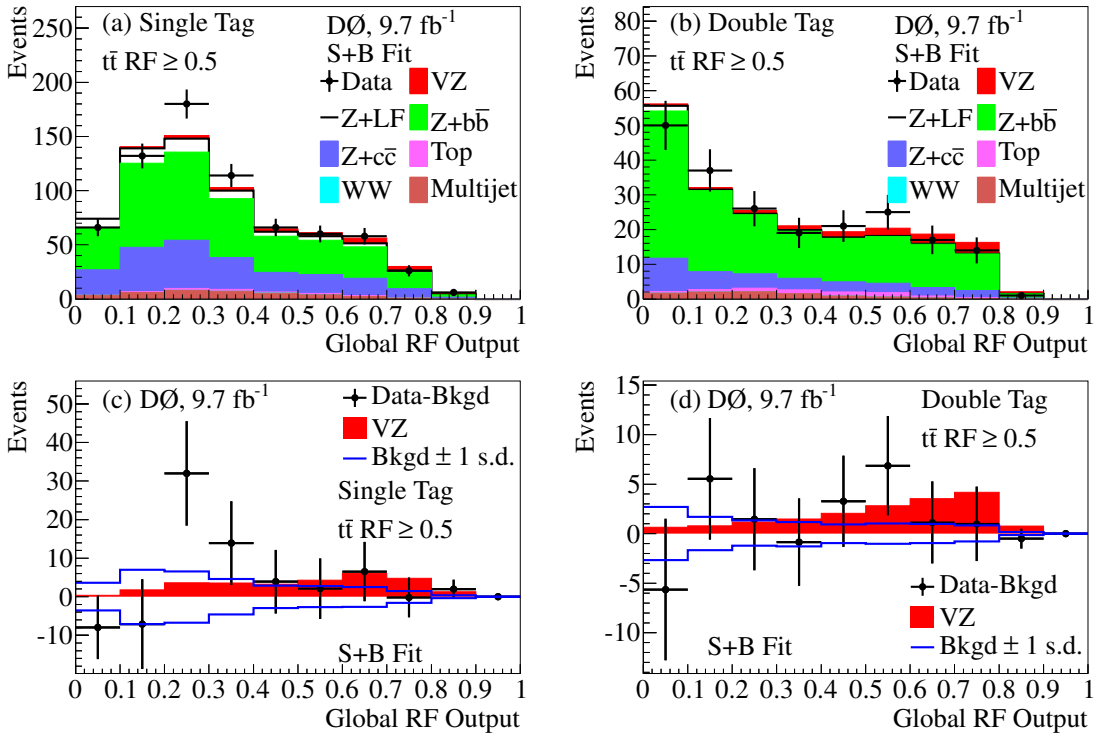

Figure 8.2: RF output distributions for the VZ search after the fit to the data in the $S+B$ hypothesis in (a) ST and (b) DT events. Distributions are summed over all four $Z \to \ell\ell$ channels. The VZ signal distribution (solid red), scaled to the measured VZ cross section, is compared to the data after subtraction of the fitted background (points) in (c) ST and (d) DT events. Also shown is the uncertainty on the background (blue lines) after the fit.

8.3 Limit on Higgs production cross section

An upper limit of the $ZH \to \ell^+\ell^- b\bar{b}$ cross section is set in units of the SM value for each Higgs mass. The histograms of the global RF output for the ST and DT samples in the $t\bar{t}$ depleted and enriched regions of each channel are the inputs to the limit setting program. For an individual lepton channel, the global RF distributions of different epochs are summed over. These give a total of 20 input channels (5 channels $\times$ 2 post-tag bins $\times$ 2 regions) to the `COLLIE` package. The use of separate channels

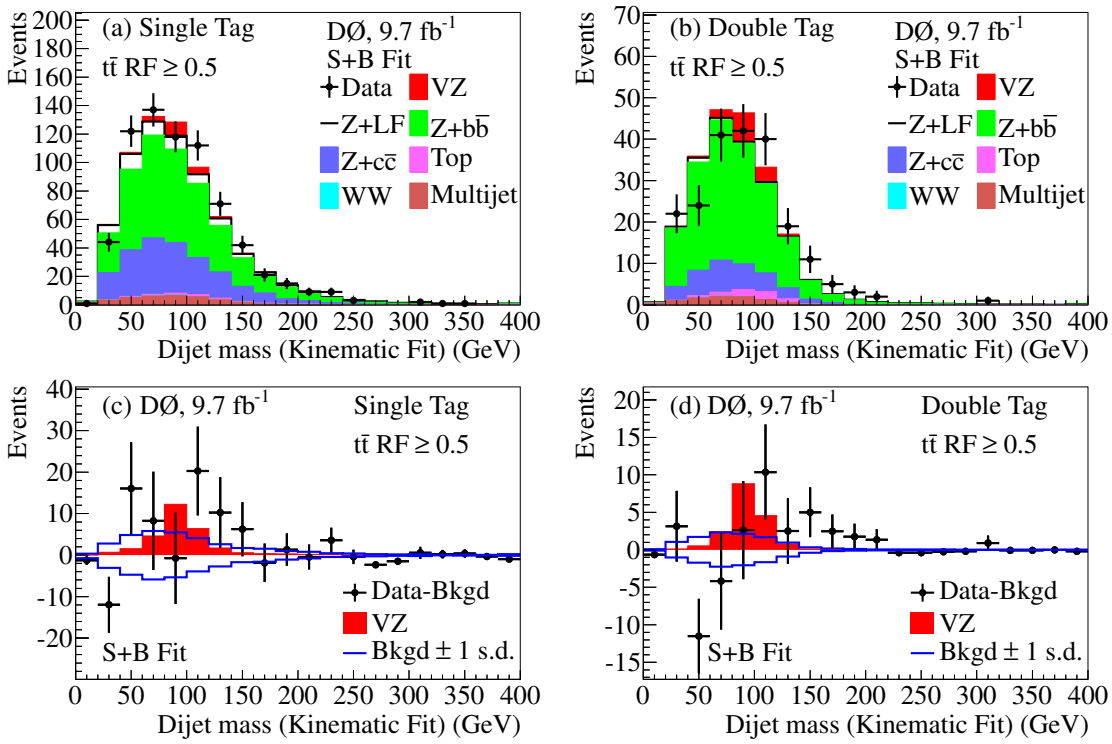

Figure 8.3: Dijet invariant mass distributions (after the kinematic fit) for the VZ search after the fit to the data in the $S+B$ hypothesis in (a) ST and (b) DT events. Distributions are summed over all four $Z \to \ell\ell$ channels. The VZ signal distribution (solid red), scaled to the measured cross section, is compared to the data after subtraction of the fitted background (points) in (c) ST and (d) DT events. Also shown is the uncertainty on the background (blue lines) after the $S+B$ fit.

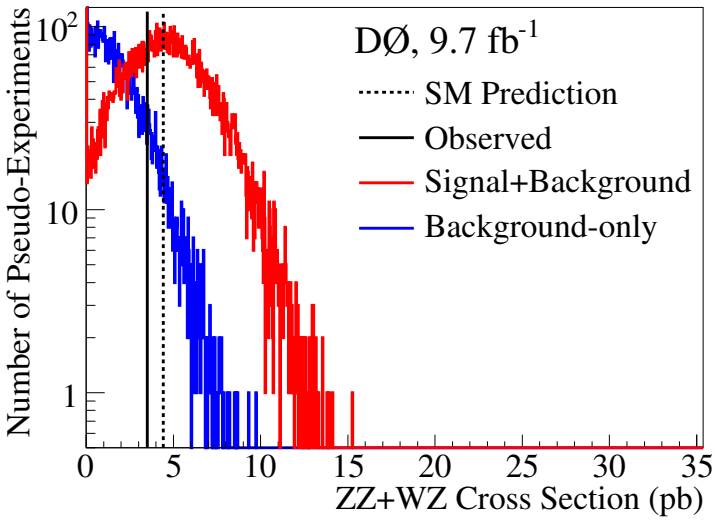

Figure 8.4: Distribution (solid histograms) of VZ cross sections obtained from B (blue) and $S+B$ (red) pseudo-experiments The observed cross section from the data (vertical solid line) and the SM cross section (vertical dotted line) are also shown.

and regions takes advantage of the sensitivity from the signal-rich subsamples and allows for a better background modeling based on the signal-poor subsamples. The limits for the $\mu\mu$ channel in shown in Tab. 8.3 and Fig. 8.5. The results from other lepton channels are listed in Appendix B. Figure 8.6 and 8.7 show the global RF distributions ($M_H = 125$ GeV) after the fit of the nuisance parameters to the data in the background-only hypothesis, summed over all lepton channels, and the data after subtraction of the background in $t\bar{t}$ depleted and enriched region. The limits for the combination of all channels are shown in Tab. 8.4. Plots of the LLR and limits are shown in Fig. 8.8. For $M_H = 125$ GeV, the observed (expected) upper limit on the ZH production cross section $\times$ branching ratio for $H\to b\bar{b}$ is 7.1 (5.1) $\times$ the SM value.

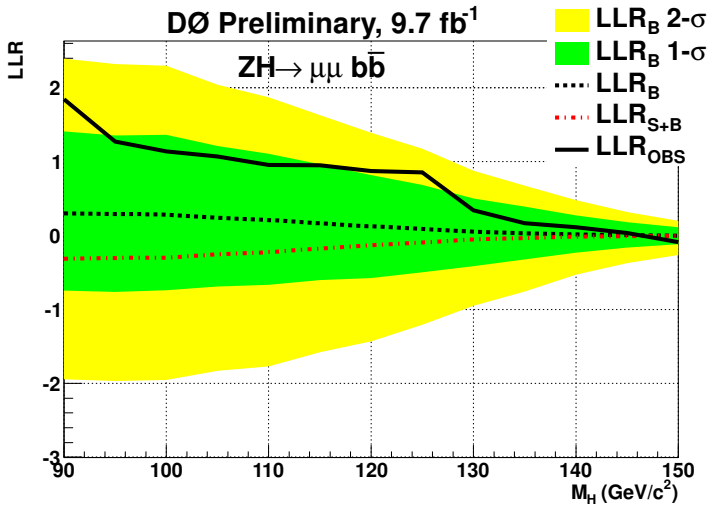

(a)

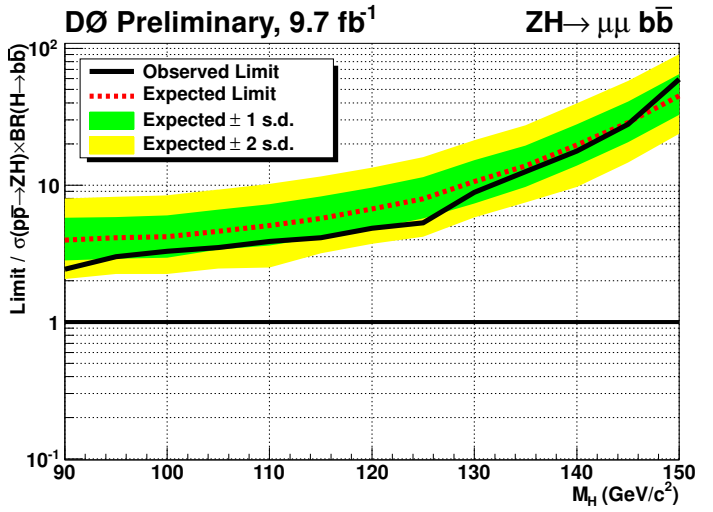

(b)

Figure 8.5: The (a) Log-Likelihood Ratio and (b) ZH production cross-section limits determined using the the CLFit2 method of the `COLLIE` package, in the $\mu\mu$ channel.

Table 8.3: The expected and observed limits on the SM Higgs production cross sections in the $\mu\mu$ channel.

M_H [GeV]	90	95	100	105	110	115	120	125	130	135	140	145	150
$\mu\mu$ Channel													
Expected	4.0	4.1	4.2	4.6	5.1	5.7	6.7	8.0	11	14	20	29	45
Observed	2.4	3.0	3.3	3.5	3.9	4.1	4.8	5.3	8.9	13	18	28	59

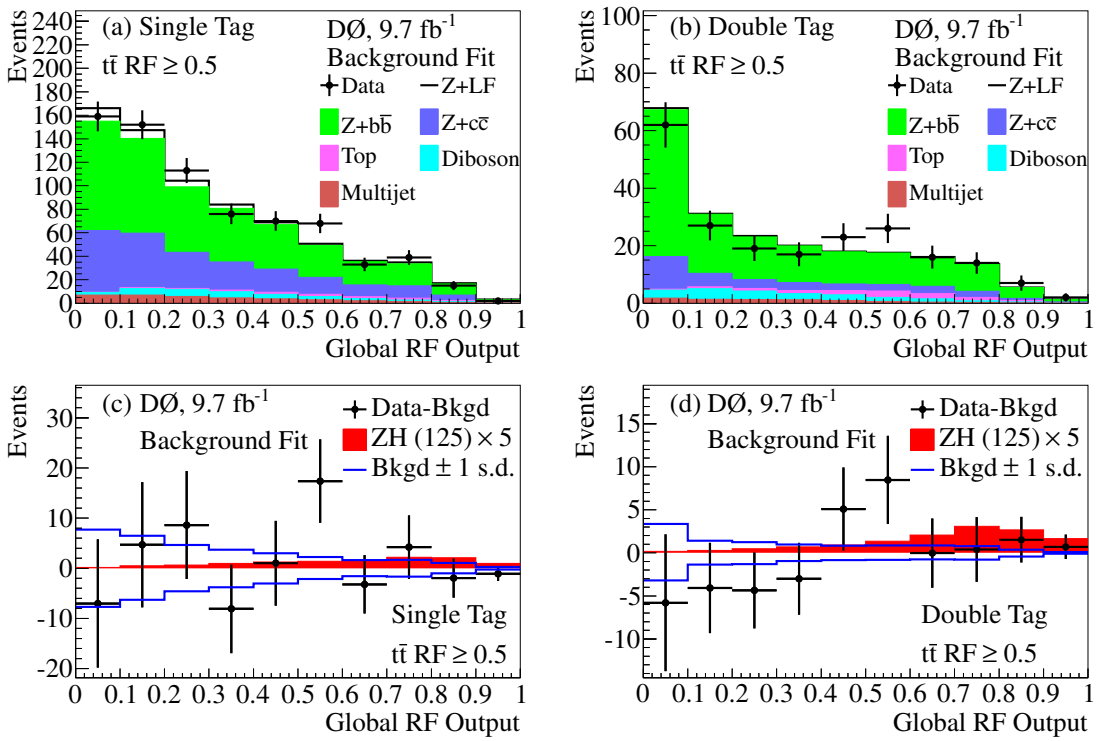

Figure 8.6: Global RF output distributions in the $t\bar{t}$-depleted region, assuming M_H = 125 GeV, after the fit to the data in the background-only hypothesis in (a) ST events and (b) DT events. Background-subtracted distributions for (a) and (b) are shown in (c) and (d), respectively. Signal distributions, for M_H = 125 GeV, are shown with the SM cross section scaled to 5 × SM prediction in (c) and (d).

Table 8.4: The expected and observed limits on the SM Higgs production cross sections in the $ZH \to \ell\ell b\bar{b}$ search.

M_H [GeV]	90	95	100	105	110	115	120	125	130	135	140	145	150
Expected	2.6	2.7	2.8	3.0	3.4	3.7	4.3	5.1	6.6	8.7	12	18	29
Observed	1.8	2.3	2.2	3.0	3.7	4.3	6.2	7.1	12	16	19	31	53

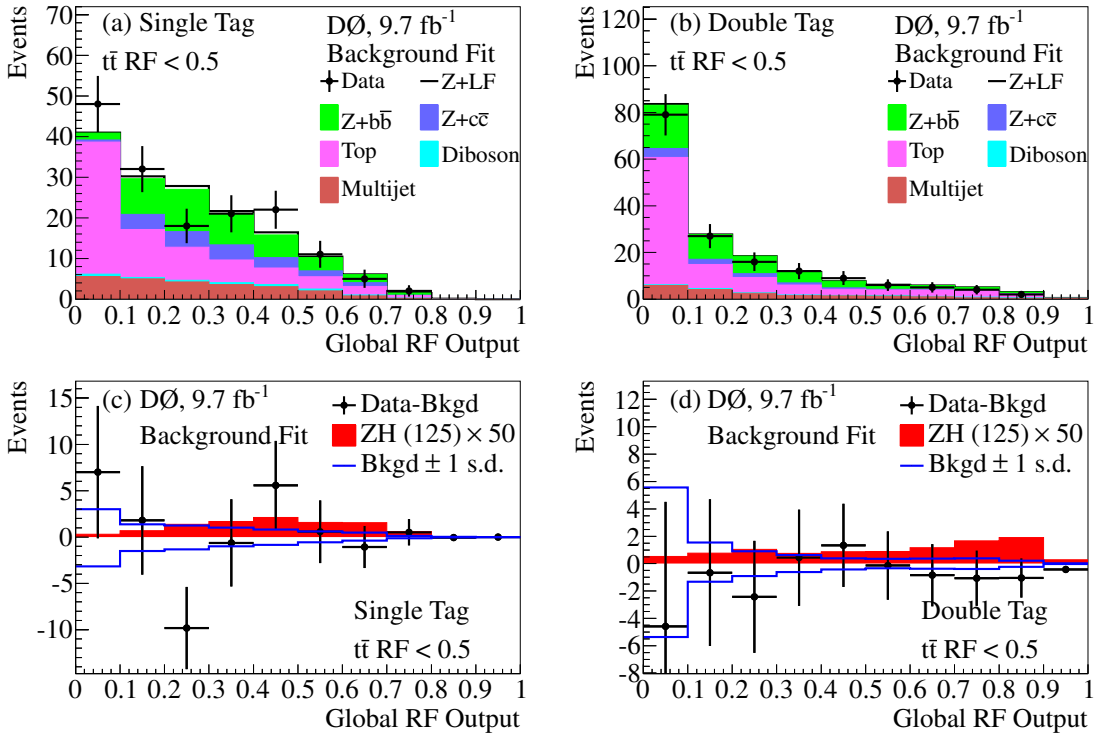

Figure 8.7: Global RF output distributions in the $t\bar{t}$-enriched region, assuming $M_H = 125$ GeV, after the fit to the data in the background-only hypothesis for (a) ST events and (b) DT events. Background-subtracted distributions for (a) and (b) are shown in (c) and (d), respectively. Signal distributions,, for $M_H = 125$ GeV, are shown with the SM cross section scaled to 50 × SM prediction in (c) and (d).

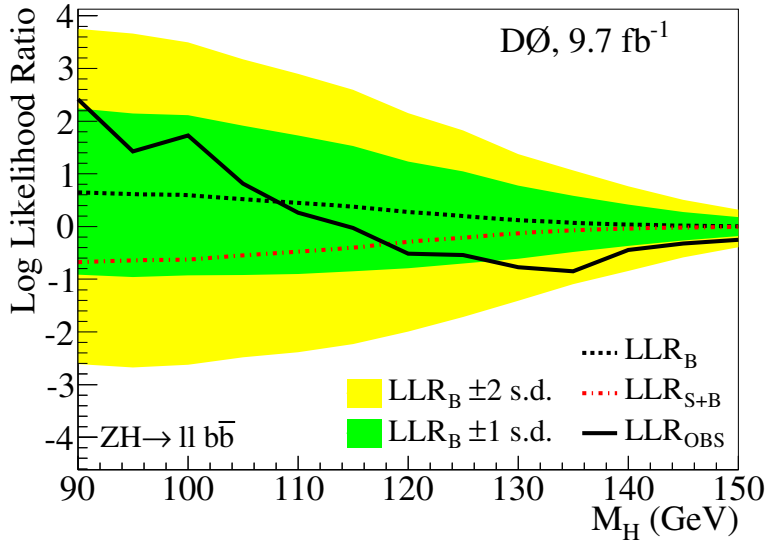

(a)

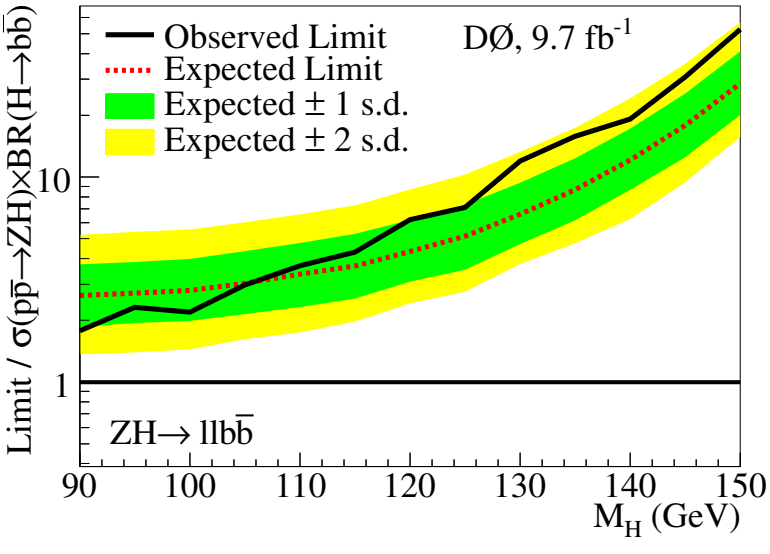

(b)

Figure 8.8: The (a) Log-Likelihood Ratio and (b) ZH production cross-section limits for all $\ell\ell bb$ channels combined, using the CLFit2 method of the `COLLIE` package.

CHAPTER IX

Evidence for $H \to b\bar{b}$ at the Tevatron

In the summer of 2013, Tevatron experiments published the final results of SM Higgs boson searches in $p\overline{p}$ collisions at $\sqrt{s} = 1.96$ TeV using the full 10 fb^{-1} Run 2 data [88]. We combined searches by the CDF and DØ collaborations for the SM Higgs boson with mass in the range 90 - 200 GeV produced in the gluon-gluon fusion, WH, ZH, $t\bar{t}H$, and vector boson fusion processes, and decaying in the $H \to b\bar{b}$, $H \to W^+W^-$, $H \to ZZ$, $H \to \tau^+\tau^-$, and $H \to \gamma\gamma$ modes. A summary of all analysis channels of DØ and CDF are shown in Tab. 9.1 and 9.2, respectively. The number of contributing channels is large, and several different kinds of discriminating variables are used. For robust comparison, we display the data from all the subchannels together, aggregating bins (of final discriminating variable of each subchannel) with similar signal-to-background ratios (s/b) from all contributing subchannels. This representation of the data is not used to compute the final results, since the distribution indiscriminately sums unrelated backgrounds which are fit separately. It does, however, provide a guide to how much individual events contribute to the results and how well the signal is separated from backgrounds in the combined search. The resulting distribution of $\log_{10}(s/b)$ is shown for $M_H = 125$ GeV in Fig. 9.1, demonstrating agreement with background over 5 orders of magnitude.

Figure. 9.2 displays the LLR distributions for the combined analyses as function of

Table 9.1: Luminosities, explored mass ranges, and references for the different processes and final states for DØ analyses. The generic labels "1×," "2×," "3×," and "4×," refer to separations based on lepton, photon, or background characterization categories. The analyses are grouped in four categories, corresponding to the Higgs boson decay mode to which the analysis is most sensitive: $H \to b\bar{b}$, $H \to W^+W^-$, $H \to \tau^+\tau^-$, and $H \to \gamma\gamma$.

Channel		Luminosity (fb^{-1})	M_H range (GeV)	Reference
$WH \to \ell\nu b\bar{b}$ 2-jet channels 2 × (4b-tag categories)	$H \to b\bar{b}$	9.7	90 - 150	[90] [91]
$WH \to \ell\nu b\bar{b}$ 3-jet channels 2 × (4b-tag categories)		9.7	90 - 150	[90] [91]
$ZH \to \nu\bar{\nu}b\bar{b}$ (2b-tag categories)		9.5	100 - 150	[89]
$ZH \to \ell^+\ell^- b\bar{b}$ 2 × (2b-tag) × (5 lepton categories)		9.7	90 - 150	[1] [2]
$H \to W^+W^- \to \ell^\pm\nu\ell^\mp\nu$ 2 × (0jets, 1jets, ≥2jets)	$H \to W^+W^-$	9.7	115 - 200	[92]
$H + X \to W^+W^- \to \mu^\pm\nu\tau^\mp_{had}\nu$ (3τ categories)		7.3	115 - 200	[93]
$H \to W^+W^- \to \ell\bar{\nu}jj$ 2 × (2b-tag categories) × (2jets, 3jets)		9.7	100 -200	[91]
$VH \to e^\pm\mu^\pm + X$		9.7	100 -200	[94]
$VH \to \ell\ell\ell + X$ ($\mu\mu e, 3 \times e\mu\mu$)		9.7	100 - 200	[94]
$VH \to \ell\bar{\nu}jjjj$ 2 × (≥4jets)		9.7	100 - 200	[91]
$VH \to \tau_{had}\tau_{had}\mu + X$ (3τ categories)	$H \to \tau^+\tau^-$	8.6	100 - 150	[94]
$H + X \to \ell^\pm\tau^\mp jj$ 2 × (3τ categories)		9.7	105 - 150	[95]
$H \to \gamma\gamma$ (4 categories)	$H \to \gamma\gamma$	9.6	100 - 150	[96]

Table 9.2: Luminosities, explored mass ranges, and references for the different processes and final states for CDF analyses. The generic labels "1×," "2×," "3×," and "4×," refer to separaions based on lepton or photon categories. The analyses are grouped in four categories, corresponding to the Higgs boson decay mode to which the analysis is most sensitive: $H \to b\bar{b}$, $H \to W^+W^-$, $H \to \tau^+\tau^-$, $H \to ZZ$, and $H \to \gamma\gamma$.

Channel		Luminosity (fb^{-1})	M_H range (GeV)	Reference
$WH \to \ell\nu b\bar{b}$ 2-jet channels 4 × (5b-tag categories)	$H \to b\bar{b}$	9.45	90 - 150	[97]
$WH \to \ell\nu b\bar{b}$ 3-jet channels 3 × (2b-tag categories)		9.45	90 - 150	[97]
$ZH \to \nu\bar{\nu}b\bar{b}$ (3b-tag categories)		9.45	90 - 150	[98]
$ZH \to \ell^+\ell^- b\bar{b}$ 2-jet channels 2 × (4b-tag categories)		9.45	90 - 150	[99]
$ZH \to \ell^+\ell^- b\bar{b}$ 3-jet channels 2 × (4b-tag categories)		9.45	90 - 150	[99]
$WH + ZH \to jjb\bar{b}$ (2b-tag categories)		9.45	100 - 150	[100]
$t\bar{t}H \to W^+bW^-\bar{b}b\bar{b}$ (4jets, 5jets, ≥6jets) × (5b-tag categories)		9.45	100 - 150	[101]
$H \to W^+W^-$ 2 × (0jets + 1jets) + ≥2jets + (low-m_{ll})	$H \to W^+W^-$	9.7	110 - 200	[102]
$H \to W^+W^-$ ($e - \tau_{had}$) + ($\mu - \tau_{had}$)		9.7	130 - 200	[102]
$WH \to WW^+W^-$ (same-sign leptons) + (trileptons)		9.7	110 - 200	[102]
$WH \to WW^+W^-$ (trileptons with 1τ_{had})		9.7	130 - 200	[102]
$ZH \to ZW^+W^-$ (trileptons with 1jet, ≥2jets)		9.7	110 - 200	[102]
$H \to \tau_{had}$ (1jet) + (≥2jets)	$H \to \tau^+\tau^-$	6.0	100 - 150	[103]
$H \to \gamma\gamma$ (0jet) + (≥1jets) + 3 × (all jets)	$H \to \gamma\gamma$	10.0	100 - 150	[104]
$H \to ZZ$ (four leptons)	$H \to ZZ$	9.7	120 - 200	[104]

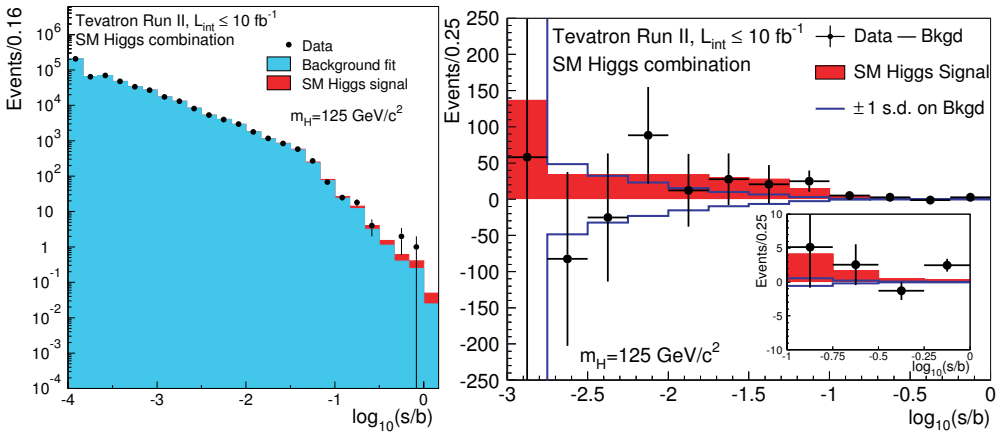

(a) (b)

Figure 9.1: Distribution of (a) $\log_{10}(s/b)$ and (b) background-subtraction, for the data from all contributing Higgs boson search channels from CDF and DØ, for M_H = 125 GeV.

M_H. The data are consistent with the background-only hypothesis at masses smaller than $\approx$ 110 GeV and above approximately 145 GeV. A slight excess is seen above approximately 195 GeV, where our ability to separate the two hypotheses is limited. For M_H from 115 to 140 GeV, an excess above 2 s.d. in the data with respect to the SM background expectation has an amplitude consistent with the expectation for a SM Higgs boson. Additionally, the LLR curve under the hypothesis that a SM Higgs boson is present with $M_H = 125$ GeV is shown. This signal-injected-LLR curve has a similar shape to the observed one.

The significance of the excess in the data over the background prediction is computed at each hypothesized Higgs boson mass by calculating the local p-value under the background-only hypothesis. The p-values express the probability to obtain the data observation or larger, assuming a signal is absent. These p-values are shown in Fig. 9.3, in which the expected p-value assuming the SM Higgs boson is present with $M_H = 125$ GeV for signal strength of 1.0 and 1.5 times the SM prediction are also shown. The median expected excess at $M_H = 125$ GeV corresponds to 1.9 s.d. assuming the SM Higgs boson is present at that mass. The observed local significance

at $M_H = 125$ GeV corresponds to 3.0 s.d.. The maximum observed local significance is at $M_H = 120$ GeV and corresponds to 3.1 s.d.. The width of the dip in the observed p-values from 115 - 140 GeV is consistent with the resolution of the combination of the $H \to b\bar{b}$ and $H \to W^+W^-$ channels, as illustrated by the injected signal curves in the same figure. Figure. 9.4 shows the best-fit value of $\sigma\times$ Branching Ratio for $M_H = 125$ GeV, for the full combination of all channels and the combinations of channels focusing on the $H \to b\bar{b}$, $H \to W^+W^-$, $H \to \tau^+\tau^-$, and $H \to \gamma\gamma$ decay modes are shown in Fig. 9.4. The combined best-fit value is $1.44^{+0.59}_{-0.56}$ times the SM predication.

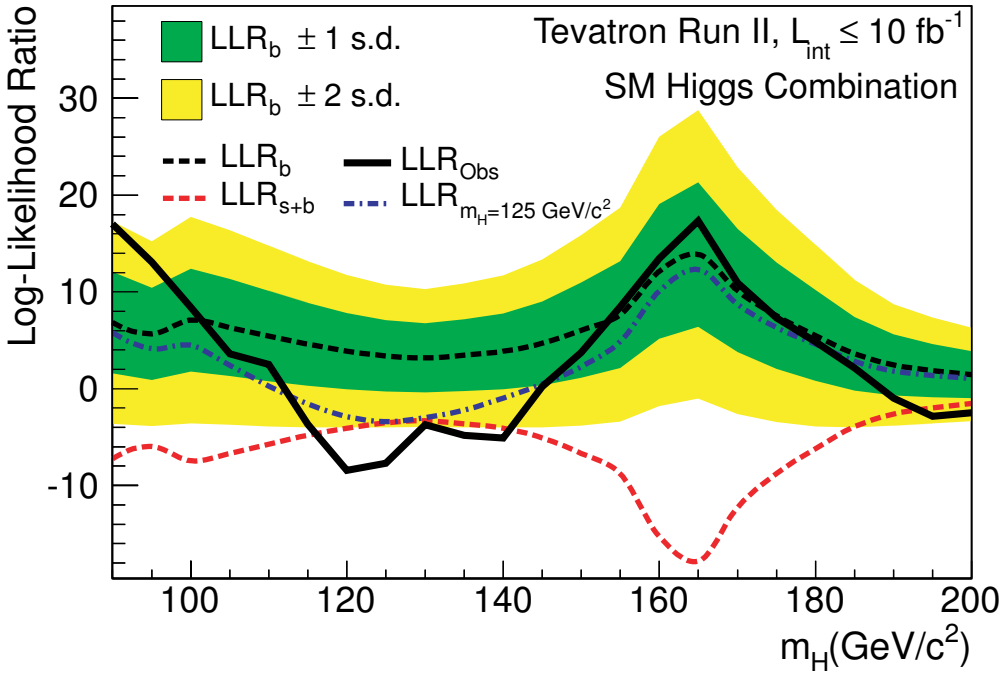

Figure 9.2: The log-likelihood ratio LLR as a function of Higgs boson mass for all of CDF and DØ's SM Higgs boson searches in all decay modes combined. The solid line shows the observed LLR values, the dark long-dashed line shows the median expectation assuming no Higgs boson signal is present, and the dark- and light-shaded bands correspond, respectively, to the regions encompassing one and two s.d. fluctuations around the background-only expectation. The red long-dashed line shows the median expectation assuming a SM Higgs boson signal is present at each value of M_H in turn. The blue short-dashed line shows the median expected LLR assuming the SM Higgs boson is present at $M_H = 125$ GeV.

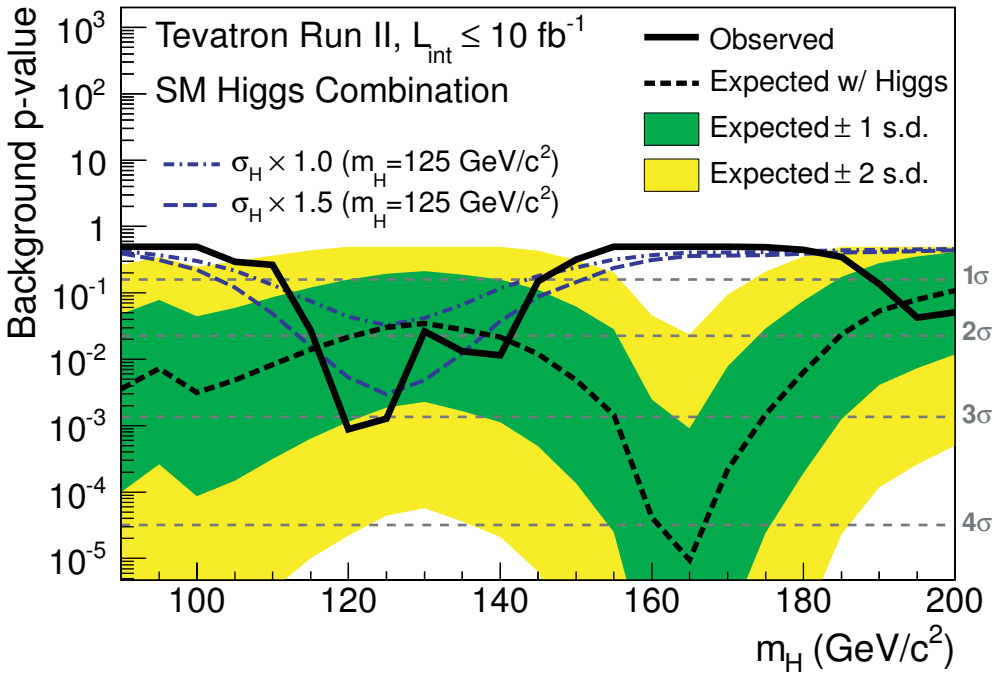

Figure 9.3: The solid black line shows the background p-value as a function of M_H for all of CDF and DØ's SM Higgs boson searches in all decay modes combined. The dotted black line shows the median expected values assuming a SM signal is present, evaluated separately at each M_H. The associated dark- and light-shaded bands indicate the one and two s.d. fluctuations of possible experimental outcomes under this scenario. The blue lines show the median expected p-values assuming the SM Higgs boson is present with $M_H = 125$ GeV at signal strengths of 1.0 times (shortdashed) and 1.5 times (long-dashed) the SM prediction.

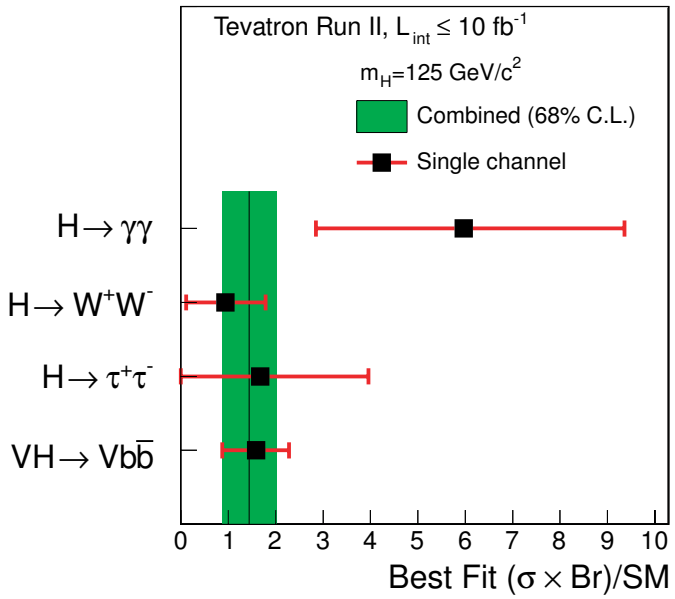

Figure 9.4: Best-fit values of $R = (\sigma \times B)/\mathrm{SM}$ using the Bayesian method for the combinations of CDF and DØ's Higgs boson search channels focusing on the $H \to b\bar{b}$, $H \to W^+W^-$, $H \to \tau^+\tau^-$, and $H \to \gamma\gamma$ decay modes for a Higgs boson mass of 125 GeV. The shaded band corresponds to the one s.d. uncertainty on the best-fit value of R for all SM Higgs boson decay modes combined.

CHAPTER X

Conclusion

In summary, we have searched for the SM Higgs production in association with a Z boson in the final state of two charged leptons (electrons or muons) and two b-quark jets using a 9.7 fb^{-1} data set of $p\bar{p}$ collisions at $\sqrt{s} = 1.96$ TeV. We employed several sophisticated techniques in this analysis, such as the kinematic fit to improve the di-jet invariant mass resolution, and a multi-steps random forest discriminant to enhance the signal-background separation. To validate the methods used in this analysis, we have measured the cross section of VZ production in the same final state, which is measured to be a factor of 0.8 ± 0.6 times the SM prediction, with a significance of 1.5 s.d. In this single channel, no significant excess over background expectation was observed in the data. We have set an upper limit on the ZH production cross section times branching ratio for different Higgs masses. The observed (expected) limit for $M_H = 125$ GeV is 7.1 (5.1) times the SM expectation.

After ten years of excellent performance for the Tevatron collider and the DØ and CDF detectors, the two collaborations combined their final results on the SM Higgs boson search. An excess of signal-like events in the low mass range $115 < M_H < 140$ GeV is observed, compatible with the experimental resolution. Its combined significance is 3.0 s.d. for $M_H = 125$ GeV, with a median expected significance of 1.9 s.d. assuming the SM Higgs boson is present at this mass. The best-fit signal

strength is $1.44^{+0.59}_{-0.56}$ times the SM expectation. This result provides the first evidence for a low mass Higgs boson decaying to its dominant decay channel ($H \to b\bar{b}$).

The ATLAS and CMS experiments announced the discovery of a new boson with a mass around 125 GeV. Strong evidence shows that the discovered boson has spin J=0 and parity P+, which is consistent with the SM prediction. The measured production cross section times branching ratio in $H \to \gamma\gamma$, $H \to ZZ^*$, $H \to WW^*$ and $H \to \tau\tau$ decay modes are consistent with the expectations for the SM Higgs boson. Due to large SM backgrounds, there are no strong evidence for the new boson decaying into the $b\bar{b}$ final state at the LHC yet.

The existence of a new resonance near 125 GeV is now established beyond reasonable doubt. There are still many open questions about this resonance: Is it the Standard Model Higgs boson? Is it the only Higgs boson and can we find its cousins? Is it fully responsible for the unitarization of the EWSB in the whole energy regime? If not, what kind of new physics can we have? All of those questions need to be answered by various precision measurements on the properties of this new boson, as well as searches for physics beyond the SM, in the coming LHC runs.

APPENDICES

APPENDIX A

Internal Consistency of the Normalization

Table A.1: Comparison of k_ϵ^i values obtained from the combined normalization fit for Run 2A data to values obtained when repeating the fit independently in each channel. Also shown are the uncertainties from the independent fit, differences in percent, and the pull (difference divided by the uncertainty).

Channel	Independent Fit	Uncertainty	Combined Fit	Discrepancy	Pull
CC-CC (Run 2a)	1.032	0.005	1.031	0.1%	0.2
CC-EC (Run 2a)	1.011	0.006	1.013	-0.2%	-0.4
ee_{ICR} (Run 2a)	1.020	0.007	1.018	0.2%	0.2
$\mu\mu$ (Run 2a)	0.925	0.003	0.925	-0.0%	-0.0
$\mu\mu_{\mathrm{TRK}}$ (Run 2a)	0.907	0.009	0.907	-0.1%	-0.1

Table A.2: Comparison of α^{i0} values obtained from the combined normalization fit for Run 2A data to values obtained when repeating the fit independently in each channel. Also shown are the uncertainties from the independent fit, differences in percent, and the pull (difference divided by the uncertainty).

Channel	Independent Fit	Uncertainty	Combined Fit	Discrepancy	Pull
CC-CC (Run 2a)	0.342	0.011	0.343	-0.2%	-0.1
CC-EC (Run 2a)	0.331	0.006	0.331	0.2%	0.1
ee_{ICR} (Run 2a)	0.116	0.010	0.117	-0.8%	-0.1
$\mu\mu$ (Run 2a)	1.434	0.113	1.433	0.1%	0.0

Table A.3: Comparison of α^{i1} values obtained from the combined normalization fit for Run 2A data to values obtained when repeating the fit independently in each channel. Also shown are the uncertainties from the independent fit, differences in percent, and the pull (difference divided by the uncertainty).

Channel	Independent Fit	Uncertainty	Combined Fit	Discrepancy	Pull
CC-CC (Run 2a)	0.302	0.028	0.293	3.1%	0.3
CC-EC (Run 2a)	0.262	0.011	0.266	-1.4%	-0.3
ee_{ICR} (Run 2a)	0.073	0.019	0.068	7.3%	0.3
$\mu\mu$ (Run 2a)	0.458	0.030	0.462	-0.9%	-0.1

Table A.4: Comparison of α^{i2} values obtained from the combined normalization fit for Run 2A data to values obtained when repeating the fit independently in each channel. Also shown are the uncertainties from the independent fit, differences in percent, and the pull (difference divided by the uncertainty).

Channel	Independent Fit	Uncertainty	Combined Fit	Discrepancy	Pull
CC-CC (Run 2a)	0.123	0.063	0.144	-17.0%	-0.3
CC-EC (Run 2a)	0.282	0.027	0.289	-2.5%	-0.3
ee_{ICR} (Run 2a)	0.013	0.035	0.012	6.9%	0.0
$\mu\mu$ (Run 2a)	0.454	0.047	0.438	3.5%	0.3

Table A.5: Comparison of k_Z^1 values obtained from the combined normalization fit for Run 2A data to values obtained when repeating the fit independently in each channel. Also shown are the uncertainties from the independent fit, differences in percent, and the pull (difference divided by the uncertainty).

	Value	Uncertainty	Discrepancy	Pull
Combined	0.970	0.007		
CC-CC (Run 2a)	0.954	0.016	-1.8%	-1.1
CC-EC (Run 2a)	0.990	0.020	2.0%	1.0
ee_{ICR} (Run 2a)	0.954	0.022	-1.7%	-0.7
$\mu\mu$ (Run 2a)	0.975	0.010	0.4%	0.4
$\mu\mu_{\mathrm{TRK}}$ (Run 2a)	0.977	0.029	0.7%	0.2

Table A.6: Comparison of k_Z^2 values obtained from the combined normalization fit for Run 2A data to values obtained when repeating the fit independently in each channel. Also shown are the uncertainties from the independent fit, differences in percent, and the pull (difference divided by the uncertainty).

	Value	Uncertainty	Discrepancy	Pull
Combined	1.057	0.020		
CC-CC (Run 2a)	1.099	0.046	3.8%	0.9
CC-EC (Run 2a)	1.105	0.059	4.4%	0.8
ee_{ICR} (Run 2a)	1.052	0.064	-0.5%	-0.1
$\mu\mu$ (Run 2a)	1.032	0.027	-2.4%	-0.9
$\mu\mu_{\mathrm{TRK}}$ (Run 2a)	1.058	0.082	0.1%	0.0

Table A.7: Comparison of k_ϵ^i values obtained from the combined normalization fit for Run 2B data to values obtained when repeating the fit independently in each channel. Also shown are the uncertainties from the independent fit, differences in percent, and the pull (difference divided by the uncertainty).

Channel	Independent Fit	Uncertainty	Combined Fit	Discrepancy	Pull
CC-CC (Run 2b1)	0.989	0.005	0.989	-0.0%	-0.0
CC-CC (Run 2b2)	1.015	0.004	1.015	0.0%	0.1
CC-CC (Run 2b3-4)	1.045	0.003	1.044	0.1%	0.3
CC-EC (Run 2b1)	0.970	0.005	0.973	-0.4%	-0.7
CC-EC (Run 2b2)	1.005	0.004	1.008	-0.3%	-0.9
CC-EC (Run 2b3-4)	1.042	0.003	1.040	0.2%	0.6
ee_{ICR} (Run 2b1)	0.966	0.007	0.968	-0.3%	-0.4
ee_{ICR} (Run 2b2)	0.913	0.004	0.918	-0.6%	-1.2
ee_{ICR} (Run 2b3-4)	1.012	0.004	1.013	-0.1%	-0.2
$\mu\mu$ (Run 2b1)	0.966	0.004	0.968	-0.2%	-0.6
$\mu\mu$ (Run 2b2)	0.982	0.003	0.982	-0.0%	-0.1
$\mu\mu$ (Run 2b3-4)	0.991	0.002	0.990	0.1%	0.5
$\mu\mu_{\mathrm{TRK}}$ (Run 2b1)	1.046	0.011	1.037	0.9%	0.9
$\mu\mu_{\mathrm{TRK}}$ (Run 2b2)	1.042	0.007	1.034	0.8%	1.1
$\mu\mu_{\mathrm{TRK}}$ (Run 2b3-4)	1.017	0.006	1.013	0.4%	0.7

Table A.8: Comparison of α^{i0} values obtained from the combined normalization fit for Run 2B data to values obtained when repeating the fit independently in each channel. Also shown are the uncertainties from the independent fit, differences in percent, and the pull (difference divided by the uncertainty).

Channel	Independent Fit	Uncertainty	Combined Fit	Discrepancy	Pull
CC-CC (Run 2b1)	0.179	0.005	0.179	0.0%	0.0
CC-CC (Run 2b2)	0.098	0.002	0.099	-0.0%	-0.0
CC-CC (Run 2b3-4)	0.131	0.001	0.131	-0.1%	-0.1
CC-EC (Run 2b1)	0.168	0.003	0.168	0.3%	0.2
CC-EC (Run 2b2)	0.095	0.001	0.095	0.2%	0.3
CC-EC (Run 2b3-4)	0.115	0.001	0.116	-0.1%	-0.2
ee_{ICR} (Run 2b1)	0.109	0.005	0.108	0.7%	0.1
ee_{ICR} (Run 2b2)	0.078	0.003	0.077	1.8%	0.4
ee_{ICR} (Run 2b3-4)	0.080	0.003	0.080	0.4%	0.1
$\mu\mu$ (Run 2b1)	1.465	0.153	1.431	2.3%	0.2
$\mu\mu$ (Run 2b2)	1.545	0.102	1.541	0.2%	0.0
$\mu\mu$ (Run 2b3-4)	1.177	0.082	1.193	-1.3%	-0.2

Table A.9: Comparison of α^{i1} values obtained from the combined normalization fit for Run 2B data to values obtained when repeating the fit independently in each channel. Also shown are the uncertainties from the independent fit, differences in percent, and the pull (difference divided by the uncertainty).

Channel	Independent Fit	Uncertainty	Combined Fit	Discrepancy	Pull
CC-CC (Run 2b1)	0.128	0.013	0.129	-0.7%	-0.1
CC-CC (Run 2b2)	0.114	0.005	0.114	0.3%	0.1
CC-CC (Run 2b3-4)	0.123	0.004	0.122	0.9%	0.3
CC-EC (Run 2b1)	0.144	0.005	0.147	-2.3%	-0.6
CC-EC (Run 2b2)	0.109	0.002	0.111	-1.9%	-0.8
CC-EC (Run 2b3-4)	0.113	0.002	0.112	1.1%	0.6
ee_{ICR} (Run 2b1)	0.075	0.009	0.079	-5.7%	-0.5
ee_{ICR} (Run 2b2)	0.057	0.006	0.065	-13.1%	-1.4
ee_{ICR} (Run 2b3-4)	0.071	0.005	0.071	0.4%	0.1
$\mu\mu$ (Run 2b1)	0.410	0.037	0.438	-6.8%	-0.8
$\mu\mu$ (Run 2b2)	0.403	0.023	0.409	-1.4%	-0.3
$\mu\mu$ (Run 2b3-4)	0.449	0.020	0.440	2.0%	0.5

Table A.10: Comparison of α^{i2} values obtained from the combined normalization fit for Run 2B data to values obtained when repeating the fit independently in each channel. Also shown are the uncertainties from the independent fit, differences in percent, and the pull (difference divided by the uncertainty).

Channel	Independent Fit	Uncertainty	Combined Fit	Discrepancy	Pull
CC-CC (Run 2b1)	0.147	0.032	0.144	1.9%	0.1
CC-CC (Run 2b2)	0.139	0.005	0.139	0.1%	0.0
CC-CC (Run 2b3-4)	0.132	0.012	0.133	-0.8%	-0.1
CC-EC (Run 2b1)	0.143	0.015	0.152	-6.7%	-0.6
CC-EC (Run 2b2)	0.134	0.008	0.137	-2.2%	-0.4
CC-EC (Run 2b3-4)	0.112	0.005	0.111	0.5%	0.1
ee_{ICR} (Run 2b1)	0.098	0.024	0.099	-1.7%	-0.1
ee_{ICR} (Run 2b2)	0.055	0.013	0.061	-10.6%	-0.5
ee_{ICR} (Run 2b3-4)	0.049	0.011	0.061	-25.2%	-1.2
$\mu\mu$ (Run 2b1)	0.335	0.049	0.309	7.8%	0.5
$\mu\mu$ (Run 2b2)	0.427	0.035	0.409	4.0%	0.5
$\mu\mu$ (Run 2b3-4)	0.348	0.025	0.351	-0.9%	-0.1

Table A.11: Comparison of k_Z^1 values obtained from the combined normalization fit for Run 2B data to values obtained when repeating the fit independently in each channel. Also shown are the uncertainties from the independent fit, differences in percent, and the pull (difference divided by the uncertainty).

	Value	Uncertainty	Discrepancy	Pull
Combined	0.895	0.003		
CC-CC (Run 2b1)	0.899	0.015	0.4%	0.2
CC-CC (Run 2b2)	0.893	0.010	-0.2%	-0.2
CC-CC (Run 2b3-4)	0.887	0.008	-0.9%	-1.1
CC-EC (Run 2b1)	0.930	0.018	3.8%	1.9
CC-EC (Run 2b2)	0.927	0.012	3.4%	2.6
CC-EC (Run 2b3-4)	0.876	0.010	-2.2%	-2.0
ee_{ICR} (Run 2b1)	0.921	0.022	2.8%	1.2
ee_{ICR} (Run 2b2)	0.946	0.014	5.4%	3.5
ee_{ICR} (Run 2b3-4)	0.895	0.011	-0.1%	-0.1
$\mu\mu$ (Run 2b1)	0.919	0.010	2.6%	2.4
$\mu\mu$ (Run 2b2)	0.900	0.006	0.5%	0.8
$\mu\mu$ (Run 2b3-4)	0.888	0.005	-0.9%	-1.5
$\mu\mu_{\mathrm{TRK}}$ (Run 2b1)	0.842	0.027	-6.3%	-2.0
$\mu\mu_{\mathrm{TRK}}$ (Run 2b2)	0.845	0.017	-6.0%	-2.9
$\mu\mu_{\mathrm{TRK}}$ (Run 2b3-4)	0.870	0.014	-3.0%	-1.8

Table A.12: Comparison of k_Z^2 values obtained from the combined normalization fit for Run 2B data to values obtained when repeating the fit independently in each channel. Also shown are the uncertainties from the independent fit, differences in percent, and the pull (difference divided by the uncertainty).

	Value	Uncertainty	Discrepancy	Pull
Combined	0.935	0.007		
CC-CC (Run 2b1)	0.924	0.040	-1.2%	-0.3
CC-CC (Run 2b2)	0.934	0.025	-0.1%	-0.1
CC-CC (Run 2b3-4)	0.941	0.022	0.6%	0.2
CC-EC (Run 2b1)	1.036	0.055	9.7%	1.8
CC-EC (Run 2b2)	0.978	0.035	4.3%	1.2
CC-EC (Run 2b3-4)	0.924	0.028	-1.2%	-0.4
ee_{ICR} (Run 2b1)	0.947	0.062	1.3%	0.2
ee_{ICR} (Run 2b2)	0.984	0.041	5.0%	1.2
ee_{ICR} (Run 2b3-4)	1.021	0.033	8.4%	2.6
$\mu\mu$ (Run 2b1)	0.900	0.024	-3.9%	-1.5
$\mu\mu$ (Run 2b2)	0.914	0.016	-2.3%	-1.3
$\mu\mu$ (Run 2b3-4)	0.939	0.013	0.4%	0.3
$\mu\mu_{\mathrm{TRK}}$ (Run 2b1)	0.847	0.065	-10.5%	-1.4
$\mu\mu_{\mathrm{TRK}}$ (Run 2b2)	0.904	0.046	-3.5%	-0.7
$\mu\mu_{\mathrm{TRK}}$ (Run 2b3-4)	0.920	0.036	-1.7%	-0.4

APPENDIX B

Other lepton channels in $ZH \rightarrow \ell^+\ell^- b\bar{b}$ analysis

In $ZH \rightarrow \ell^+\ell^- b\bar{b}$ analysis, there are four leptons channels in total – ee, $ee_{\rm ICR}$, $\mu\mu$ and $\mu\mu_{\rm TRK}$ subchannels. The $\mu\mu$ channel analysis has been described in main body of this thesis. This appendix will only give a berief description of other three lepton channels and results from those channels.

The $\mu\mu_{\rm TRK}$ channel is designed to recover dimuon events in which one muon is not identified in the muon system, primarily because of gaps in the muon system coverage. In this channel we require the presence of exactly one muon with $|\eta_{det}| < 1.5$ and $p_T > 15$ GeV that must satisfy the same isolation requirements used for the $\mu\mu$ channel. We also require the presence of an isolated track with $|\eta_{det}| < 2$ and $p_T > 20$ GeV, and separated from the muon by $dR > 0.1$. This track-only muon must have at least one SMT hit, $d_{PV} < 0.02$ cm, and $d^z_{PV} < 1$ cm. It must also satisfy the same tracker and calorimeter isolation requirements as the muon. It must be separated from all jets with with $p_T > 15$ GeV and $|\eta_{det}| < 2.5$ by $dR > 0.5$. To ensure that the $\mu\mu$ and $\mu\mu_{\rm TRK}$ selections do not overlap, we reject events that contain any additional muons with $|\eta_{det}| < 2$ and $p_T > 10$ GeV. For the very small fraction of events with more than one track passing these requirements, the track whose invariant mass with the muon is closest to the Z boson mass (91.2 GeV) is

chosen.

In the ee channel, we select events with at least two electrons with $p_T > 15$ GeV that pass selection requirements based on the energy deposition and shower shape in the calorimeter and the CPS. Electrons are acccepted in the CC with $|\eta_{det}| < 1.1$ and in the EC with $1.5 < |\eta_{det}| < 2.5$, but at least one of the electrons must be identified in the CC. Electrons are selected from EM clusters reconstructed within a cone of radius $\mathcal{R} = 0.2$ and satisfying the following requirements: (i) at least 90% (97%) of the cluster energy is deposited in the EM calorimeter of the CC (EC); (ii) the calorimeter isolation variable $I = [E_{tot}(0.4) - E_{EM}(0.2)]/E_{EM}(0.2)$ is less than 0.09 (0.05) in the CC (EC), where $E_{tot}(0.4)$ is the total energy in a cone of radius $\mathcal{R} = 0.4$ and $E_{EM}(0.2)$ is the EM energy in a cone of radius $\mathcal{R} = 0.2$; (iii) the scalar sum of the transverse momenta of all tracks in an hollow cone of $0.05 < \Delta\mathcal{R} < 0.4$ around the electron is less than 4 GeV in the CC, and less than a cutoff between 0.01 and 2 GeV in the EC, depending on the η_{det} of the electron; (iv) the output of an artificial neural network – which combines the energy deposition in the first EM layer, track isolation, and energy deposition in the CPS – is consistent with that expected from an electron; (v) CC electrons must match central tracks or a set of hits in the tracker consistent with that of an electron trajectory; (vi) for EC electrons the energy-weighted cluster width in the third EM layer must be consistent with that expected from an EM shower.

In the $ee_{\rm ICR}$ channel, events must contain exactly one electron in either the CC or EC with $p_T > 15$ GeV, and an "ICR track" pointing toward one of the ICRs, where electromagnetic object identification is compromised. The ICR track must be matched to a calorimeter energy deposit with $E_{\rm T} > 15$ GeV. Electrons going into the ICR are reconstructed as taus in the offline software. The ICR electron must therefore satisfy a requirement on the output of a neural net, designed to separate taus from jets, that combines the track quality, the track isolation and the energy deposition

in the plastic scintillator detectors located in the ICR. When the electron is found in the EC, we require that the ICR electron is in the adjoining ICR. In both the ee and the ee_{ICR} channels, any tracks matched to electrons must have $d_{PV}^{z} < 1$ cm.

For ee and $\mu\mu_{\mathrm{TRK}}$ channels, no explicit trigger is required; for the ee_{ICR} channel, an `EJets_OR` trigger is required to achieve good background modeling.

The results extracted from those three individual channels are shown in Tab. B.1 and Fig. B.1 - B.3.

Table B.1: The expected and observed limits on the Standard Model Higgs production cross sections in the $\mu\mu_{\mathrm{TRK}}$, ee, and ee_{ICR} channels.

M_H [GeV]	90	95	100	105	110	115	120	125	130	135	140	145	150
ee Channel													
Expected	4.1	4.2	4.6	4.9	5.3	5.8	7.1	8.4	10	14	19	28	46
Observed	4.3	4.7	4.4	6.0	9.4	8.0	11	12	18	23	28	42	74
ee_{ICR} Channel													
Expected	11	12	12	13	15	17	19	23	29	40	55	82	141
Observed	7.7	11	10	13	23	26	37	44	64	91	103	164	219
$\mu\mu_{\mathrm{TRK}}$ Channel													
Expected	11	14	14	16	19	23	26	30	39	53	71	106	171
Observed	14	17	15	27	23	30	43	48	61	75	96	164	237

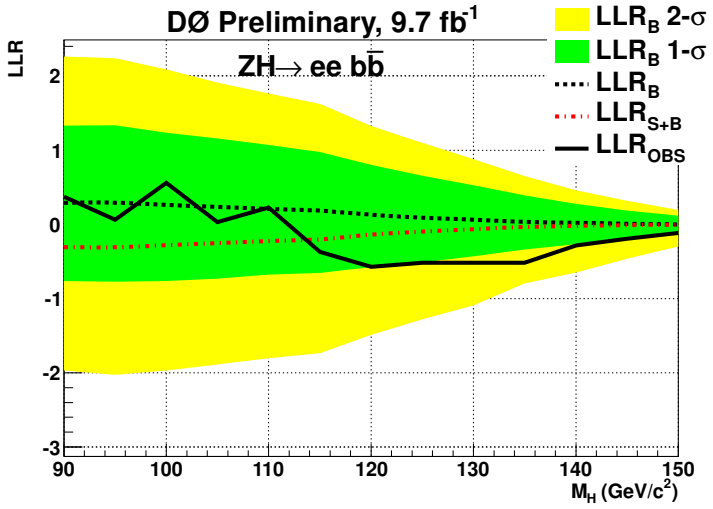

(a)

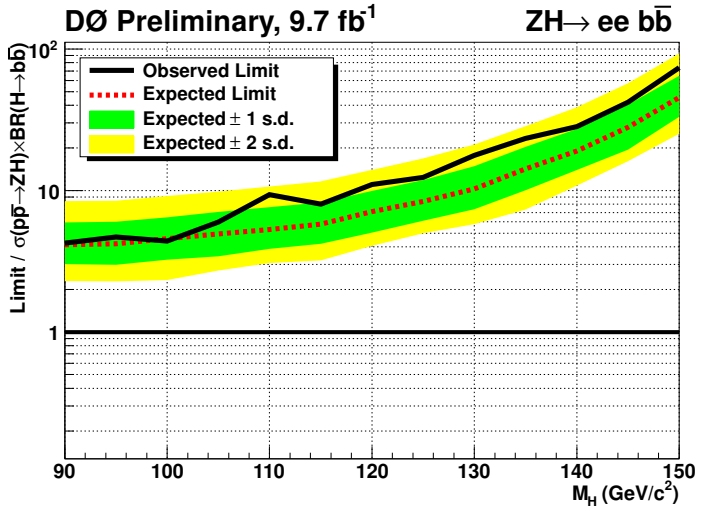

(b)

Figure B.1: The (a) Log-Likelihood Ratio and (b) ZH production cross-section limits determined using the the CLFit2 method of the `COLLIE` package, in the ee channel.

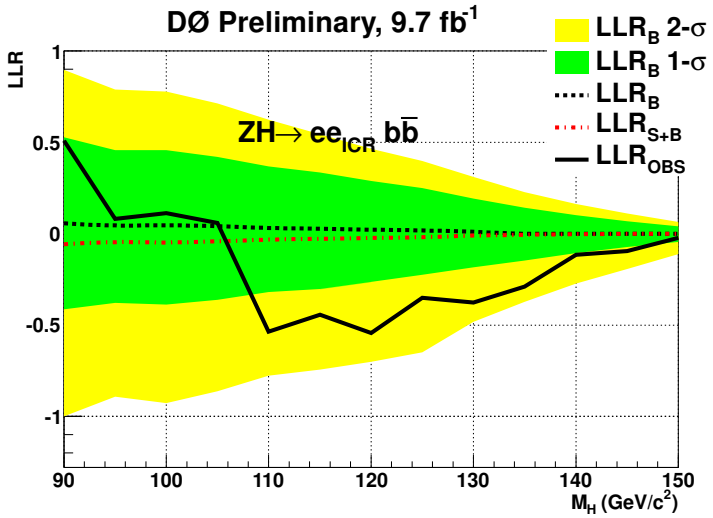

(a)

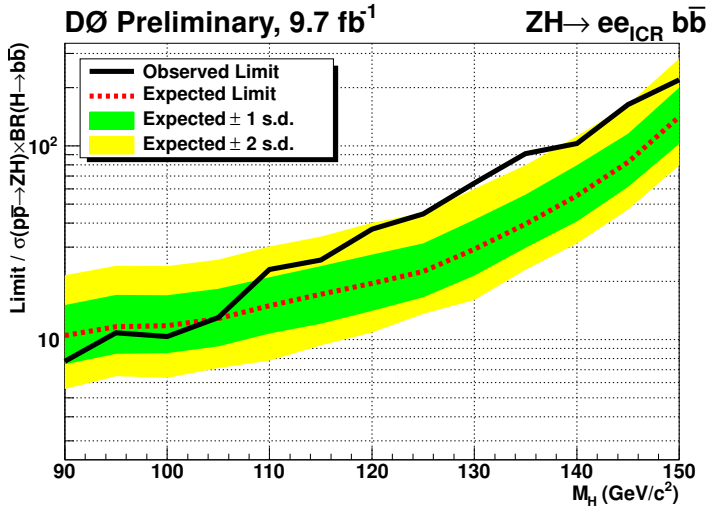

(b)

Figure B.2: The (a) Log-Likelihood Ratio and (b) ZH production cross-section limits determined using the the CLFit2 method of the `COLLIE` package, in the ee_{ICR} channel.

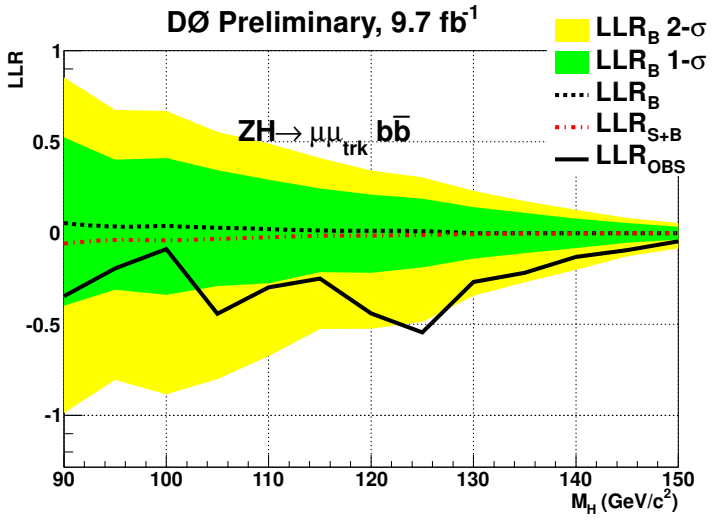

(a)

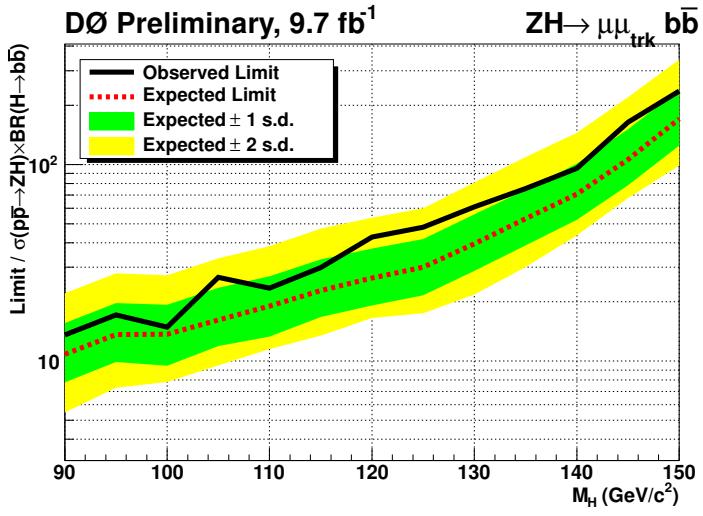

(b)

Figure B.3: The (a) Log-Likelihood Ratio and (b) ZH production cross-section limits determined using the the CLFit2 method of the `COLLIE` package, in the $\mu\mu_{\rm TRK}$ channel.

APPENDIX C

Control plots

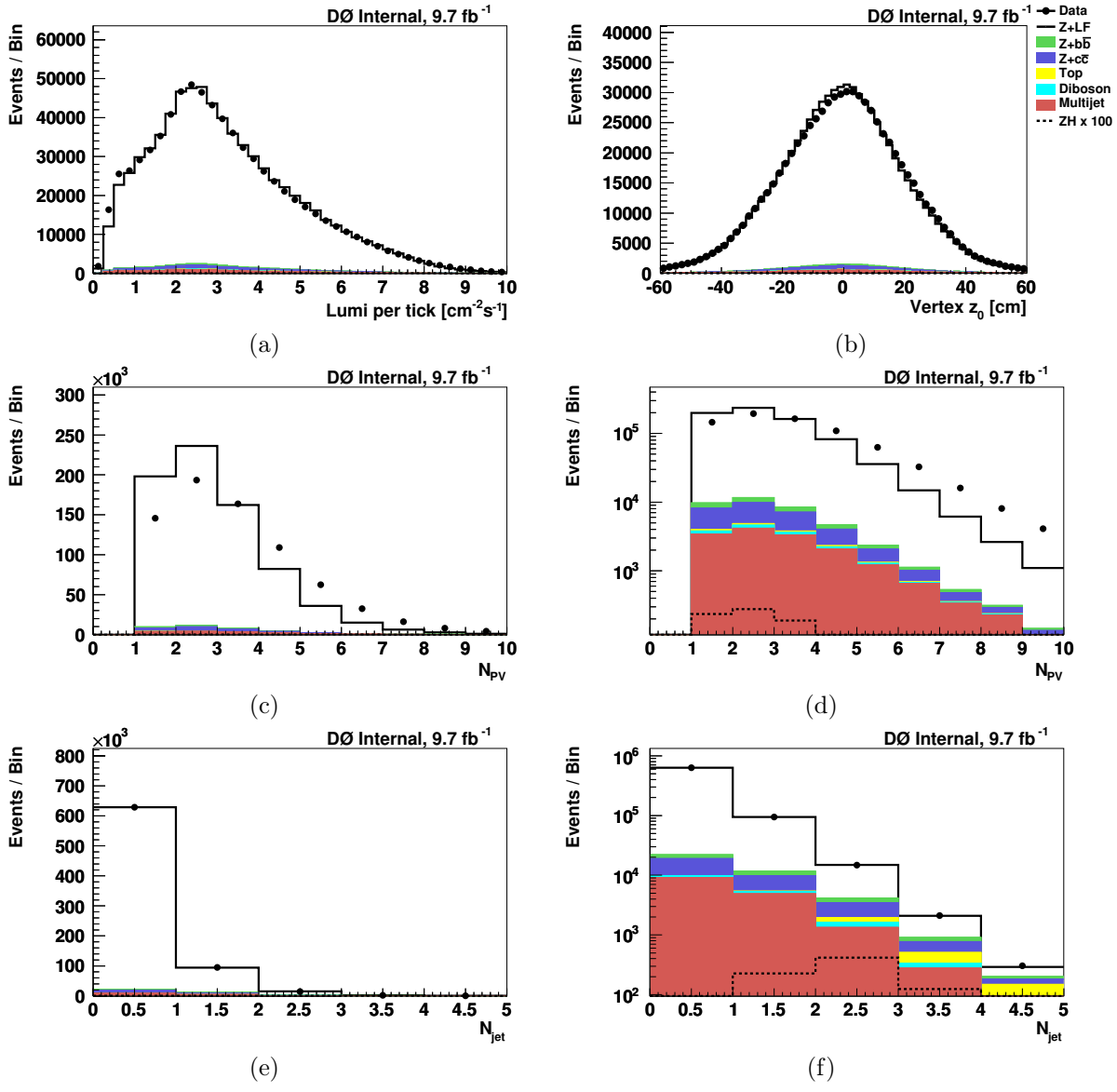

Figure C.1: $\mu\mu$ sample with leptonic preselection but no jet requirements: (a) instantaneous luminosity, (b) primary vertex z, (c) number of primary vertices, (d) log, (e) number of jets, and (f) log.

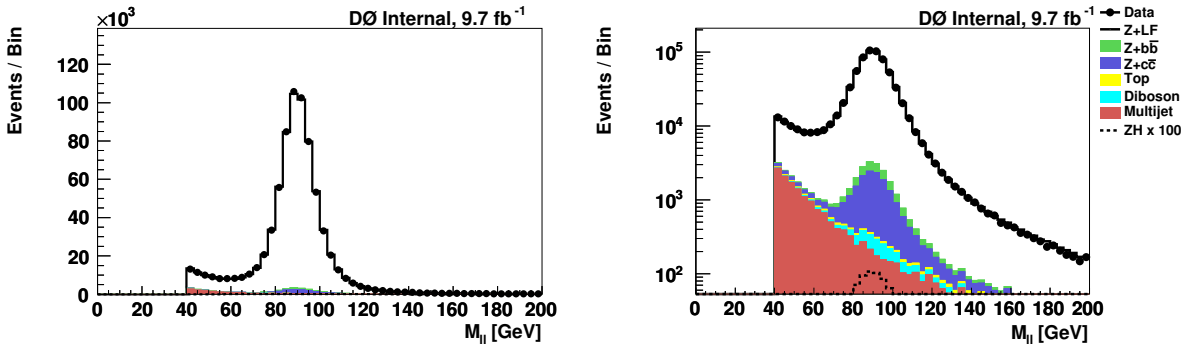

(a) (b)

Figure C.2: $\mu\mu$ sample with leptonic preselection but no jet requirements: (a) dilepton invariant mass and (b) log.

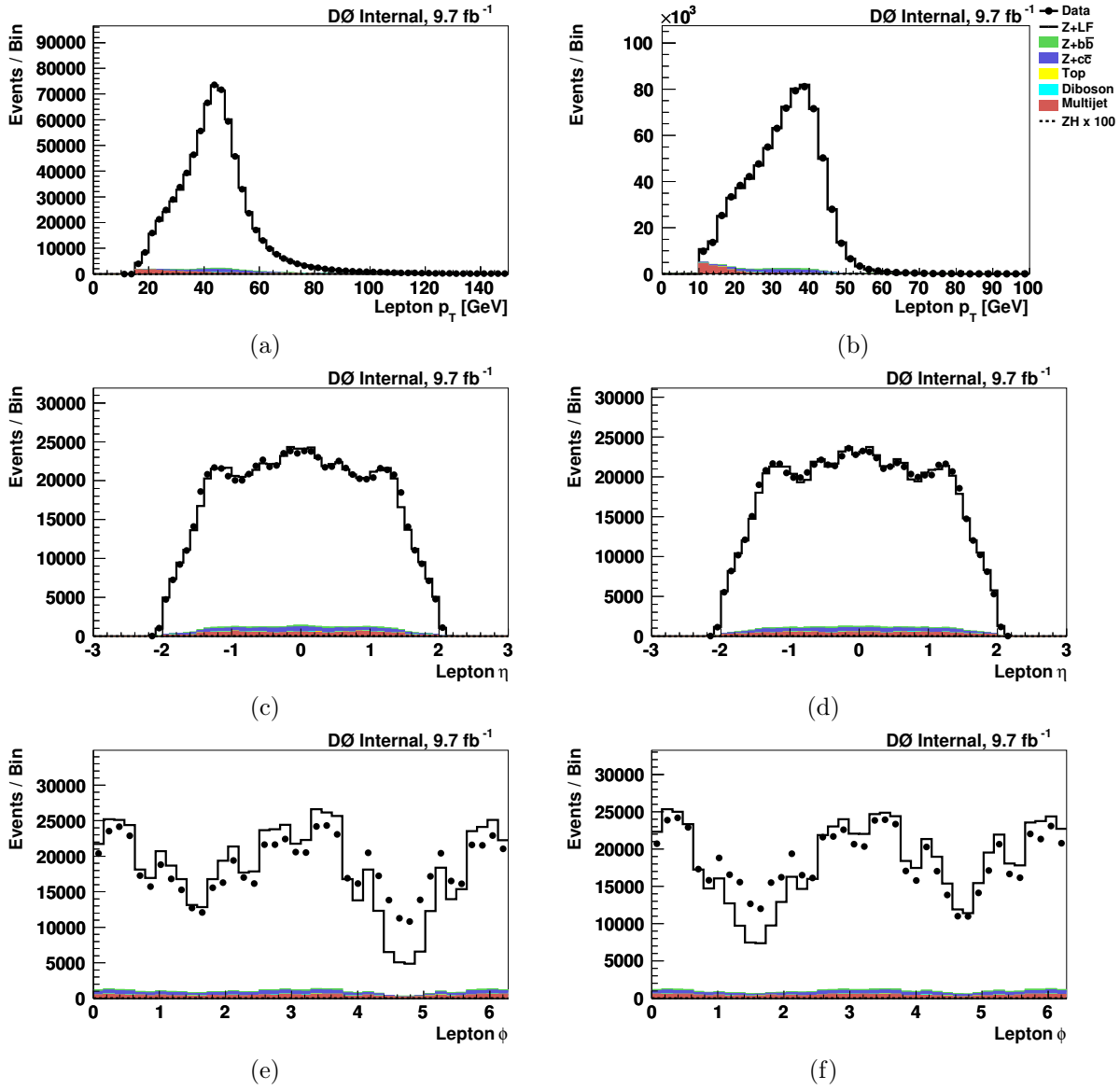

Figure C.3: $\mu\mu$ sample with leptonic preselection but no jet requirements: (a) leading lepton p_{T}, (b) second lepton p_{T}, (c) leading lepton η, (d) second lepton η, (e) leading lepton ϕ, and (f) second lepton ϕ.

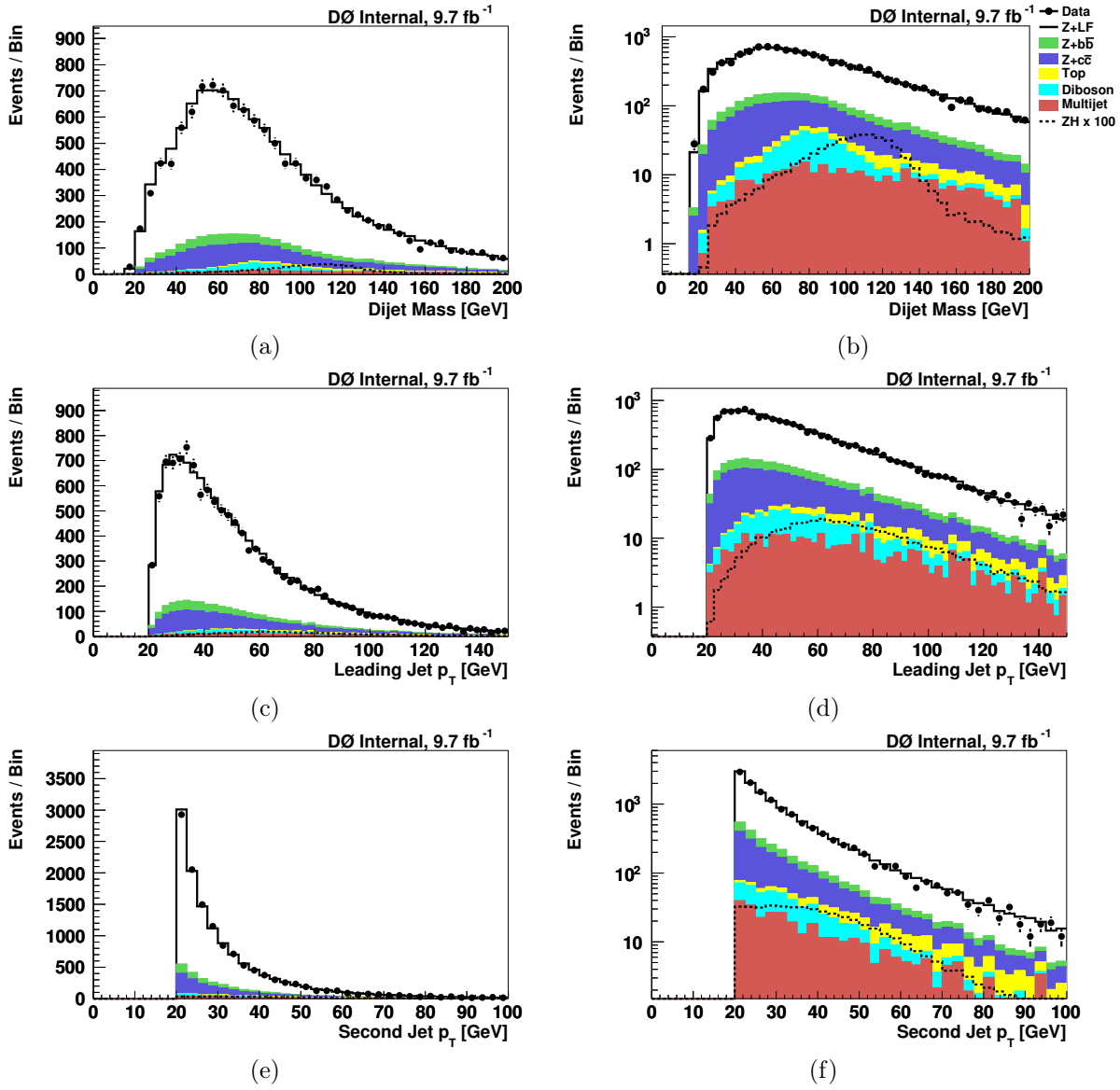

Figure C.4: dimuon ($\mu\mu$) pretag sample: (a) dijet invariant mass, (b) log, (c) leading jet p_{T}, (d) log, (e) second jet p_{T}, (f) log.

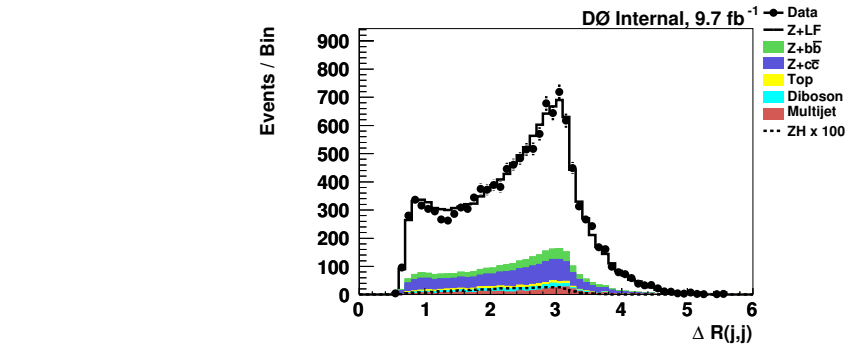

(a)

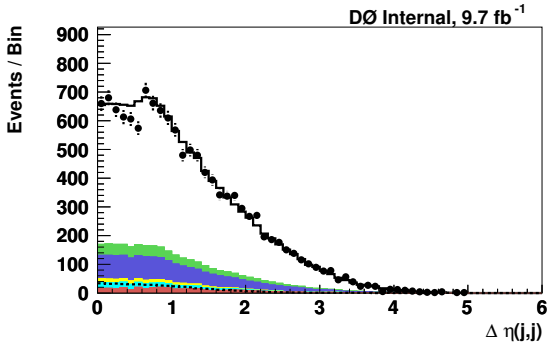

(b)

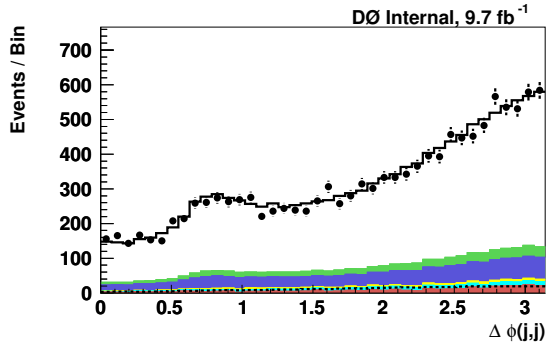

(c)

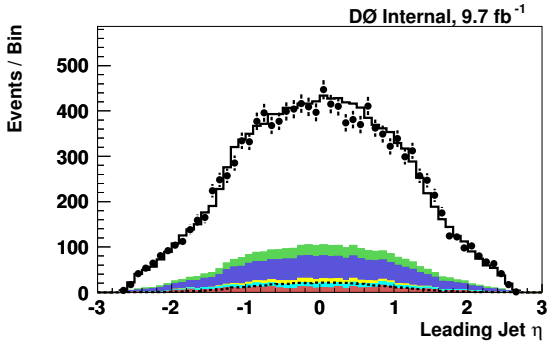

(d)

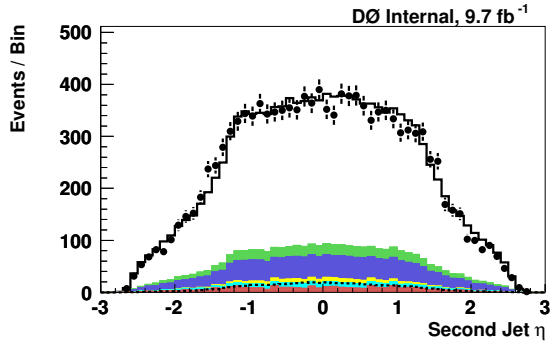

(e)

Figure C.5: dimuon ($\mu\mu$) pretag sample: (a) ΔR between jets in dijet system (b) $\Delta\phi$ of same (c) $\Delta\eta$ of same (d) leading jet η and (e) second jet η.

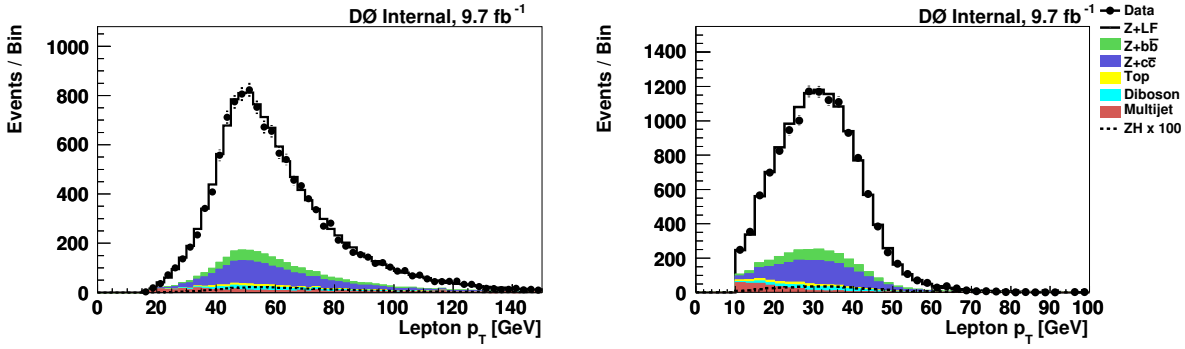

(a) (b)

Figure C.6: $\mu\mu$ pretag sample: (a) leading lepton p_{T}, (b) second lepton p_{T}.

BIBLIOGRAPHY

BIBLIOGRAPHY

[1] V. M. Abazov et al. (D0 Collaboration), Phys. Rev. Lett **109**, 121803 (2012).

[2] V. M. Abazov et al. (D0 Collaboration), Phys. Rev. D **88**, 052010 (2013).

[3] T. Aaltonen et al. (CDF and DØ Collaboration), Phys. Rev. Lett. **109**, 071804 (2012).

[4] S.L. Adler and W.A. Bardeen, Phys. Rev. 182 (1969) 1517; R. Jackiw, Lectures on "Current Algebra and its Applications", Princeton University Press, 1972.

[5] G.'t Hooft, Nucl. Phys. B33 (1971) 173; ibid. Nucl. Phys. B **35** (1971) 167; G.'t Hooft and M. Veltman, Nucl. Phys. B44 (1972) 189.

[6] F. Englert and R. Brout, Phys. Rev. Lett. **13**, 321 (1964); P. W. Higgs, Phys. Rev. Lett. **13**, 508 (1964); G.S. Guralnik, C. R. Hagen, and T. W. B. Kibble, Phys. Rev. Lett. **13**, 585 (1964).

[7] A. Djouadi, Phys.Rept.457:1-216,2008, arXiv:hep-ph/0503172v2.

[8] J. Ellis, M.K. Gaillard, and D.V. Nanopoulos, Nucl. Phys. B **106** (1976) 292.

[9] L. Resnick, M.K. Sundaresan and P.J.S. Watson, Phys. Rev. D **8** (1973) 172.

[10] B.W. Lee, C. Quigg and H.B. Thacker, Phys. Rev. D **16** (1977) 1519.

[11] `http://maltoni.home.cern.ch/maltoni/TeV4LHC/SM.html`.

[12] T. Aaltonen et al. (CDF Collaboration), Phys. Rev. Lett. **108**, 151803 (2012).

[13] V.M. Abazov et al. (DØ Collaboration), Phys. Rev. Lett. **108**, 151804 (2012).

[14] T. Aaltonen et al. (CDF and DØ Collaborations), Phys. Rev. D **86**, 092003 (2012).

[15] LEP Electroweak Working Group, `http://lepewwg.web.cern.ch/LEPEWWG/`.

[16] ALEPH, DELPHI, L3, and OPAL Collaborations, The LEP Working Group for Higgs Boson Searches, Phys. Lett. B **565**, 61 (2003).

[17] Tevatron New Phenomena and Higgs Working Group, arXiv:1207.0449.

[18] G. Aad et al. (ATLAS Collaboration), Phys. Rev. D **86**, 032003 (2012).

[19] S. Chatrchyan et al. (CMS Collaboration), Phys. Lett. B **710**, 26 (2012).

[20] G. Aad et al. (ATLAS Collaboration), Phys. Lett. B **716**, 1 (2012).

[21] S. Chatrchyan et al. (CMS Collaboration), Phys. Lett. B **716**, 30 (2012).

[22] S. Abachi, et al., Phys. Rev. Lett. **74** (1995) 2632.

[23] Tevatron Run II Handbook, `http://www-bd/fnal.gov/lug/`.

[24] S. Abachi et al., Nucl. Instr. and Meth. A **338** (1994) 185.

[25] V.M. Abazov, et al., Phys. Rev. D **66** (2002) 012001.

[26] V.M. Abazov, et al., Nucl. Instr. and Meth. A **565** (2006) 463.

[27] Particle Data Group. Phys. Rev., D50 (3): 1173–1876, August 1994. `http://pdg.lbl.gov/`.

[28] B. Squires, et al., Design of the 2 Tesla superconducting solenoid for the Fermilab DØ detector upgrade, in: P. Kittel, et al. (Eds.), Advances in Cryogenic Engineering, Plenum Press, New York, NY, 1994, p. 301.

[29] G.C. Blazey, et al., arXive:hep-ex/0005012

[30] C. Brown et al., DØ Collaboration, Nucl. Instrum. Methods Phys. Res. A **279**, 331 (1989)

[31] `http://wwwasdoc.web.cern.ch/wwwasdoc/geantold/GEANTMAIN.html`.

[32] A. Schwartzman and C. Tully, Primary Vertex Reconstruction by Means of Adaptive Vertex Fitting, DØNote 4918 (2005).

[33] A. Schwartzman and M. Narain, Probabilistic Primary Vertex Selection, DØNote 4042 (2002).

[34] A. Abdesselam, A. Kumar, et al., DØNote 3745 (2000), 4769 (2005).

[35] X. Bu, et al., DØNote 5545 (2007), 5650 (2008).

[36] O. Atramentov, Y. Maravin, X. Bu, et al., DØNote 4444 (2004), 5764 (2008).

[37] D. Whiteson, A. Kumar, M. Aoki, et al., DØNote 4184 (2003), 4769 (2005), 5675 (2008).

[38] Vertex Fitting by means of the Kalman Filter technique, DØNote 3907 (2001).

[39] S. Calvet, P. Verdier and E. Kajfasz, Towards MissingET Certifiation and Unclustered Energy Studies, DØ Note 4927 (2005).

[40] G. Borissov, Status of DØ track reconstruction. Talk at All DØ Meeting, 14 February 2003.

[41] A. Khanov, HTF: histograming method for finding tracks. The algorithm description, DØNote 3778 (2000).

[42] H. Greenlee, The DØ Kalman track fit, DØNote 4303 (2003).

[43] H. Greenlee, The DØ interacting propagator, DØNote 4293 (2003).

[44] E. Busato, B. Andrieu, Jet Algorithms in DØ Run 2 software, DØNote 4457 (2004).

[45] E. Berger (Ed.), Research directions for the decade. Proceedings, 1990 Summer Study on High-Energy Physics, Snowmass, USA, June 25 - July 13, 1990, Singapore: World Scientific (1992).

[46] "Jet energy scale determination in the DØ experiment", arXiv:1312.6873.

[47] L. Feligioni, M. Narain, P. Schieferdecker, A. Schwartzman Update on b-quark Jet Identication with Secondary Vertex Reconstruction using DReco version p14, DNote 4414.

[48] D. Bloch, B. Clement, D. GelÂťe, S. Greder, Isabelle Ripp-Baudot, Performance of the JLIP b-tagger in p14, DNote 4348. n

[49] Lisa Chabalina, Regina Demina, Alexander Khanov, Flera Rizatdinova `http://www-d0.fnal.gov/phys id/bid/d0 private/certication/p14/CSIP/CSIP v2.html`.

[50] T. Scanlon, A Neural Network b-tagging Tool, DØNote 4889.

[51] S. Greder, I. Ripp-Baudot, B-tagging with combined multivariate techniques, DØNote 5936.

[52] Thomas Gadfort, Gavin Hesketh, Vincent Lesne, Mark Owen, Raimund Strohmer, Boris Tuchming, "Muon Identification Certification for p17 data", D0Note 5157, Sept., 2006.

[53] G. C. Blazey *et al.*, in *Proceedings of the Workshop: "QCD and Weak Boson Physics in Run II,"* edited by U. Baur, R. K. Ellis, and D. Zeppenfeld, (Fermilab, Batavia, IL, 2000).

[54] "Certified preliminary JES for p17 data", JetCorr v07-01-02, `http://www-d0.fnal.gov/phys_id/jes/public/plots_v7.1/`, Feb., 2006.
S. Caughron, "soft muon correction", JES meeting, 20/12/2011 .

[55] Abhinav Dubey, Arnaud Duperrin, Gabriel Facini, Jean-Francois Grivaz, Thibault Guillemin, Joe Haley, Xiaowen Lei, Arthur Maciel, Ruchika Nayyar, Nicolas Osman, Murilo Rangel, Tim Scanlon, Erich Varnes,Ren-Jie Wang "Search for the standard model Higgs boson in the $ZH \to \nu\bar{\nu}b\bar{b}$ channel in 9.5 fb^{-1} of $p\overline{p}$ collisions at 1.96 TeV," DØ Note 6336 (2012)

[56] J. BackusMayes, `http://www-d0.hef.kun.nl//askArchive.php?base=agenda&categ=a10728&id=a10728s1t44/transparencies`.

[57] M. Abolins et al, Nucl. Instrum. Methods Phys. Res. Sect. A **584**, 75 (2008)

[58] D0 Data Quality Coordination, `http://www-d0.fnal.gov/computing/data_quality/d0_private/forusers.html`.

[59] S. Calvet, A. Duperrin, J.-F. Grivaz, E. Kajfasz, D0 Note 5367.

[60] `http://www-d0.fnal.gov/Run2Physics/cs/MC/MC.html`.

[61] T. Sjöstrand *et al.* Comput. Phys. Commun. **135**, 238 (2001) versions 6.319 and 6.413.

[62] M. Mangano *et al.* ALPGEN, a generator for hard multiparton processes in hadron collisions, hep/ph 0206293, JHEP07 (2003) 001, version 2.11, `http://mlm.web.cern.ch/mlm/alpgen`.

[63] MLM matching procedure, `http://www-d0.fnal.gov/computing/MonteCarlo/generators/common_alpgen.html`.

[64] D. Gillberg, D0 Note 5129.

[65] J . Pumplin et al, Nucl. High Energy Phys. **07**, 012 (2002)

[66] T. Sjöstrand and P. Skands, JHEP (2004) 0403.

[67] X. Bu, T. Head, K. Petridis, M. Takahashi, and Y. Xie D0 Note 6116.

[68] M. Vesterinen "An Improved Energy Calibration and Monte Carlo Over-smearing for Electromagnetic Clusters" D0 Note 6040, Mar., 2010.

[69] T. Guillemin, presentation at V+Jets/CSG meeting, March 22, 2011, `http://www-d0.hef.ru.nl//askArchive.php?base=agenda&categ=a11271&id=a11271s1t23/transparencies`.

[70] T. Guillemin, presentation at V+Jets/CSG meeting, November 30th, 2010, `http://www-d0.hef.ru.nl//askArchive.php?base=agenda&categ=a101471&id=a101471s1t14/transparencies`.

[71] J. Hobbs, T. Nunnemann, and R. Van Kooten, "Study of the Z to ee and Z to mumu Yields", D0Note 5268, Oct 27, 2006.

[72] J-F. Grivaz: Talk in the February 12, 2008 VJets working meeting: http://www-d0.hef.kun.nl//askArchive.php?base=agenda&categ=a08266&id=a08266s1t4/transparencies/K-factors.pdf.

[73] M. Shamim and T. Bolton, D0 Note 5565.

[74] http://www-d0.hef.kun.nl//askArchive.php?base=agenda&categ=a091434&id=a091434s1t25/transparencies.

[75] W. Fisher, J. Haley, D. Price, Studies of Alpgen parametes, corrections and associated uncertainties, D0 Note 5966.

[76] C. Balazs and C.-P. Yuan. Phys.Rev.D56:5558-5583,1997.

[77] S. Desai, "Comparison of VH Modeling in Pythia and Resbos", DØNote 6204.

[78] T. Scanlon, "Fake Rate Studies", B-ID Meeting, June 23, 2009, http://www-d0.hef.kun.nl///fullAgenda.php?ida=a09975.

[79] J. BackusMayes, S.B. Beri, K. Chan, M.-C. Cousinou, S. Desai, S. Dutt, M. Mulhearn, E. Nagy, T. Yasuda, "Search for $ZH \to \ell^+\ell^- b\bar{b}$ in 6.2 fb^{-1} of Data Using a Random Forest in Dimuon and Dielectron Events", D0 Note 6080.

[80] E. Barberis, G. Cerminara, G. Hesketh, J. Hobbs, E. Strauss, D. Wood, T. Wyatt, "ZZ to l+l-nunu production in ppbar collisions at sqrt(s) = 1.96 TeV, D0Note 5620.

[81] Toolkit for Multivariate Data Analysis with ROOT, http://tmva.sourceforge.net/.

[82] S. Parke and S. Veseli, "Distinguishing WH and $Wb\bar{b}$ production at the Fermilab Tevatron" Phys Rev D Vol 60 (1999) 093003. (hep-ph/9903231).

[83] T. Guillemin, presentation at V+Jets/CSG meeting, November 30th, 2010 http://www-d0.hef.ru.nl//askArchive.php?base=agenda&categ=a101471&id=a101471s1t141106/transparencies.

[84] J. Campbell, R. K. Ellis, Phys Rev D, **60**, 113006 (1999); **62**, 114012 (2000); **65** 113007 (2002); http://mcfm.fnal.gov/.

[85] U. Langenfeld, S. Moch and P. Uwer, Phys. Rev. D **80**, 054009 (2009) arXiv:0906.5273.

[86] "Cross Section and Branching Ratio Recommendations for Tevatron Higgs Searches", Tevatron New Phenomena and Higgs Working Group, January 2012 Baglio and Djouadi,arXiv:1003.4266v2.

[87] A Confidence Level Limit Evaluator, https://plone4.fnal.gov/P1/D0Wiki/Members/szelitch/hwwmunujj/collie/.

[88] T. Aaltonen et al. (CDF and DØ Collaboration), Phys. Rev. D **88**, 052014 (2013).

[89] V. M. Abazov et al. (D0 Collaboration), Phys. Lett. B **716**, 285 (2012).

[90] V. M. Abazov et al. (D0 Collaboration), Phys. Rev. Lett **109**, 121804 (2012).

[91] V. M. Abazov et al. (D0 Collaboration), arXiv:1301.6122 (2013), accepted by Phys. Rev. D.

[92] V. M. Abazov et al. (D0 Collaboration), arXiv:1301.1243 (2013), accepted by Phys. Rev. D.

[93] V. M. Abazov et al. (D0 Collaboration), Phys. Lett. B **714**, 237 (2012).

[94] V. M. Abazov et al. (D0 Collaboration), arXiv:1302.5723 (2013), submitted to Phys. Rev. D.

[95] V. M. Abazov et al. (D0 Collaboration), arXiv:1211.6993 (2012), accepted by Phys. Rev. D.

[96] V. M. Abazov et al. (D0 Collaboration), arXiv:1301.5358 (2013), accepted by Phys. Rev. D.

[97] T. Aaltonen et al. (CDF Collaboration), Phys. Rev. Lett **109**, 111804 (2012).

[98] T. Aaltonen et al. (CDF Collaboration), arXiv:1301.4440 (2013), accepted by Phys. Rev. D.

[99]

[100] T. Aaltonen et al. (CDF Collaboration), J. High Energy Phys. 02 (2013) 004.

[101] T. Aaltonen et al. (CDF Collaboration), Phys. Rev. Lett. **109**, 181802 (2012).

[102] T. Aaltonen et al. (CDF Collaboration), FERMILABPUB-13-029-E (2013), for submission to Phys. Rev. D.

[103] T. Aaltonen et al. (CDF Collaboration), Phys. Rev. Lett. **108**, 181804 (2012).

[104] T. Aaltonen et al. (CDF Collaboration), Phys. Lett. B **717**, 173 (2012).

[105] T. Aaltonen et al. (CDF Collaboration), Phys. Rev. D **86**, 072012 (2012).